AN ABSTRACT OF THE THESIS OF

Maximo Argo for the degree of Master of Science in Civil Engineering presented on August 31st, 2016.

Title: Seismic Performance of Aging Prestressed Transmission Poles with Simulated Soil Foundation.

Abstract approved:

_____

Christopher C. Higgins

The Cascadia Subduction Zone has recently been identified as a source for an impending great earthquake. The potential of a large earthquake has created widespread interest into the resiliency of lifelines within the potentially affected areas. One critical lifeline is the electrical distribution and transmission systems which relies on legacy infrastructure components that were designed and constructed without regard to the seismic hazard. Of particular interest is the resiliency of prestressed concrete poles used for transmission towers within the region. Through material and structural testing of existing full scale specimens,

moment capacities have been analyzed and compared to simulated earthquake moment demands. The structural testing allowed for an innovative solution to produce simulated site response through fabricating soil representative springs using steel plates. The soil simulated springs allowed for full scale testing with non-fixed base motions such as rotation and translation. After the conclusion of testing three different specimens, it was found that the poles remaining in the field are considerably vulnerable to site conditions but would structurally survive a subduction zone like earthquake.

Seismic Performance of Aging Prestressed Transmission Poles with Simulated soil Foundation

by

Maximo Argo

A THESIS

submitted to

Oregon State University

in partial fulfillment of

the requirements for the

degree of

Master of Science

Presented August 31, 2016

Commencement June 2017

Master of Science thesis of Maximo Argo presented on August 31, 2016

APPROVED:

Major Professor, representing Civil Engineering

Head of the School of Civil and Construction Engineering

Dean of the Graduate School

I understand that my thesis will become part of the permanent collection of Oregon State University libraries. My signature below authorizes release of my thesis to any reader upon request.

Maximo Argo, Author

ACKNOWLEDGEMENTS

I would like to sincerely thank Dr. Chris Higgins, Dr. Burkan Isgor, and Dr. Jason Ideker for the guidance and support throughout the creation and realization of this project.

I would like to thank the Cascadia Lifelines Program for the funding of this project.

I would like to thank Eugene Water and Electric Board for supplying the decommissioned prestressed concrete specimens for testing.

The project could not have been completed without the help of Walter Webster, Jeff Gent, and Tyler Deboodt. Their contributions made laboratory testing and data collection possible.

Finally, I would like to thank my friends and family who have made moving to Oregon possible and the time I spent here unforgettable.

TABLE OF CONTENTS

TABLE OF CONTENTS (Continued)

TABLE OF CONTENTS (Continued)

LIST OF FIGURES

LIST OF FIGURES (Continued)

LIST OF FIGURES (Continued)

LIST OF FIGURES (Continued)

LIST OF FIGURES (Continued)

LIST OF FIGURES (Continued)

LIST OF TABLES

Table: Page

1 Introduction

1.1 Organization of Thesis

The thesis has been divided into five chapters.

Chapter 1 Introduction: This chapter primarily discusses the overview of the project and what has been studied to complete such a project.

Chapter 2 Literature Review: This chapter is written to understand the problem in its entirety and what areas of study have been previously accomplished.

Chapter 3 Experimental Study: The specimens tested and the testing apparatus have been described within this chapter. The methods for the material and structural tests have been summarized.

Chapter 4 Experimental Results: The analysis of the results including figures and tables for both material and structural testing have been presented.

Chapter 5 Comparative Analysis: The analysis for both Response2000 and OpenSees are compared to experimental results.

Chapter 6 Conclusion: The interpretation and recommendations of the study are provided in this chapter.

The Appendix contains pictures and figures of results from the various tests. Also included are the design drawings provided by Eugene Water and Electric Board.

1.2 Background

Cascadia is a region in North America that spans from northern California to the state of Washington and continues into British Columbia that borders the Pacific Ocean. The plate tectonics within this region are driven by a subduction zone between the Juan de Fuca plate and the North American plate. The Juan de Fuca plate has been slowly descending under the North American plate along an approximately 700 mile (1130km) segment that runs parallel to the Pacific Northwest coast (Cascadia 2013).

The plate interactions creates strain along the fault leading to a large storage of energy. A release of energy in such a subduction zone results in a long duration earthquake. The long duration can lead to larger ground movements. The region creates a unique situation in which the subduction zone has not dissipated energy through small earthquakes along the fault leading experts to believe a large release will occur (Goldfinger *et al*. 2012). Geologic history in the region has lead experts to believe that a large earthquake (moment magnitude 9.0+) can be expected every 400-600 years as there have been seven in the past 3500 years, most recently in 1700 (PNSN 2016). The recurrence of a large earthquake has been predicted and therefore the resilience of the affected areas should be improved with knowledge and understanding of what will occur.

A group of researchers at Oregon State University have partnered with industry to come together and form The Cascadia Lifelines Program (CLiP) with the primary objective to research soil liquefaction, improvements to infrastructure, evacuation routes, create tools to predict risk, and potential land slide locations from a Cascadia Subduction Zone event (Oregonstate.com 2016). All aspects of the CLiP initiative are to reinforce the resilience of

the Pacific Northwest, reduce the damage to structures or infrastructure, and prevent loss of life.

Eugene Water and Electric Board (EWEB) is a member within CLiP and have around 600 hundred utility poles in service within the Willamette Valley of Oregon, many of which are prestressed concrete. The prestressed concrete bulb I-beams were a new technology in the 1960's and were regarded as the way of the future for building materials (Rodgers 1984). In the early 1960's, EWEB contracted the Morse Brothers to build a series of prestressed concrete poles for their network of power transmission towers. At the time, prestressed concrete was in its early years of use and design was standardized only in the late 1950's (PCI 2016). Towers that are currently being designed have historically performed well during seismic response (ASCE 2010). Though interest into older designed structures has not been as widely examined. The focus of this thesis is to investigate the seismic resilience of aging transmission towers in the northwest subjected to the Cascadia Subduction Zone earthquake.

1.3 Research Significance

The rising concern for a large seismic event in the Pacific Northwest has increased in recent years as other large scale disasters have occurred around the world such as the 2011 Tahoku Tsunami in Japan, 2005 Hurricane Katrina on the Gulf Coast of the United States, and 2012 Hurricane Sandy along the eastern seaboard of the United States crippling the regions effected (Tipson 2013). The seismic performance of infrastructure is imperative for survivability during a catastrophic event and to enable effective relief efforts. Power transmission is often neglected as an immediate need, falling behind water and transportation, but currently most modes of communication require a power source.

The objective of this thesis is to investigate the seismic performance of legacy prestressed concrete transmission poles within the Eugene Water and Electric Board inventory. The amount of aging experienced by the poles was studied by means of material testing, both destructive and non-destructive, as well through structural tests. The structural capacity of the poles was assessed by destructive tests in the Structural Engineering Research Laboratory at Oregon State University. A unique feature of the tests was inclusion of simulated soil-structure interactions. The response of the poles from such testing provides seismic performance data for EWEB regarding the seismic resiliency of the structures remaining in service.

2 Literature Review

2.1 Seismic issues in Cascadia Subduction Zone

The Cascadia Subduction Zone (CSZ) resides as close as 40 miles (60 km) off the northwest off the coast of the United States and southwest coast of Canada (Goldfinger et *al*. 2012). The subduction is a fault system where the Juan de Fuca Plate is descending under the North America Plate. The 700 mile (1130 km) border where the plates converge receives resistance from the North America plate (Cascadia 2013) causing a strain to build up at the fault. Subduction zone earthquakes demonstrate characteristics of both deep and shallow earthquakes; these types of sources can cause long period earthquakes from great depths but become weak or short damaging earthquakes from shallow depths (Cascadia 2013). The subduction zone builds strain in the plates and can gradually release the energy with lower magnitude earthquakes which have not been observed in the CSZ (PNSN 2016). A cause for concern stems from nonoccurrence of earthquakes in the recent past within the region and the evidence of a large earthquake, M8.7 - M9.2, which occurred in January of 1700, as dated by Japanese historical records and sediment samples collected in Oregon (Cascadia 2013). Sediment core samples can estimate plate movements and can also date reoccurrence which have led to the understanding that large events take place with a return interval of 300-800 years with an average 500 year interval (Goldfinger et *al*. 2012). A recurrence interval with a lower bound of 300 years places the Cascadia region at risk for the first event with modern infrastructure.

2.2 Historic Design of Prestressed Poles

The idea of introducing initial stresses, or prestressing, to offset service loads has been around for centuries (Loewe and Llovera 2014). The application for prestressing concrete did not come until Eugene Freyssinet had the idea during lectures in school in the late 1800's (Billington 2004; Dinges 2009). Freyssinet began using pretension steel within concrete for bridges in the early 1900's in France which permitted the use of concrete in more complex applications (Dinges 2009). The prestressing allowed the concrete to bend with reduced deflections, originally seen in reinforced concrete, due to initial camber (Loewe and Llovera 2014).

Freyssinet eventually started making prestressed concrete poles for power distribution in the 1930's after testing identical specifications for a regular reinforced concrete pole against a prestressed pole and saw improved performance from the prestressed option (Rodgers, 1984). The prestressed concrete pole became widely used after World War II for the Soviet Union when they replaced the damaged transmission infrastructure after proving to be more weather resistant (Rodgers 1984).

The United States started to use prestressed concrete poles for power transmission in Florida in 1954 with a 66 kilovolt (kV) system (Rodgers 1984). The concrete poles followed the birth of the Prestressed Concrete Institute in Tampa, Florida, that same year, 1954 (Billington 2004). Following Florida's application, Eugene Water and Electric Board created a bulb I-shape prestressed concrete pole to run a 115 kV transmission line by the Makenzie River (Rodgers 1984). In the design, wind pressure on the superstructure and the horizontal component of conductor tension were considered the only lateral loads. The exclusion of seismic loads during design was common and addressed by the American

Society of Civil Engineers (ASCE) when setting a standard for the creation of transmission structures (ASCE 2010).

2.3 Current Design Approach for Transmission Towers

ASCE created a design manual, *ASCE No. 74,* which focuses on the electrical transmission industry and loads for structures. The manual provides detail about how loading is categorized and chosen based on geographical location within the United States. Transmission systems are designed considering two categories: wire systems and the structure (ASCE 2010). Due to complexities in transmission line connections and proper representation of conductors, only the structure is under consideration for the present research.

The geographic location of a structure dictates the wind load and ice loads on the structure. After years of experience and observing conditions leading to tower failure, it was noted that wind and ice loads controlled the design loads of transmission towers (ASCE 2010). It is believed that he combinations of a wind event and ice accumulation on the conductors leads to a design that is sufficiently robust to withstand a seismic event (ASCE 2010). The manual contains a section dedicated to earthquakes loads and states "transmission structures need not be designed for ground-induced vibrations caused by earthquake motion because, historically, transmission structures have performed well under earthquake events…" (ASCE 2010).

The recurrence interval for wind events and ice storms in ASCE 74 was chosen to be a baseline of 50 years up to a maximum of 400 years which gives the designer a ratio of $1/8^{th}$ the probability of failure. The CSZ event, which is expected, has a return interval of 500

years and is said to have a 10% probability to occur in the next 50 years (Cascadia 2013). Not viewing a large enough return interval may be detrimental to the life of the structure.

Vibrations, another potential concern from earthquakes, can damage transmission systems as it can cause fatigue failures or weaken a connection (ASCE 2010). *ASCE No. 74* provides detail of aeolian (wind) induced vibration and what potential steps are required to reduce these risks leading to benefits in damping the system.

ASCE created a more specific report from *No. 74*, called *Prestressed Concrete Transmission Pole Structures* or *ASCE NO. 123,* which covers applications and loads, through testing of prestressed concrete pole style structures (ASCE 2012). Tests conducted to the poles are used to determine the cracking and ultimate moment as well as the deflection which can be sustained during transverse loading (ASCE 2012). Design considerations include the boundary conditions, which view the structure as a cantilever structure from ground line on to the top (ASCE 2012). A cantilever system uses the idea of a fixed end which refers to a support that resists torsion and translation in both vertical and horizontal directions. A fixed boundary condition removes any possibility for foundation to affect the loads applied to the superstructure.

A report by the Federal Emergency Management Agency (FEMA) details seismic resistance for transmission facilities which support the federal government (Yokel 1990). In the report, it stated that before the year 1981, only two incidents of earthquakes causing damage or failure to a transmission tower have occurred (Yokel 1990). In recent years, the Wenchuan Earthquake in 2008 had tower failures from an earthquake (Eidinger 2009), though it was concluded the towers were in a region with landslides and collisions from objects during the event caused failure.

Many have conducted seismic analysis and few full-scale tests of transmission towers trying to see when the unlikely event of seismic loads controlling over wind and ice loading. Researchers looked at all aspects of the transmission system, from tower type (Liang and Hoa 2008; Riley *et al*. 2003) to terrain (Riley *et al*. 2006; Bai *et al*. 2010: Li *et al*. 2011). Riley *et al*. (2003) used models of typical towers such as steel tubular and lattice towers and included more specific towers to see a range of seismic responses from known ground motions, such as: San Fernando 1971, Loma Prieta 1989, Michoacan 1985, and Valparaiso 1989.

Terrain, playing a part in the seismic response, has been studied with different soils being included or geometry of the adjacent towers to induce differing response from standard models (Bai *et al.* 2010; Tian *et al*. 2010; Liang and Hoa 2008). The soil structure interaction was modelled for various settings: rock, sand, and mud for a steel lattice style structure in SAP2000 (Bai *et al*. 2010; Liang and Hoa 2008). The analysis concentrated on members of the lattice tower that were dominated by earthquake loads over wind and ice (Liang and Hoa 2008). While the special variability of the towers within a model, under seismic ground motions, would produce a significant response to the system (Bai *et al*. 2010).

Broken conductor is an issue of concern for tower design due to the extreme lateral load that is initiated by the removal of tension in one direction (McClure and Lapointe 2003). Removing the transmission system from equilibrium with a shock load of a broken conductor can dynamically load the structure and cause failure (ASCE 2010). Transmission towers and the system in which they are connected are fragile, requiring many aspects of design, including seismic, to be considered.

Models of towers, both analytical and experimental generally assume either a fixed or pinned base to the soil (Taniwaki and Ohkubo 2004; Pengyun *et al.* 2012; Li *et al*. 2005; Liang and Hoa 2008; Bai *et al*. 2010, Xie 2013). The papers that include soil in the analysis (Tian *et al*. 2010; Liang and Hoa 2008; Bai *et al*. 2010; Riley *et al.* 2003; Li *et al.* 2011), let the soil receive the motion, dampen if applicable, then transmit the loading to the fixed structure.

2.4 Experimental Performance of Aged Prestressed Poles

Concrete is a well-studied material with desirable traits and documented procedures for interpreting test results to see these characteristics. Papers, standards, and books have been written specifically to test or inspect concrete both destructively and nondestructively (Mehta 2006; Kosmatka and Wilson 2011; Bungey and Soutsos 2001; ASTM 2010; ASTM 2013; ASTM 2014; ASTM 2015; ASTM 2016). Investigation into the effects of age on concrete is a more complicated field. The study of aged concrete requires one of three avenues: accelerated weather conditions, investigated existing structures, or modeling, to observe the effects on the materials of both the concrete and reinforcement.

Dejke (2001) applied accelerated aging techniques to a concrete specimen to monitor the effects to the underlying Glass Fiber Reinforcement Polymers (GFRP). The specimens were aged by various methods including keeping a specimen in a 100% relative hydration environment and at a constant 20° C for one year which correlated to 21 years of field conditions. Another specimen tested was subjected to an elevated temperature of 60° C for 18 months to simulate 100 years of environmental effects. The tests showed noticeable reduction in the tensile strength of the reinforcement as a function of exposure. The study

did not included loading of the specimens or freeze thaw cycles during exposure that would greatly affect the overall state of the concrete.

Saha and Tan (2005) tested beams that were GFRP by accelerating native weather conditions of the region (Singapore). The beams were subjected to sustained loads while remaining in a weathering chamber that controlled the temperature and simulated rainfall. The chamber produced an effect that equated to six times the speed of the natural environment. The longest sustained weathering was six months before final loading until failure was conducted. The results showed that cracking of the concrete beams in the weathering chamber were increased by 36-39% over non accelerated specimens and the ultimate flexural strength of the beam were reduced by 17%. The results of the tests conducted showed the importance of weathering to accurately portray structural capacities subjected to time-dependent effects.

A study done by Choi *et al.* (2015) was conducted on the concrete state of a 90 year old stadium in North Carolina. The seating sections of the stadium were visually inspected for cracking or and other defects that might contribute to reduced performance. Reinforcement was exposed in areas and corrosion was apparent. A region of the stadium was divided into subsections where both core samples and impact echo methods were used to investigate the concrete strength of the section. The dynamic modulus of elasticity was concluded from the impact echo method which allowed an understanding of the damaged received by freeze thaw cycles. Tests of existing structures are limited to noninvasive procedures because the structure in still in use. The value of elaborate tests on existing structures is uncommon and could prove to be beneficial.

An approach consisting of modeling the structure for corrosion and subsequent seismic demand instead of experimental testing is a more convenient method when evaluating an aged structure. Guo *et al.* (2015) created a model within OpenSees that investigated the time dependence of corrosion within a tidal region along a coast to see the reduction in seismic performance. The authors created time dependent corrosion methods to reduce the capacity of the exposed columns of the bridge and a comparative analysis to a corrosion free structure was conducted to see the ductility effects due to exposure lengths. It was concluded that a noticeable effects for ductility were not observed until 60 years of corrosion exposure were observed. The authors concluded through the model that the failure of the system would decrease then increase during service because plastic deformations translate through the different exposed zones allowing it to gain strength before complete failure.

A step further into realistic modeling of structures was conducted by Pitilakis *et al.* (2013) which modeled a cored structure with the inclusion of Soil Structure Interaction (SSI). The authors created three models of code designed moment frame structures varying in height and stories. The models were developed on OpenSees and were subjected to ground motions with multiple foundation ground types that consisted of shear wave velocities consistent to Eurocode 8 soil classifications. The model included a time dependent corrosion parameter that was set to a 50 year exposure value. The authors concluded that the vulnerability of a structure due to earthquake ground motion increased with the inclusion of SSI and furthermore increased with corrosion effects present. Results such as this lend evidence to the need of properly testing a sample with realistic weather related decay as well as boundary conditions corresponding to SSI effects.

SSI is a topic of great importance in design of structures and foundations due to the difficulty in predicting exact response of a system whether it be through experimental testing or modeling. Experimental testing of systems is the most realistic approach in determining how a system will behave. A full scale test of realistic structures in true field conditions is the perfect scenario for researchers (Todorovska 2002). The ability to have monitors within structures for when earthquakes occur and use the data collected to analyze the structural response seems to be straightforward but requires time to collect such a knowledge base or chance that a building was located in a highly monitored region such as the Hollywood Storage Building as studied in Todorovska (2002). Laboratory full scale experiments must be explored as a more viable option to gain insight into structural response. Laboratory experiments to see the soil response from actuator loading was simplified in Negro *et al.* (2000). The structure was not examined but a full scale shallow foot foundation resting in a large caisson filled with soil was subject to ground motions. The footing had had vertical loading available to represent an array of structures by simply increasing the load. The soil was saturated and then subjected to various loadings. The final loading was a sinusoidal displacement controlled test with increasing amplitude until failure of the soil. Experimental tests such as this are useful when seeing how the soil will react to a foundation but miss the response of the structure. Laboratory experiments that utilize shake tables with soil, such as seen in Hosseinzadeh and Nateghi (2004), get a more clear idea of what is happening with SSI. The test required scaling the structure down to capture the entire system. The experiment consisted of a soil basin on top of a 1.2m x 1.4m shake table and scaled down a multistory building resting on top of the soil. The structure was then fit with accelerometers to monitor the building response after subjecting the soil basin to single axis ground motions. The test also included the effects of adjacent buildings

by having the scale small enough to have two structures in the basin without being too close to the boundaries to cause inaccurate soil responses.

Modeling of SSI has many advantages to full scale testing, most notably the feasibility of modeling complex structures at scale. When modeling structures, many times the foundation is chosen to be fixed but this leads to over stiffening of the system and will not have a realistic dynamic response (Dutta and Roy 2002). The Winkler model of placing individual springs throughout the foundations footprint as a simplistic form of representing soil lends an easy avenue to modeling soil (Dutta and Roy 2002; PEER 2005). The Winkler method assumes the soil to be a spring that would deform under a pressure producing a subgrade modulus (Dutta and Roy 2002). The issues with the Winkler spring method, is the soil behaves linear in stress-strain which would not be a fully realistic response to load for soil and the springs interact with the structure individually and do not have continuity (PEER 2005). Concerns in the Winkler model have been addressed and modifications have been made to correct these short comings but the underlying idea of springs to represent soil remain.

2.5 Summary

As seen in the literature review, seismic response of legacy prestressed concrete transmission structures is uncertain. The knowledge that a great earthquake is expected to occur within the Pacific Northwest fuels the need to investigate how non-seismically designed legacy prestressed concrete transmission poles will perform. Insight into realistic response of a structure through soil structure large scale testing can be gained by developing new ways to experimentally model soil. By pushing the structure to ultimate

capacity in an innovative apparatus, results can be compared to similar earthquake characteristics leading to realistic survivability to such an event. Gaining an understanding of how a non-fixed foundation with a more representative approach, such as a soil foundation allowing for rotation and translation, provides greater insight into the expected feild response of the structure.

3 Experimental Study

3.1 Specimens

Three prestressed concrete power poles were provided by EWEB for testing. The poles were removed from service. The poles were constructed in the early 1960's when prestressed concrete was gaining momentum in industry and design and construction practices were still emerging (Rodgers, 1984). Fig. *3-1* depicts images of the poles provided in various uses within service.

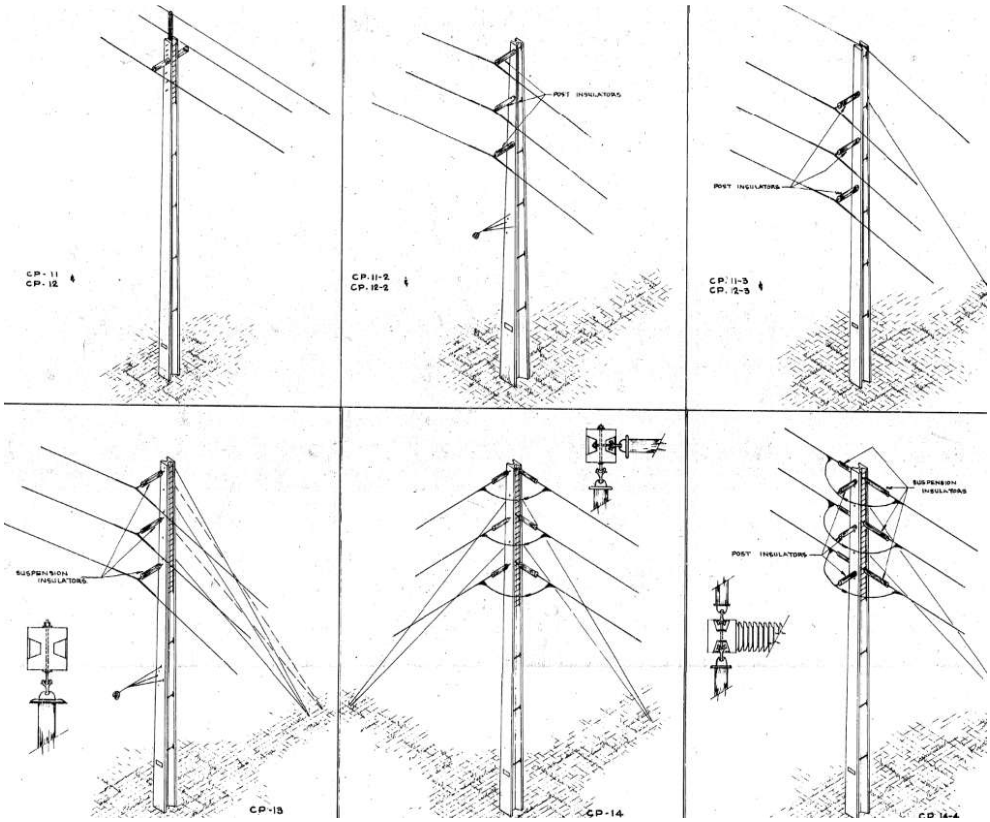

Fig. 3-1 Typical uses for the provided specimens. Courtesy of EWEB provided drawings.

Construction drawings of the specimens were provided by EWEB and were used to identify the section geometry, location of reinforcement, materials, and to understand the construction details for the foundation. Review of the drawings and inspection of the actual specimens led to the design of the testing apparatus. The lower 9.5 ft., or about quarter length of the pole, was embedded into the soil restricting rotation and translation at the base. The soil permits some rotation and translation due to soil deformation when subjected to lateral loads. The embedment depth was not provided but by inspection of the poles, as seen in Fig. *3-2*, indicated a discoloration on the concrete as evidence the ground line.

Fig. 3-2 Prestressed concrete pole specimens staged at the laboratory.

Strand patterns were not provided within the set of strand pattern drawings therefore measurements from the exposed ends were required to produce a strand layout. The cross section of the poles tapers along the height from the base to the top but this was not the expected case for the strands, as a result, the strands were assumed as straight lines for modeling purposes.

Initial material properties were identified on the design drawings. The drawings noted that the concrete was to be 5000 and 7000 psi at transfer and 28 days respectively. The prestressing steel strands were low relaxed strand with 270 ksi ultimate strength. The strands were prescribed to have a jacking force of 28.9 kips per strand. An overview of the specimen details is shown in *Table 3-1*. Material tests were conducted post-structural testing to better quantify the material properties.

Table 3-1 Specimen details at ground line.

	Pole 1		Pole 2		Pole 3
Description	Cyclic	Monotonic	Cyclic	Monotonic	Cyclic
f'_c (psi)	7000	7000	7000	7000	7000
E_s (ksi)	28500	28500	28500	28500	28500
Prejack/strand (kip)	28.9	28.9	28.9	28.9	28.9
Height (in)	15	14	15	14	15.8
Width (in)	15	14	15	14	15
Web Thickness (in)	4.25	4.25	4.25	4.25	4.25
Flange Thickness (in)	3	3	3	3	3
Weight (k)	5.8	3.9	5.8	3.9	5
Length (ft)	40	29	40	28.5	30.96
GL Area (in^2)	156.2	139	156.7	134.2	162.6
Inertia (in^4)	2278.7	1735.8	3942.9	2972.3	2564.8

Two poles were of the same specification, a 40 ft. long tapering bulb I-beam shape. The bottom section begins with a flange width and depth 16 in. then tapers down to 12 in. The

cross section of the pole at ground line was the section of particular interest during testing. Each 40 ft. pole had five prestressed strands in each flange. The middle strand was debonded. A mild steel #3 rebar (Grade 40) was included in each flange located off center between the outer most strand and inside strand. The cross section and strand pattern for the 40 ft. poles in weak axis (Pole 1) illustrated in *Fig. 3-3* and strong axis (Pole 2) illustrated in *Fig. 3-5* with profile views in Fig. *3-4* and Fig. *3-6* respectively.

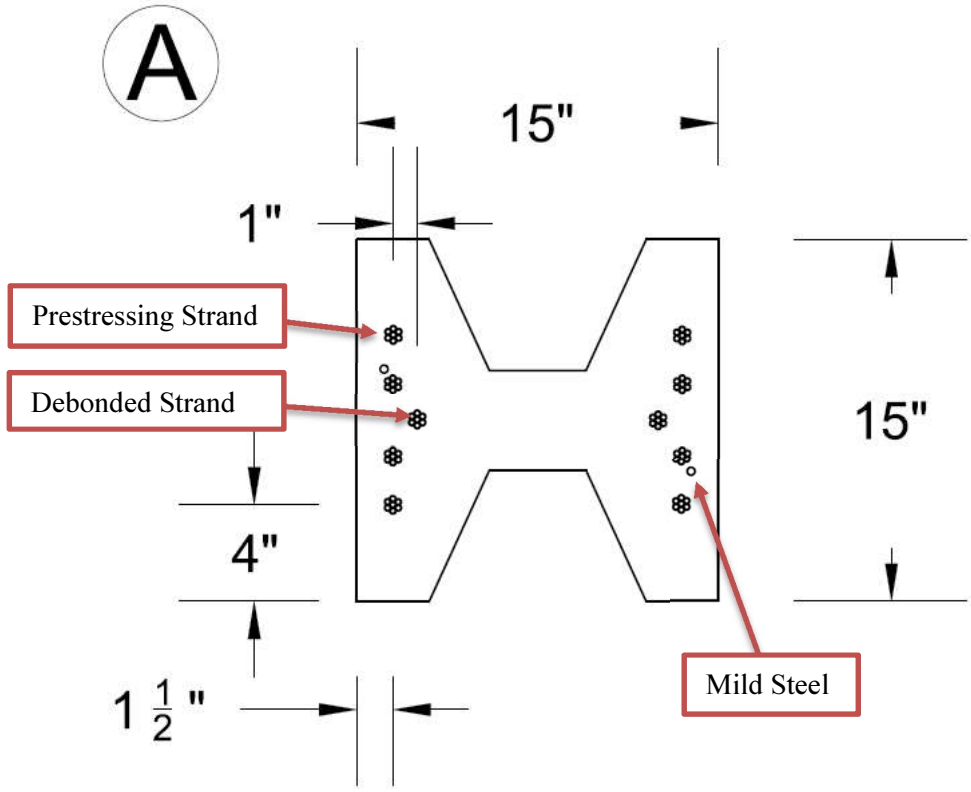

Fig. 3-3 Cross section of Pole 1 with highlighted debonded strand.

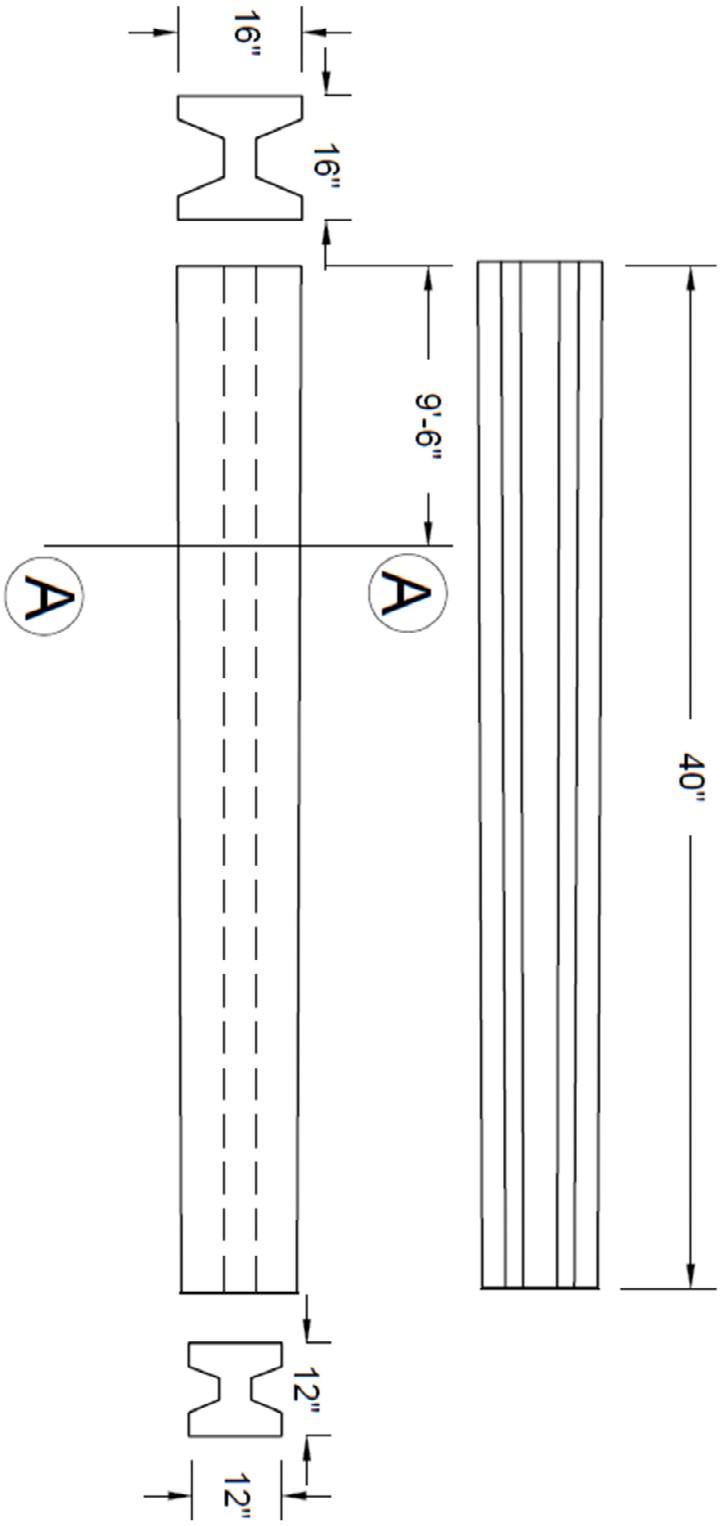

Fig. 3-4 Pole 1 profile.

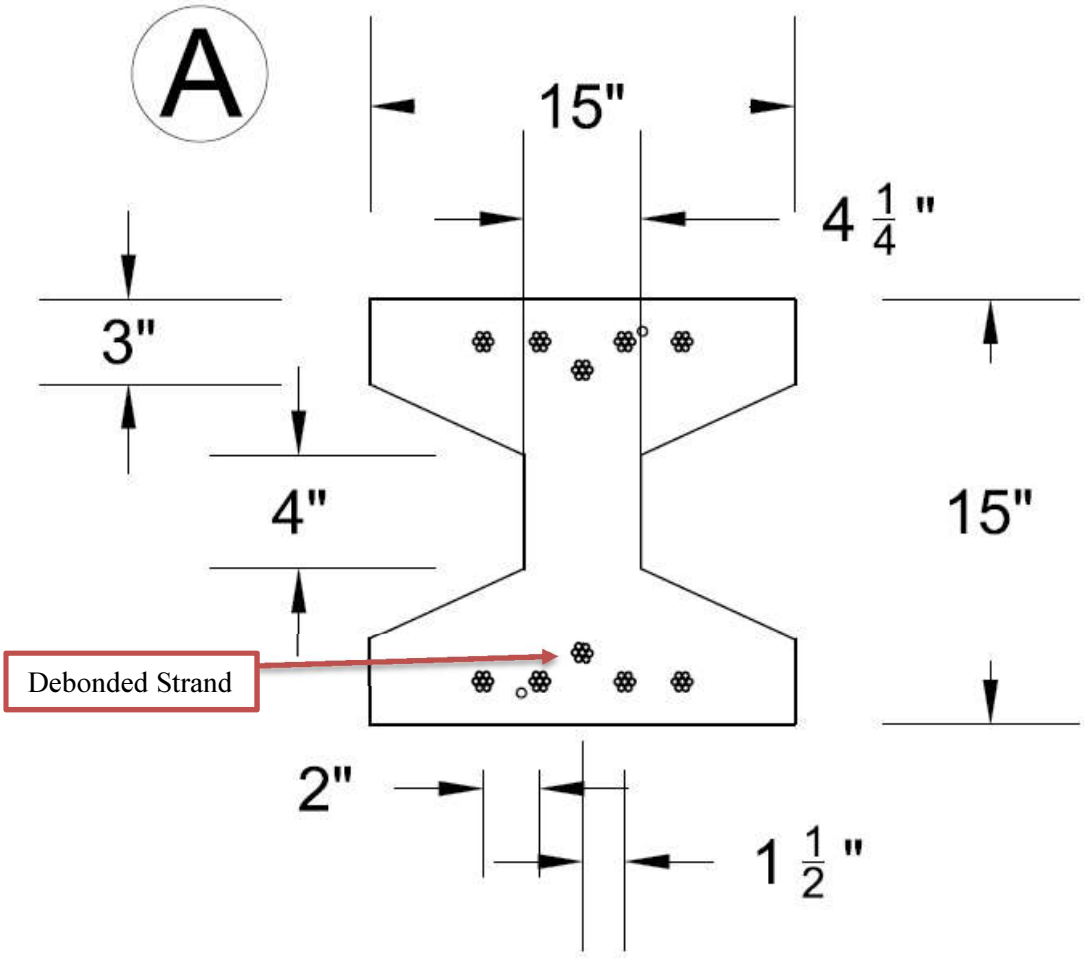

Fig. 3-5 Cross section of Pole 2 with highlighted debonded strand.

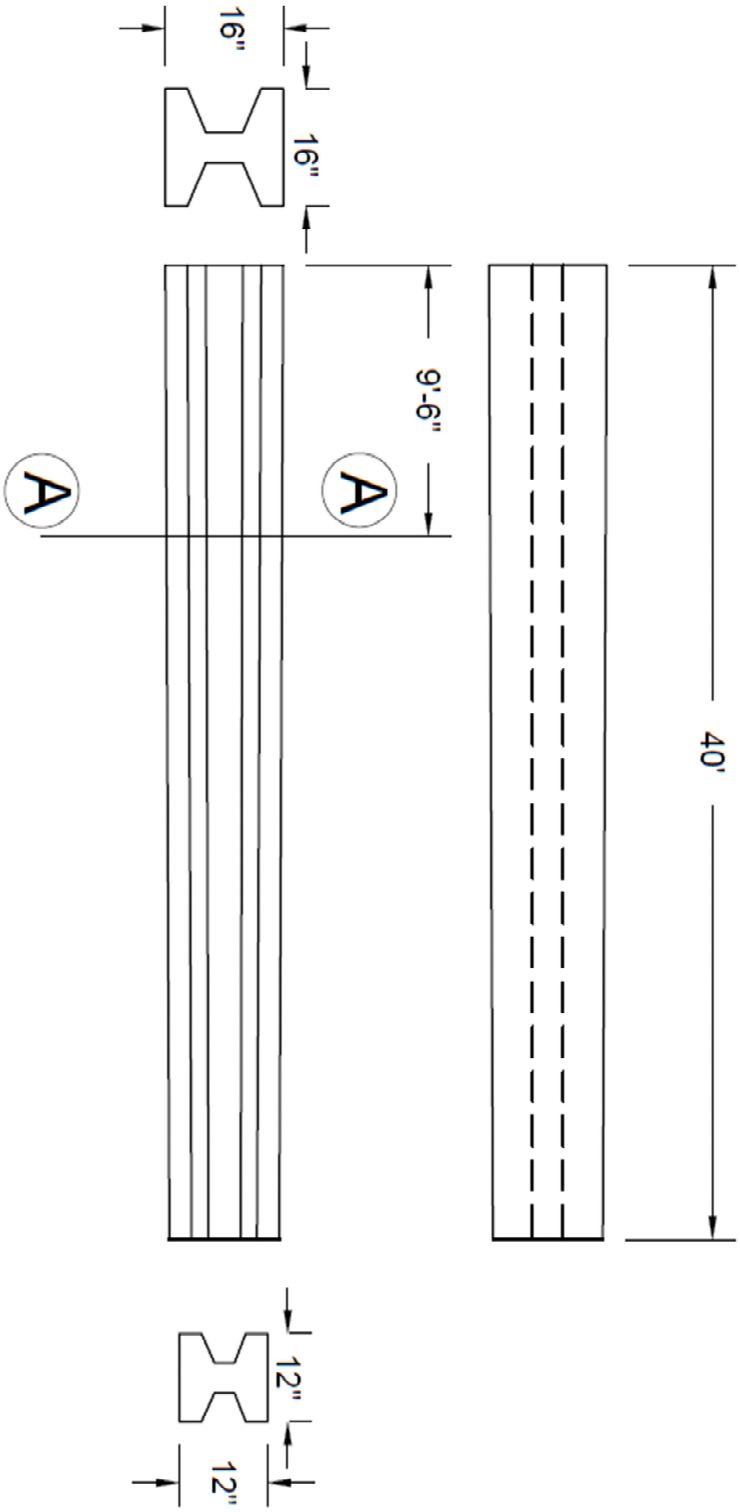

Fig. 3-6 Pole 2 profile.

The third specimen (Pole 3) was unique from the previous two; it was a segment of a larger and longer pole. Originally it was a 70 ft. pole that was extracted and then cut into two pieces, the top 30 ft. 11.5 in. was used for the final test because this portion was of similar dimension to the first two poles and thus could fit into the test setup. The cross section of the pole is illustrated in *Fig. 3-7*. The strand pattern for the larger pole was distinctive from the other specimens with a pattern of 4 strands spaced throughout the width of the flange on one side and 6 strands on the other.

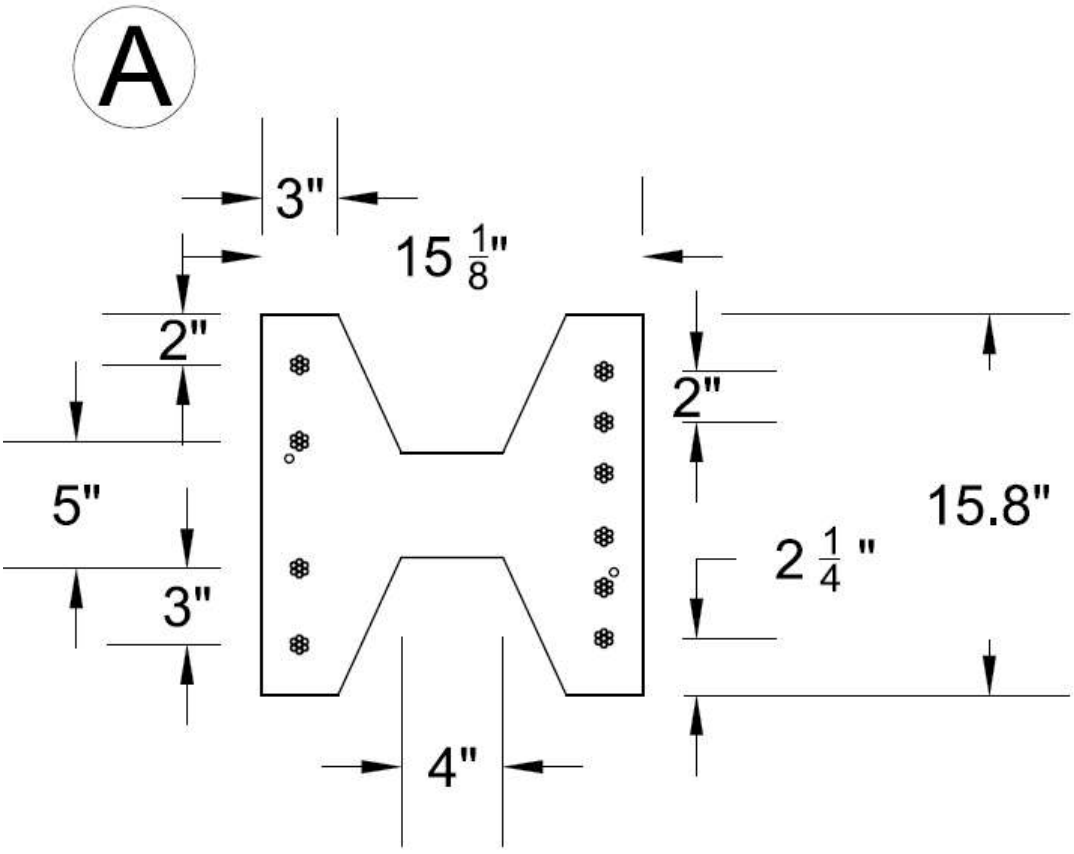

Fig. 3-7 Cross section of Pole 3 with strand pattern.

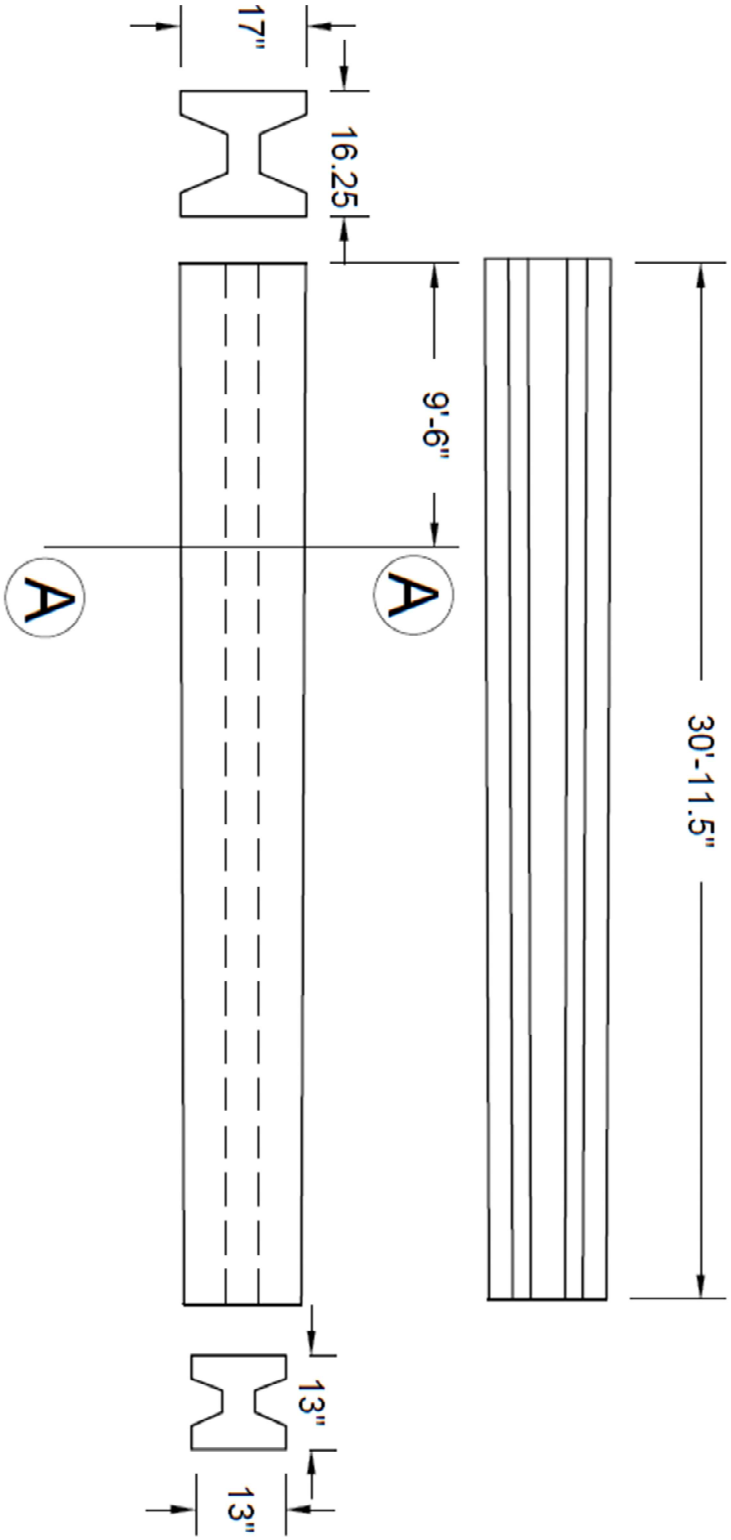

Fig. 3-8 Pole 3 profile.

3.2 Experimental Methods

3.2.1 Material Tests

A range of tests were conducted to verify concrete and reinforcement properties and assess the effects of age and possible deterioration. The primary areas of interest were the concrete and reinforcement properties. Table *3-2* depicts the tests performed for investigating the aged specimens. Visual inspections were performed on the reinforcement and concrete to assess their condition and samples were removed for mechanical tests.

Table 3-2 - Material tests performed

Material	Test	Section Description
Concrete	Concrete Compressive Strength	3.2.1.1.1
Concrete	Carbination	3.2.1.1.2
Concrete	Surface Resistivity	3.2.1.1.3
Concrete	Half-Cell Testing	3.2.1.1.4
Concrete	Scanning Electron Microscopy	3.2.1.1.5
Concrete	Petrographic Analysis	3.2.1.1.6
Reinforcement Steel	Tensil Test	3.2.1.2.1
Prestressing Strand	Tensil Test	3.2.1.2.2

3.2.1.1 Concrete

3.2.1.1.1 Concrete Compressive Strength

Concrete compressive strength testing was conducted by removing 3.75 in. diameter cores from the webs of each specimen. Two cores were taken for each section of interest. A section from both above and below ground on the 40 ft. poles were selected to assess the effects of aging variability along the length of the specimen. The top section of the 70 ft. pole only required core samples from one location due to the specimen not having been embedded in soil.

Tests were conducted in accordance with ASTM C39, *Compressive Strength of Cylindrical Concrete Specimens* (ASTM Standards 2016). The web thickness of the specimens 4.25 in. while the diameter of the cylinders was 3.75 in. The length was shortened from grinding to achieve a level surface then sulfur mortar capping was utilized to achieve parallel ends. A correction factor ranging from 0.87 to 0.93 was apllied for a 1.0 to 1.25 ratio for length to diameter, the value was linearly interpolated (ASTM Standards 2013).

3.2.1.1.2 Carbonation

Carbonation testing was done in accordance with RILEM TC CPC-18. A sample of the specimen broken off during testing and immediately tested for carbon dioxide exposure. The tests consisted of placing drops of a solution comprised of 1% phenolphthalein in 70% ethyl alcohol onto the exposed concrete surface. The solution indicates carbonation upon contact by not changing color, while the uncarbonated surface area will turn a shade of pink. The color change is due to increased pH levels in the concrete but with carbon dioxide present, the pH level is lower removing the color indicator upon reaction. The drops were placed on the surface of the specimen and the depth of the carbonation measured from the original surface, d_k, was measured. The degree of carbonation is a measure of the passivity of the concrete to inhibit corrosion of the embedded reinforcing steel and prestressing strand.

3.2.1.1.3 Surface Resistivity

Electrical surface resistivity has become a common durability performance indicator in recent years (Andrade *et al*. 2013). This test method does not require the extraction of concrete cores for bulk resistivity or access to rebar for half-cell measurements. The

measurements are taken directly on the surface of the concrete, and a reading is recorded within seconds. One durability indicator is the ability to determine a relationship between electrical resistivity and corrosion rate of reinforcing steel, as well as transport properties throughout the bulk concrete (Polder *et al.* 2000). It was found that the electrical resistivity and corrosion rate are inversely proportional (Lopez and Gonzalez 1993, Gowers and Millard 1999). However, the state of the concrete can affect the electrical resistivity measurements. These include the degree of saturation in the pore network, chloride concentrations (Morris *et al.* 2004, Song *et al.* 2007), and the presence of reinforcing steel (Millard 1991). In this research, a four-point Wenner probe was used as seen in Fig. *3-9*.

Fig. 3-9 Electrical surface resistivity measurements.

When the probe's four points contact the concrete, a current is induced and a change in voltage (potential difference) is measured. The two outer most probes induce a current, measured in milliamperes, while the two inner probes measure the potential difference (Garzon *et al.* 2014, Ueli and Angst 2013). The induced current and potential difference are used in the Wenner equation [1] to get the electrical resistivity of the concrete as:

$$\rho = 2\pi * a * \frac{\Delta V}{I} \quad [1]$$

where a is the spacing between probe electrodes (cm), ΔV is the potential difference (V), I is the current (mA), and ρ is the electrical resistivity (kΩ-cm).

3.2.1.1.4 Half-Cell Tests

Corrosion of the reinforcing steel within a concrete member can be estimated by measuring the voltage difference between the reinforcing steel and a reference electrode. This test method has been widely used in the field as a quick and inexpensive method to determine regions of possible active corrosion. The results may be affected by the degree of humidity, temperature, oxygen content near the reinforcement, micro cracks in the concrete, and stray currents (Mehta and Monteiro 2006). According to ASTM C876 (ASTM 2015), if the measured potential is greater than -200 mV (vs. $Cu/CuSO_4$), then there is a low probability of corrosion. If the measured potential is less than -350 mV (vs. $Cu/CuSO_4$), then there is high probability of corrosion. If the reading is between -200 to -350 mV (vs. $Cu/CuSO_4$), then the probability of corrosion is unknown. In order to obtain half-cell potential results, the positive connection of the volt meter must be connected to the reinforcing steel, and the negative connection must be connected to the reference

electrode. The positive terminal of the voltmeter was connected to an exposed region of the reinforcing steel. A small hole was drilled and a steel nail was embedded to ensure a good connection and no interference caused by any surface corrosion products. The positive terminal of the volt meter was then connected to the nail. Connectivity of the entire reinforcing cage was determined prior to testing. For this research, a saturated calomel electrode was used, as seen in Fig. *3-10*.

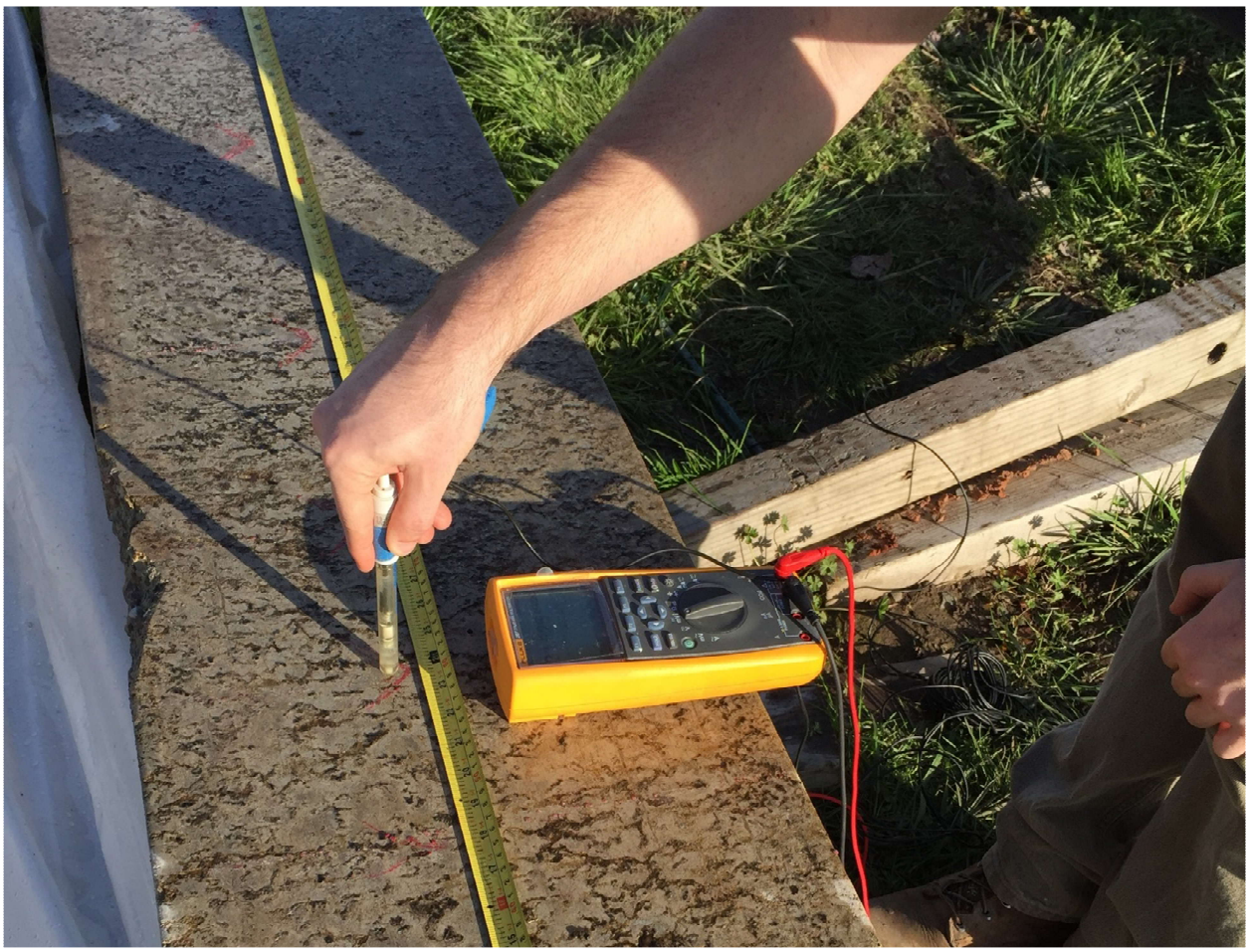

Fig. 3-10 Half-cell measurements.

3.2.1.1.5 Scanning Electron Microscopy

Scanning electron microscopy (SEM) was used to investigate the microstructure of select regions of the concrete. For the 40 ft poles (weak and strong axis), one sample was taken above the ground line and one sample below the ground line to compare any differences caused by in-service environmental conditions. Thin sections (3 mm thick) were cut from the selected concrete regions, impregnated with epoxy, and polished prior to observation. An FEI Quanta 600F environmental SEM was used under high vacuum with a BSE detector with a beam acceleration of 15 kV was used for all imaging.

3.2.1.2 Reinforcing Steel

3.2.1.2.1 Prestressing Strands

Lengths of prestressing strand were removed after destructive tests of the poles. The sections from which the strand was removed were chosen where no visual cracking was displayed. A 2 ft long section both above and below the ground line were used to take samples. For Pole 3, two sections were taken from the same location because embedment in the ground was not a factor. To ensure that failures would not occur in the hydraulic grips of the universal testing machine (UTM), 1/8 in. by 1/2 in. aluminum angle was used between the grip face and strand as seen in Fig. *3-11*. The sections were then tested in accordance with ASTM E8 for *Tension Testing of Metallic Materials* (ASTM 2015).

(A)

(B)

Fig. 3-11 (A) Aluminum angle used to grip prestressing strand in UTM, (B) Prestressing strand with both ends covered in aluminum angle.

3.2.1.2.1.1 Reinforcing Steel

The tested poles were also reinforced with #3 mild steel reinforcing steel bars in an offset pattern within the flanges as shown in Fig. 3-3. To establish the constitutive properties of the reinforcing steel, a 2 ft section of bar was removed from the locations previously cut to remove prestressing strands. These 2 ft long sections were then cut down to various testing lengths of 9 in. to 13 in. to avoid stress concentration on the bars due to welded transverse

steel used during construction to assemble the cages. A schematic of the transverse steel with weld locations and strand is seen in Fig. 3-12. The straight bars without welds located on the samples were tested in accordance with ASTM E8 for *Tension Testing of Metallic Materials* on a hydraulic MTS ASTM (Standards 2015) as seen in *Fig. 3-13*.

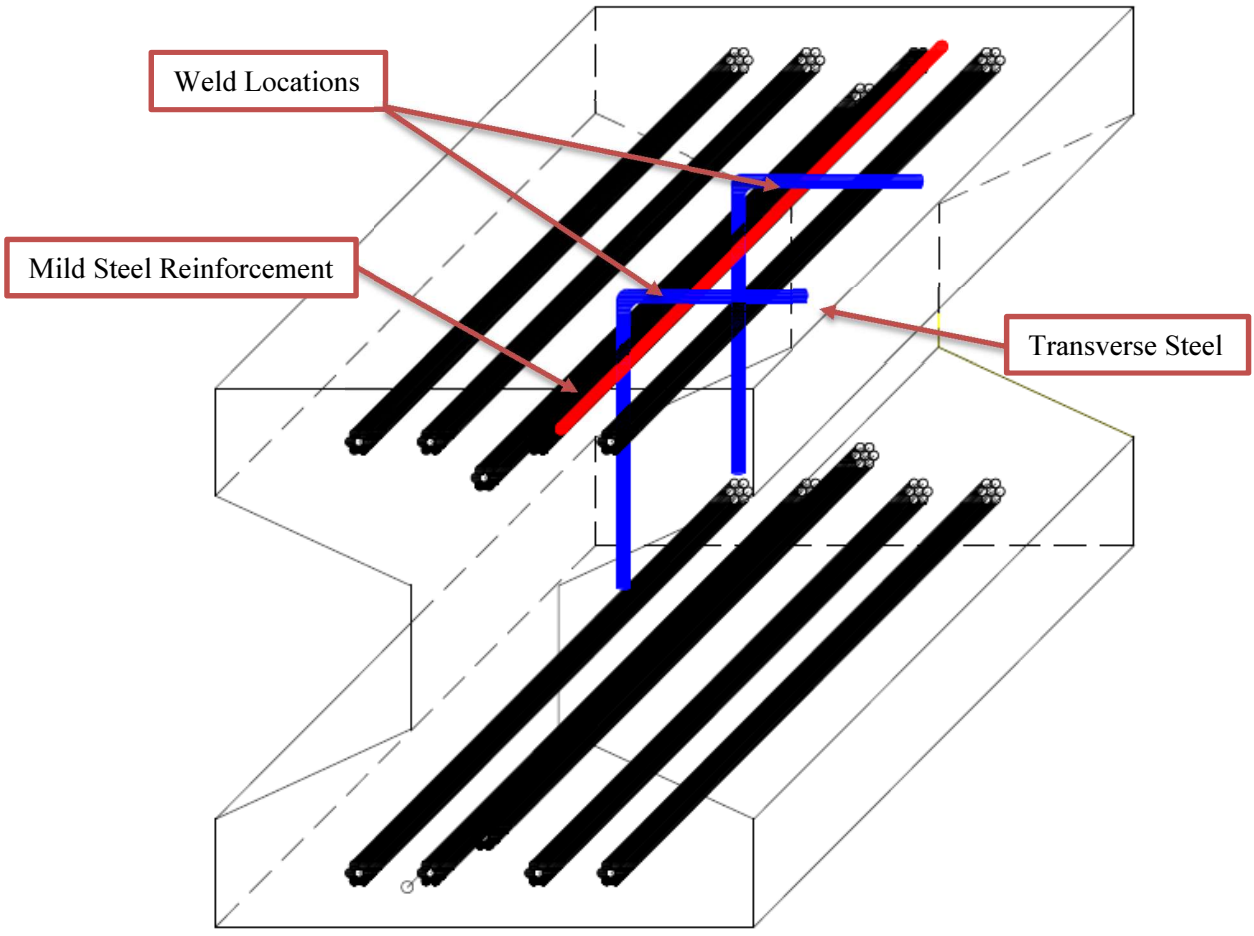

Fig. 3-12 3D rendering of transverse reinforcement with transverse locations.

Fig. 3-13 Mild reinforcing steel samples within UTM.

3.2.2 Material Results

Materials of the specimen such as the concrete, prestressing strand, and mild steel rebar were investigated for properties in which would more accurately represent the specimens within the models for structural performance.

3.2.2.1 Concrete Strength

The concrete compressive strength testing showed expected results. Multiple samples from each section were tested under ASTM C39 conditions and presented in *Table 3-3* in units of psi. The correction factor ranging from 0.93 to 0.87 due to height to diameter ratio (ASCE Standards 2016) was applied as needed to each sample. The samples had to be trimmed of raised edges due to the narrowing of the web for the above ground sections as well as some below ground sections. Sulfur capping was done to at least one core from every sample and ranged from being within reasonable range of the non-capped specimen such as tests for 40’ Weak Axis - Above Ground. The samples for 40’ Strong Axis – Below Ground were all sulfur capped and proved to have the highest standard deviation for compressive strength. The values for the compressive strength are lower for above ground samples for both the weak and strong axis specimens. The lower compressive strength is most likely due to the section being more exposed to the effects of elements and weathering. A value of 7000 psi was selected for use in the analytical models which corresponds to the lowest compressive strength in Table *3-3*.

Table 3-3 Concrete Compressive Strength from Core Samples.

ID	Average f'c (psi)	Std Dev
40' Weak Axis - Above ground	6972	226
40' Weak Axis - Below ground	8203	953
40' Strong Axis - Above ground	7194	871
40' Strong Axis - Below ground	10148	1105
70' Weak Axis - Above ground	8443	1008

3.2.2.1.1 Concrete Deterioration

The concrete specimens had aged for 50 years and the potential for deterioration over their in-service life could be anticipated to affect the structural capacity of the specimens. The signs of deterioration were investigated by various methods as detailed in following sections.

3.2.2.1.1.1 Carbonation

Carbonation testing was done immediately following destruction of the specimen during structural testing. A removed section of the flange which broke during testing for each test was taken aside and the 1% phenolphthalein in 70% ethyl alcohol solution was placed on the newly exposed face to see the depth of carbonation. *Fig. 3-14* shows an example of a concrete sample tested. The depth of the carbonation, d_k, showed a maximum of 2-3 mm on sections tested which confidently represent the specimen. The d_k indicated that carbonation has taken effect on the outer most exposed section of concrete but ultimately did not provide a substantial reduction in the capacity of the cross section.

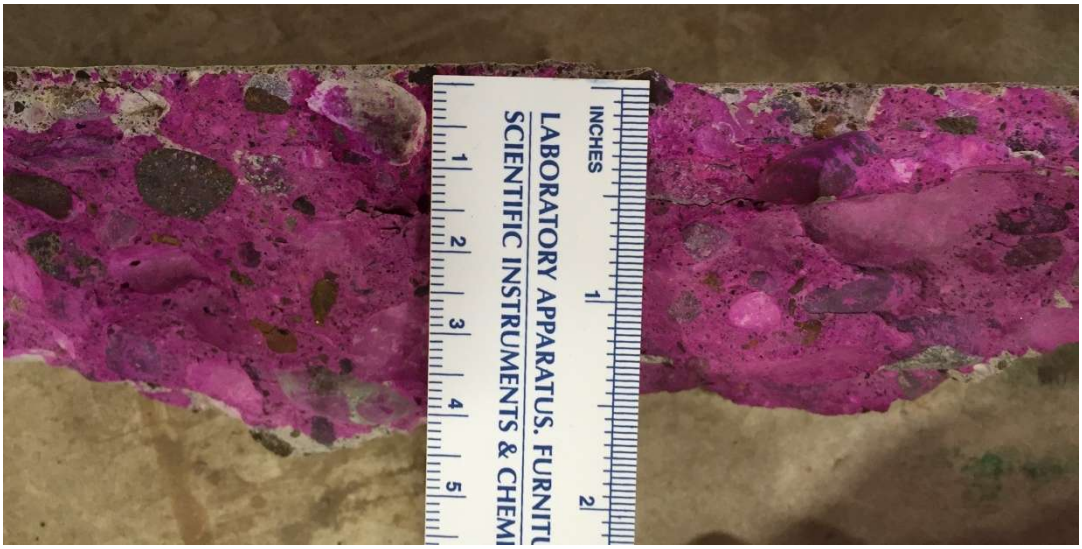

Fig. 3-14 Sample of inspection for carbonation depth.

3.2.2.1.1.2 Surface Resistivity

It can be seen in the results, Fig. *3-15*, for both the strong and weak axis poles that the two ends had lower surface resistivity values compared to the section of the pole that was above ground. The middle section of the poles had values greater than 254 kΩ-cm, which according to AASHTO TP 95 (2014) corresponded to having negligible chloride penetrability. This was likely caused by overall drying shrinkage of the concrete (reduced tortuosity and porosity) as well as a high degree of hydration. The ends of the strong axis pole had lower surface resistivity values, thus indicating there was a very low potential for chloride ion penetration. Furthermore, the lower values of surface resistivity corroborate with the condition of some exposed reinforcing steel, as seen in Fig. *3-16*. However, as discussed in half-cell testing, the reinforcing steel and prestressing strands exhibited no signs of corrosion or deterioration.

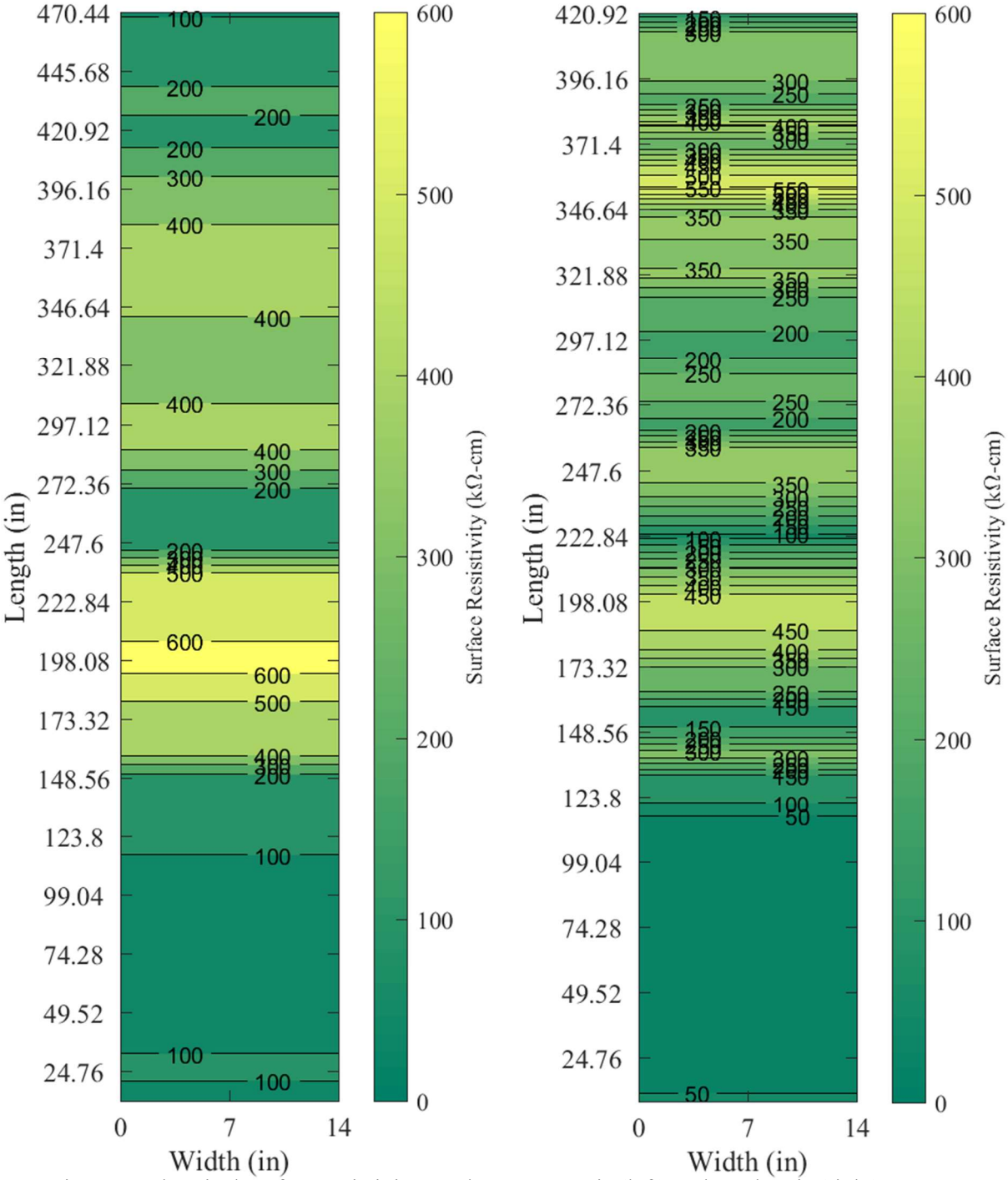

Fig. 3-15 Electrical surface resistivity results. Strong axis (left) and weak axis (right).

Fig. 3-16 Condition of reinforcing steel at pole ends.

3.2.2.1.1.3 Half-Cell Testing

At the time of measurements, the strong axis had a temperature of 18.2 ˚C and the weak axis had a temperature of 15.4 ˚C. The results for half-cell potential for the strong and weak axis tests are seen in Fig. *3-10*. An offset of 73 mV should be applied to convert from readings were taken using a method with saturated Calomel electrode (SCE) to the standard discussed using $Cu/CuSO_4$.

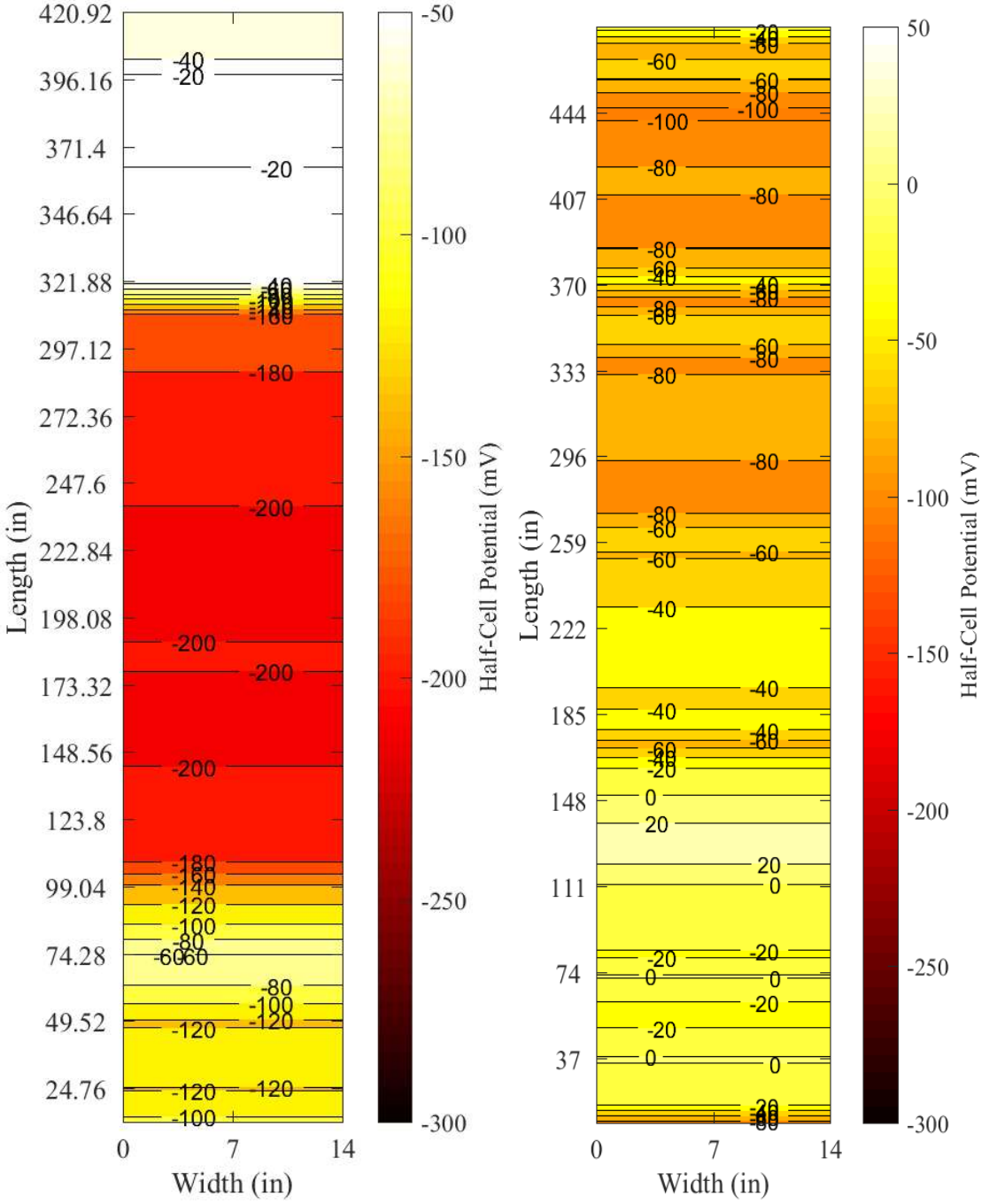

Fig. 3-17 Strong axis half-cell (left) and weak axis half-cell (right). Note: a 73 mV offset is required to all value to get readings vs. $Cu/CuSO_4$.

It can be seen in Fig. *3-17* there is low probability of corrosion occurring in either the strong axis or weak axis poles. For the strong axis, 34 half-cell readings were taken, and it was observed that 79% of the potential readings were greater than -200 mV (vs. $Cu/CuSO_4$) or -127 (SCE). The other potential readings were near -200 mV (vs. $Cu/CuSO_4$) or -127 (SCE) with none exceeding -212mV (vs. $Cu/CuSO_4$). The weak axis had 45 readings and it was observed that 100% of the potential readings were greater than -200 mV (vs. $Cu/CuSO_4$) or 273 mV (SCE). The results of this testing indicated that there was a low probability of corrosion occurring in the mild steel. After structural testing, further destructive tests demonstrated that there was no corrosion was visible in the mild steel or prestressing strands, shown in Fig. *3-18*.

Fig. 3-18 Condition of prestressing strands and reinforcing steel after structural testing.

3.2.2.2 Mild Reinforcing Steel Material Properties

The reinforcing steel samples were removed from sections of the poles above and below ground. The elastic limit for all specimens were consistent with a value just below 60 ksi indicating that the bars were comprised of Grade 40 material. The samples that were pulled from the weak axis specimens (Pole 1 and 3) exhibited a well-defined yield plateau while the samples taken from Pole 2 did not. This may be due to prior yielding which would eliminate the yield plateau. To infer the yield stress of the reinforcing steel in Pole 2 (ignoring the possibility of prior yielding), a 0.2% offset was used. The stress-strain

response is shown in Fig. *3-19* and depicts a yield stress of 56 ksi and ultimate stress of 86 ksi while the response in Fig. *3-20* had a yield stress of 58 ksi and ultimate stress of 86 ksi. The lack of a yield plateau for the sample taken from Pole 2 is likely due to prior yielding during the test in which case the reinforcing bar would go directly into strain hardening (as seen in Fig. 4-6). However, even with this, the yield stress was below 60 ksi which would still categorize the steel as Grade 40.

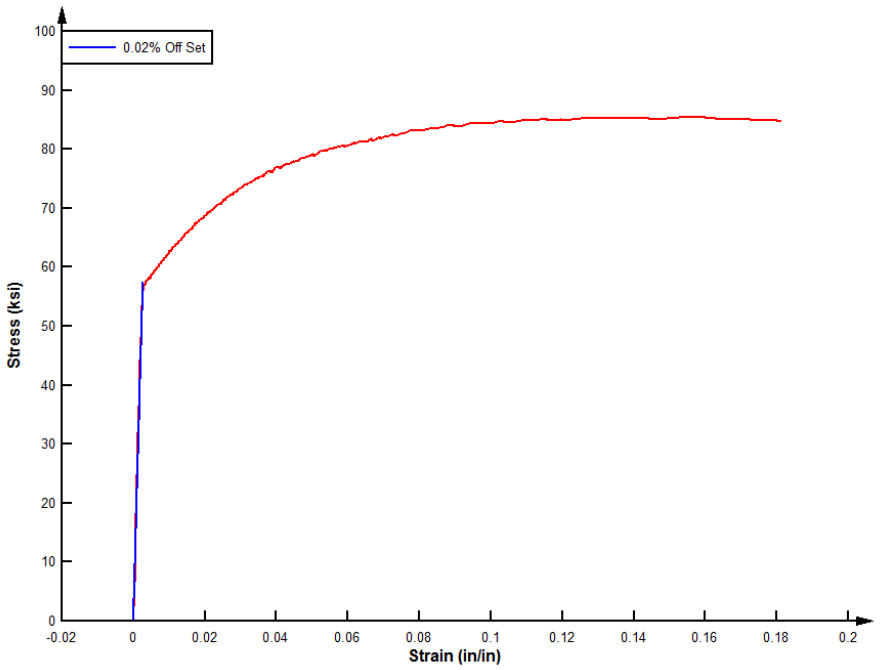

Fig. 3-19 Rebar test demonstration no yield plateau.

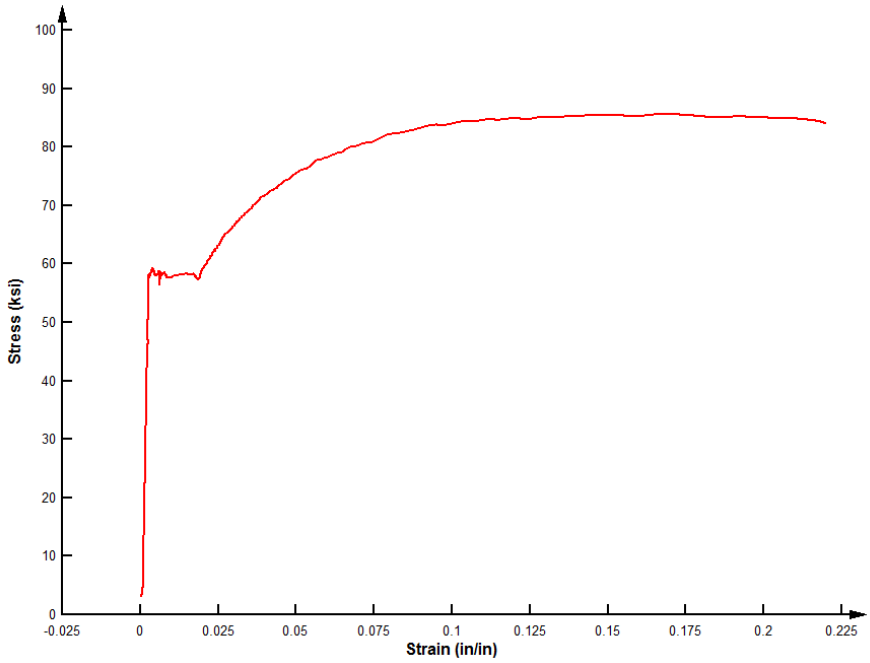

Fig. 3-20 Rebar test demonstrating yield plateau.

3.2.2.3 Prestressing

The prestressing strand was gripped in the UTM using aluminum angles to prevent damage of the cross section of the strand and cause failure in the grips. *Fig. 3-21* provides an image of the aluminum angle after testing and the underlying strand twisting pattern can be seen through the angle.

Fig. 3-21 Aluminum angle after gripping prestressing strand during a test.

The rupture of the prestressing strands occurred outside the grips and provided examples of cup and cone fracture surfaces typical of ductile metallics. *Fig. 3-22* depicts the strand after failure at mid-length of the 2 ft long specimen. At the top of the figure, the aluminum angle can be seen protruding out of the grips.

Fig. 3-22 Tensile failure of prestressing strand.

The tensile stress-strain behavior from four strand tests is shown in Fig. 3-23 . A single strand was removed and tested from each pole specimen and was assumed to be representative of the other strands in the specimen. The extensometer was prematurely removed during Pole 3 test 1 and therefore a second test was conducted for this specimen. The strain hardening and necking portion of the stress strain curve are extremely short for high strength metals and the extensometer was removed prior to rupture to avoid damage therefor the total elongation was not captured by the sensor but was estimated based on the displacement of the UTM actuator after removal of the extensometer. The data collected from the strands indicates that the material corresponds to Grade 270 for all the pole

specimens.

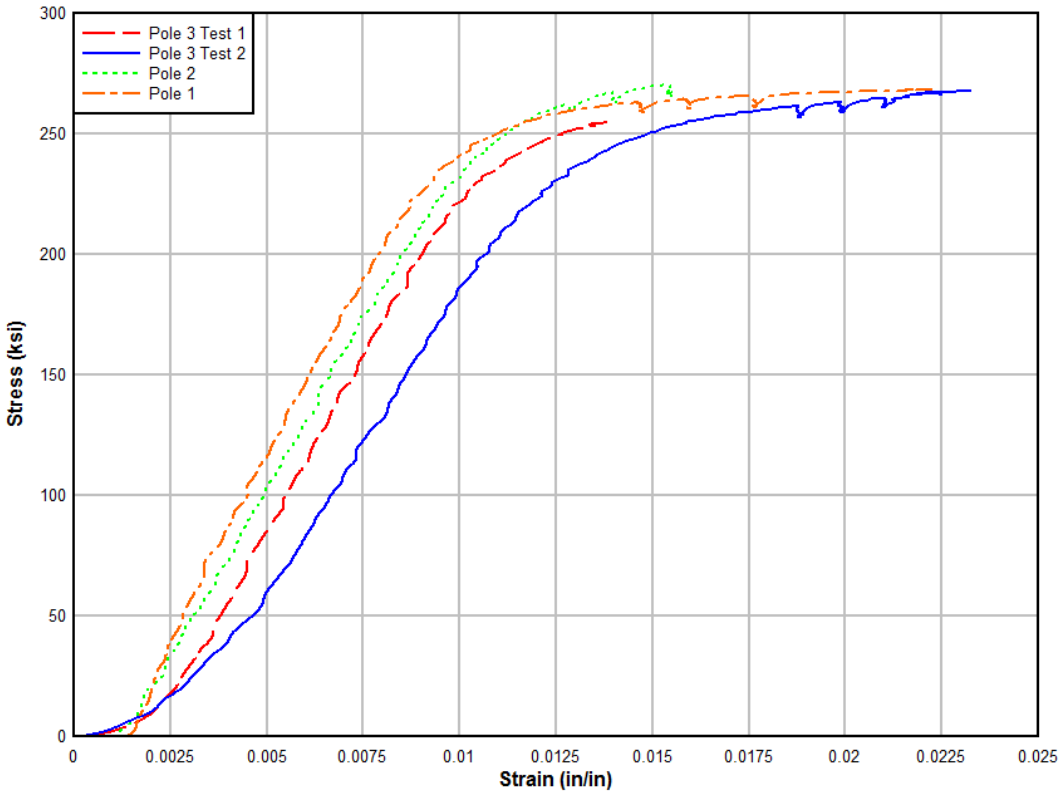

Fig. 3-23 Prestressing strand uniaxial tension stress-strain results for Poles 1-3.

3.2.2.3.1 Prestressing Loss Calculations

Prestressing loss calculations were performed in accordance with conventional methods (PCI 2004). The loss variables consisted of the concrete strength at both transfer and the expected value at 28 days. The modulus of elasticity was computed from concrete strength assuming normal weight concrete. The area of concrete, eccentricity, and moment of inertia were all taken based on the ground line cross section. Poles 1 and 2 contained a debonded strand but otherwise remain symmetric about the axis with negligible eccentricity while Pole 3 had ten strands divided into four on one flange and six on the

other which produces larger eccentricity. The weights of the poles were provided by EWEB. The values of input variables which were used to calculate the losses are provided in *Table 3-4*.

Table 3-4 Prestressing loss variables.

Variables	40 ft	70 ft
E_c (psi)	4030509	4030509
E_s (ksi)	28500	28500
Area (in^2)	156.7	206.1
Ecentricity (in)	0.55	1.18
Inertia (in^4)	3942.9	2564.8
# Tendons	10	10
# Debonded	1	0
Weight (k)	5.6	11.5

The prestressing losses from each component contributes a portion to the total losses within the specimen. The initial jacking force specified in the construction drawings was used to compute the initial stress in the strands. The losses from all contributions produced approximately 20% loss in stress from the initial stress, as seen in *Table 3-5*. Given the age of the specimens, it is reasonable to see relatively large losses due to the time variable components such as creep which provided the most stress reduction. The remaining prestress in the strands for each of the pole specimens was used in subsequent analytical models. The prestressing in the model was achieved by imposing an initial strain which is a done by converting the stress by way of modulus of elasticity for the strand.

Table 3-5 Calculated Prestressing Losses

Loss Variables	40 ft	70 ft
Elastic Shortening (ksi)	11.5	10.7
Shrinkage (ksi)	5	5
Creep (ksi)	18.9	18.3
Relaxation (ksi)	3.2	3.4
Prestress Lost (ksi)	38.6	37.4
Stress (ksi)	150.3	151.5
PS Loss (%)	20.4	19.8

3.2.3 Structural Testing

Three specimens previously described as Pole 1, 2, and 3 were tested to destruction in the Structural Engineering Research Laboratory at OSU. Five tests were performed: cyclic and monotonic for Pole 1; cyclic and monotonic for Pole 2, and cyclic for Pole 3 as shown in Table *3-6*. The test setup placed the poles within a roughly 9.5 ft length comprised of steel springs that represent the foundation to simulate soil-structure interaction during tests. The pole was loaded with a servo-hydraulic actuator located 18.5 ft. from the ground line of the foundation apparatus. The location of the actuator was chosen based on time-history analyses of model poles using OpenSees. The analytical model simulated the response of a structure within elastic soil springs under sinusoidal loading as well as earthquake ground acceleration from the Tahoku earthquake in 2011. The maximum moment and corresponding shear predicted from the analysis at the ground lien, which was expected to be the critical location, were used to compute the equivalent moment arm for placement of the. This moment arm, with constraints associated with the locations of strong floor anchor points, resulted in the final moment arm used during tests of 18.5 ft from the ground line.

Table 3-6 - Structural Test Matrix.

Specimen	Orientation	Test Conducted	Adjustments
Pole 1	Weak Axis	Cyclic	None
Pole 1	Weak Axis	Monotonic	Spacer and Instrumentation
Pole 2	Strong Axis	Cyclic	Spacer and Actuator Assembly
Pole 2	Strong Axis	Monotonic	Spacer, Instrumentation, and Actuator Assembly
Pole 3	Weak Axis	Cyclic	Spacer

Fully reversed cyclic loading was conducted for each of the pole specimens. The intention of the test was to investigate the behavior of the poles through increasing amplitude cycles with full stress reversal. These are commonly used to assess seismic performance by characterizing the initial stiffness, the amount of energy dissipated, progression of damage, and deterioration of resistance from repeated cycles.

After cyclic tests, monotonic tests were conducted for Pole 1 and 2. The undamaged upper portion of the pole was used in these tests. The specimens were embedded further within the simulated soil spring apparatus to allow the undamaged section to be located above the ground. This test section was then subjected to increasing amplitude deformation by pushing in only one direction. Due to tapering of the pole cross section along the length, adjustments were required to accommodate the smaller cross section of the specimen within the test setup.

The following sections describe the foundation apparatus, springs, actuator assembly, instrumentation, and loading protocols used in the experimental program.

3.2.3.1 Soil Spring Simulator

The test apparatus was designed to permit soil-structure interactions between the concrete pole and the foundation. Due to the size of the specimens, the orientation of the setup had

to be designed to fit within the laboratory strong floor. The tests were conducted by placing the pole in a horizontal orientation to fit within the building. The soil was represented with a series of elastic springs made of steel plates that were distributed over the embedded region of the poles.

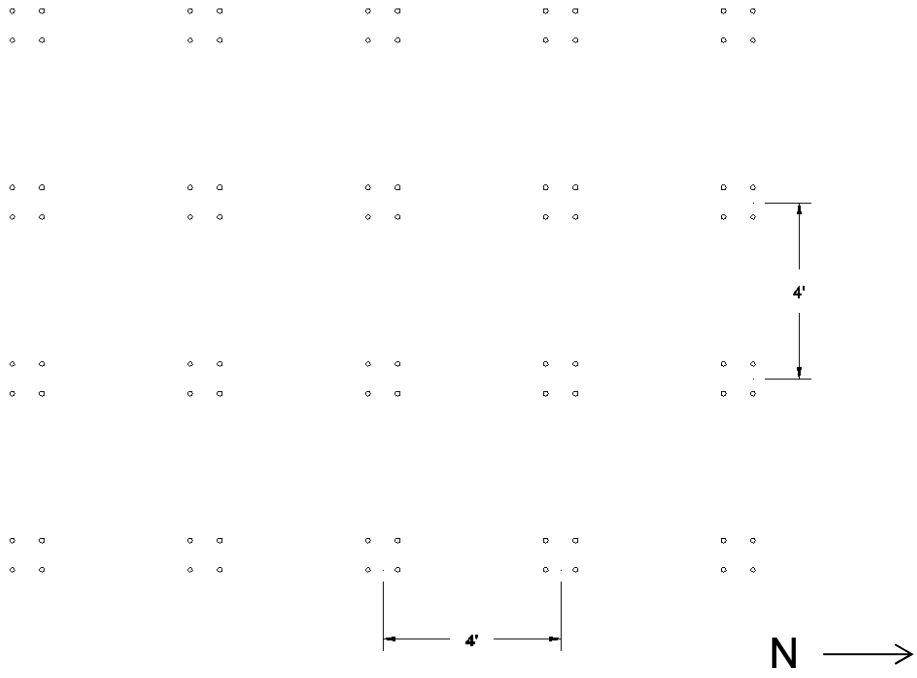

Fig. 3-24 Strong Floor Layout.

The base of the apparatus was fastened to the strong floor within the structures laboratory. The strong floor is a 5 ft deep heavily reinforced concrete slab that allows for beams to be securely fastened to the ground. The strong floor is laid out in a grid pattern 4 ft on center for connection points as seen in Fig. 3-24 Strong Floor Layout.. The connection to the floor is by four 1¼ in. diameter treaded rods that are 8 in. on center from each other forming a square pattern. Two W12x120 steel sections spanning 5 ft 4 in. in length, with stiffeners throughout, were placed at locations which allowed for alignment with the strong floor

connection points. The configuration of the locations of the floor beams can be seen Fig. 3-25. Fig. 3-26 shows a W12x120 floor beam that was used during testing.

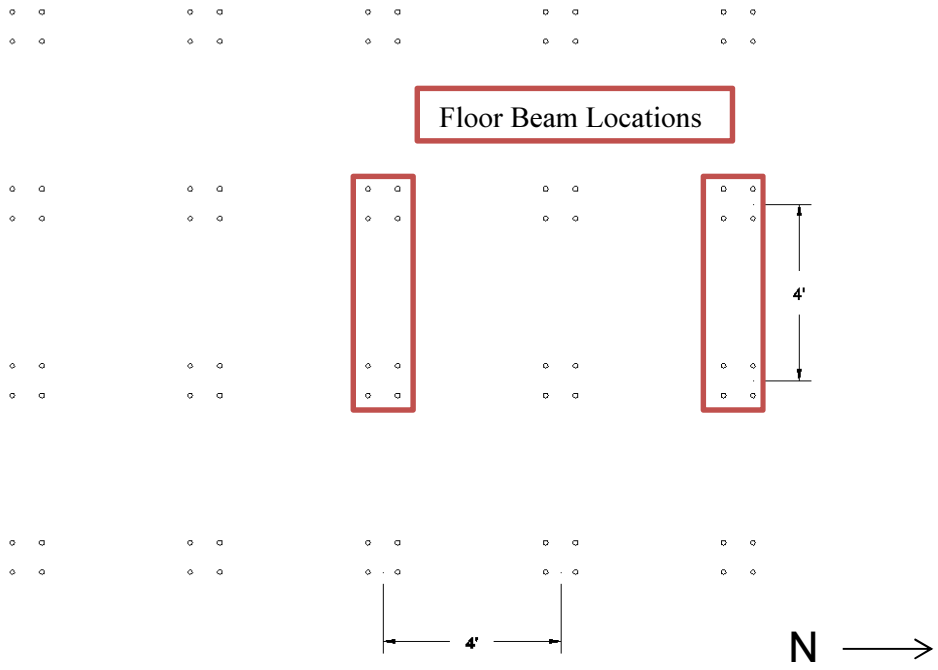

Fig. 3-25 Floor beam locations in reference to strong floor.

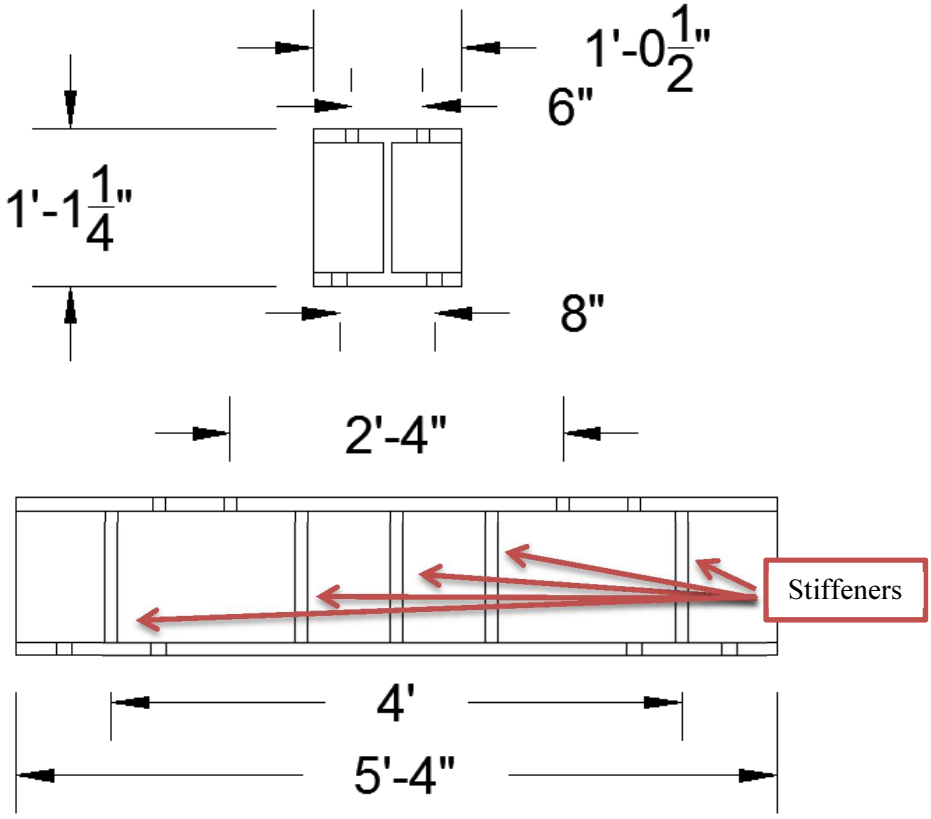

Fig. 3-26 W12x120 Floor beam.

New holes were drilled into the floor beams using a magnetic-base drill to space the W14x159 columns the appropriate distance for the steel plate springs to align properly. This distance was chosen to be 28 in. from hole to hole.The spacing of 28 in. was chosen by calculating the depth in which a hole could be placed into the flange of the W14x159 before interfering with the fillet leading into the web and an additional clearance of 1 in. was provided for the specimen at its largest cross section from the flange of the W14x159. The existing holes made in the W12x120 were made for 1¼ in. bolts or threaded rod; the

new holes would be 1 1/16 in. made to fit one inch bolts from the W14x159 to the W12x120. The hole locations can be seen in *Fig. 3-26* for both the floor connections and beam connections.

The main body of the apparatus was made up by four W14x159s that were 23 ft 1/8 in. long being placed horizontally and stacked on top of one another to make two stacks oriented in the North-South direction of the laboratory. The W14x159s were separated vertically by shorter W12x120 sections that were 17 in. long at a location 23 7/16 in. on center from the southern edge of the W14x159. A separate spacer was made using a W14x159 with a length of 17 in. and placed at a location 10 ft. 1 9/16 in. from the southern end. The locations for the spacers allowed alignment with existing holes in the W14x159 and W12x120 spacers as well as being over the top of the floor beams. By having spacers of different heights running along the length of the W14x159s, the setup had a taper that allowed better fit for the springs to the specimen. Connections of the W14x159s to the spacers and to the floor beams were all done with 1 in. A325 structural bolts. Fig. *3-27* depicts the apparatus prior to springs and specimen being placed.

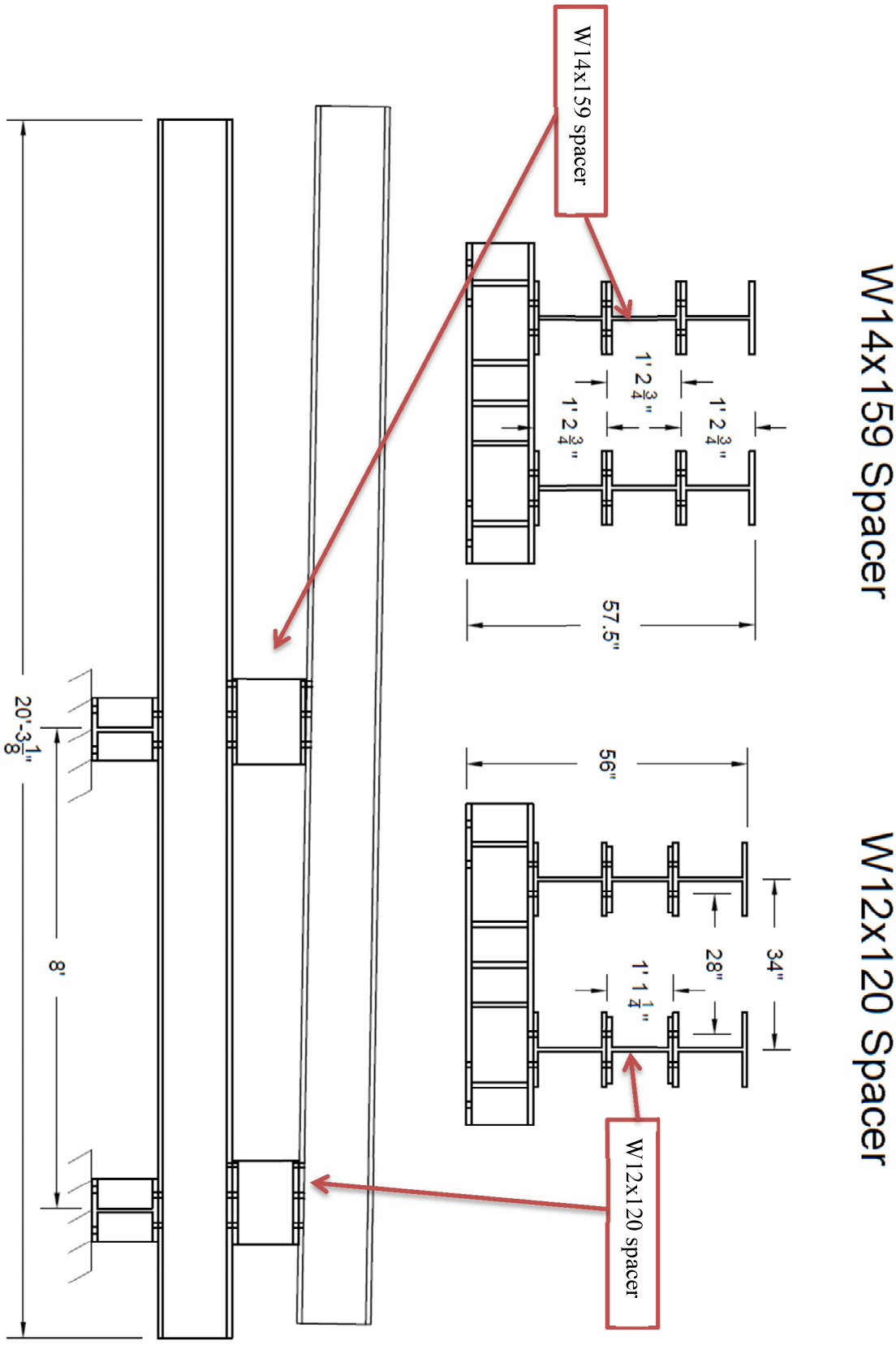

Fig. 3-27 Foundation apparatus without springs.

The springs used to represent the soil within the embedded region of the pole were designed to act as leaf springs and remain linear elastic during testing. The springs only provide compressive reactions to the pole. Assuming a 6in spacing of the springs along the embedded length and the width of the pole, a soil spring constant of 2.6 kip/in was estimated for the Willamette Valley soil (Stuedlein 2016). This low stiffness would result in large deflections that could not be properly accommodated in the present laboratory and would not permit testing the pole to failure (either the displacement limit of the setup would be reached or soil failure would occur first). It was determined that it was not feasible to match both the soil stiffness and strength required and thus the actual springs had to be designed to provide higher stiffness than that expected in the native soils.

The predicted spring constant for the plates was established through a two-step process which entailed the calculation of the displacement and then the spring constant. The springs were modeled as simply supported beams with a concentrated load at midspan. The displacement at midspan was computed as:

$$\delta = \frac{PL^3}{48EI} \qquad [2]$$

Where E is the modulus of elasticity, P is the applied load, I is the second moment of area, and L is the span length. The maximum load was predicted to be 5.45 kips based on the analysis results from OpenSees a pole model with linear springs spaced the corresponded experimental set up along the length of the embedment depth. The displacement of the spring model associated to this load was determined to be 0.61 in. Using the load in the spring and the spring displacement, δ, an elastic spring constant was computed as:

$$k = \frac{P}{\delta} \quad [3]$$

The spring constant for one ¾ in. thick and 4 in. wide plate was computed as 8.9 kip/in. This value was nearly three and a half times the desired amount for a soil spring. Due to high demands in the plate when the strength of the pole is achieved, a second plate was required to prevent yielding of the plate during testing. The plates were fastened only at the ends where the join to the flanges of the W14x159 sections. This allows slip along the interface and results in the plates acting as springs in series. The two plates placed in series produce a spring constant of 17.8 kip/in. The final spring design consisted of two plates stacked on top of one another, 1.5 in. thick, 4 in. wide, by 31 in. long. The plates had two 1 1/16 in. diameter drilled holes that were spaced 28 in. apart. The holes were drilled to match the holes along the flanges of the W14x159. The spring plates were bolted to the underside of the flanges of the W14x159, and thus did not interact with the steel flanges during deflection. The steel grade for the springs was chosen to be 50 ksi to prevent yielding the plates. The springs were placed every 6 in. on-center over a length of 9'-6". The test setup with the springs added is illustrated in Fig. 3-28. Fig. 3-29 gives perspective of the setup in the laboratory.

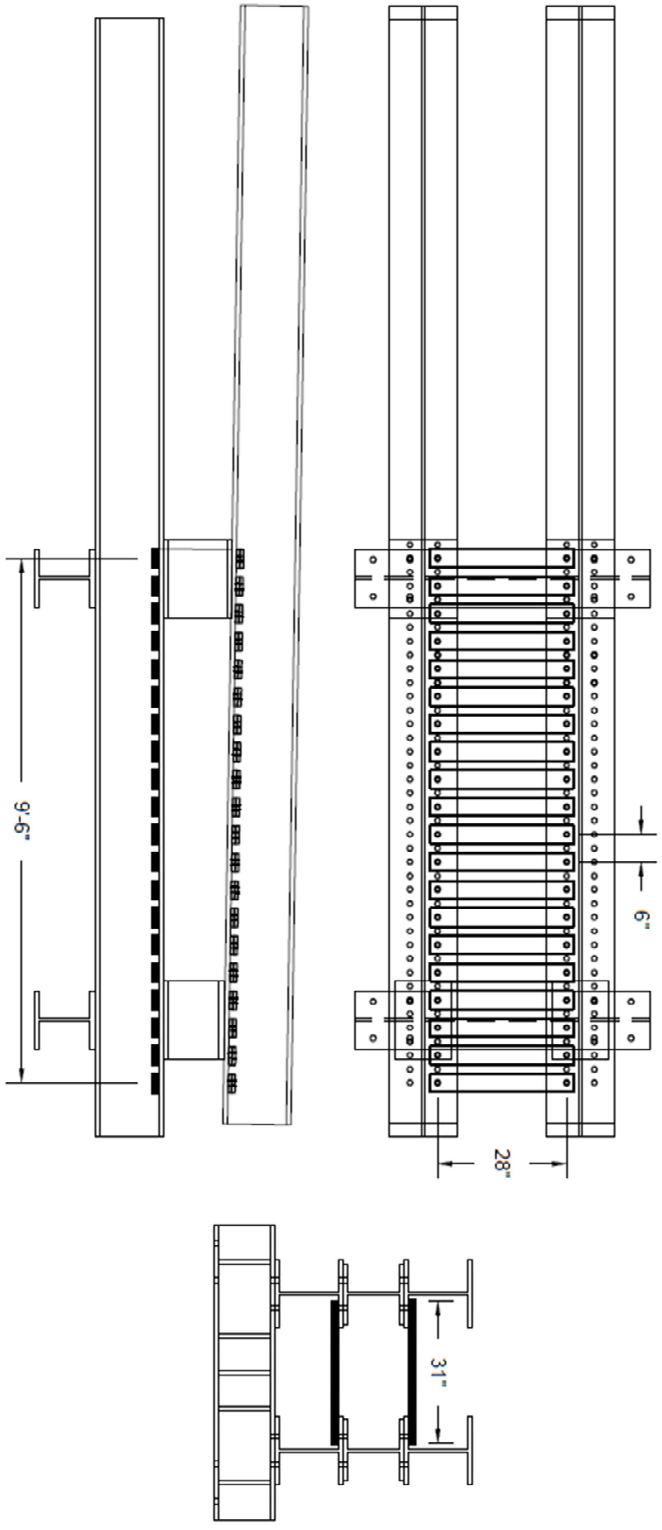

Fig. 3-28 Foundation apparatus with springs

Fig. 3-29 Construction of foundation setup prior to placement of specimen (springs shown across the bottom only).

To ensure that the springs would not accidently produce damage to the flanges of the poles due to uneven contact, square plates, ¾ in. by 4 in. by 4 in. were used to only permit loading over the webs in the strong-direction tests and specifically placed on the flanges for the weak-direction tests. In addition, due to the taper of the poles, ¼ in. by 4 in wide pieces of aluminum were placed over the length of the flange to permit bearing on all springs prior to testing as seen in Fig. *3-30*.

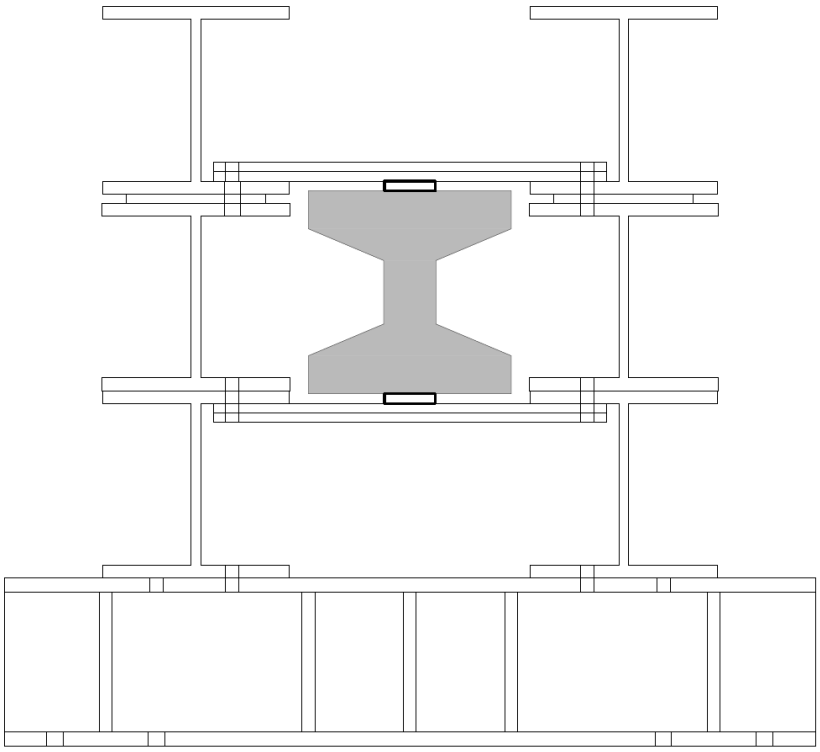

Fig. 3-30 Spacers positioned to load web exclusively.

The accumulation of ¾ in. spacers on both top and bottom springs created an additional 1.5 in. of space between spring locations. The additional space was accomplished by adding a 12 in. by 12 in. by 1.5 in. steel plate between the W14x159 beams.

3.2.3.2 Actuator

The load was applied to the specimens using a servo-hydraulic actuator. The actuator had a 30 in. stroke and a maximum load capacity of 135 kips in compression and 110 kips in tension at a working line pressure of 3500 psi.

The actuator was attached to a load frame that was bolted to the laboratory strong floor. The load frame consisted of two W120x120 floor beams and @12x120 columns. The load frame was connected to the strong floor using 1.25 in. diameter A193-B7 threaded rod. The actuator and load frame are illustrated in Fig. *3-31*.

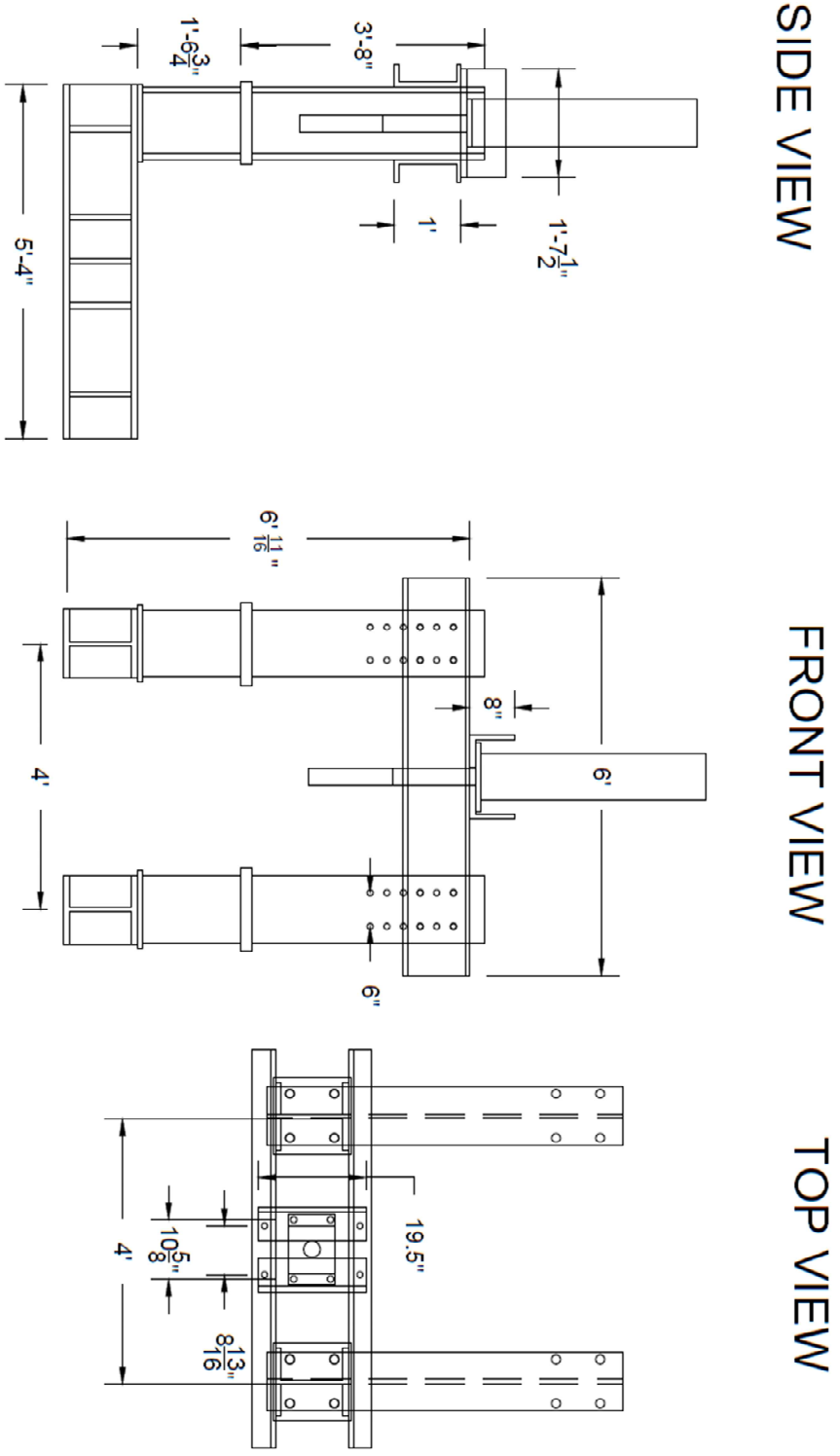

Fig. 3-31 Actuator Configuration.

A 150 kip capacity fatigue rated load cell was connected to the end of the actuator psiton. Two channel sections were used to connect the load cell to the specimen using 1 ¼ in. diameter threaded rod which allowed the actuator to both push and pull the specimen for cyclic lading. A 1/16 in. thick piece of copper plate was placed between the load cell and a steel channel that attached to the specimen to transfer the actuator load. Steel plates were used to transfer the applied force to the specimen at prescribed bearing locations. For weak axis tests, only the flanges were to be loaded. To evenly distribute the load onto the flanges ofer the width of the channel, two plates 4 in. by 6 in. by ¼ in. were welded to the channel aligning to the locations of the flanges. Fig. *3-32* displays the apparatus that connects the load cell to the specimen for the weak axis configuration. For the strong axis tests, two ¼ in. plates were replaced with a single plate of similar dimensions located over the web as shown in Fig. *3-33*. These arrangements prevented localization damage from occurring at the load application points.

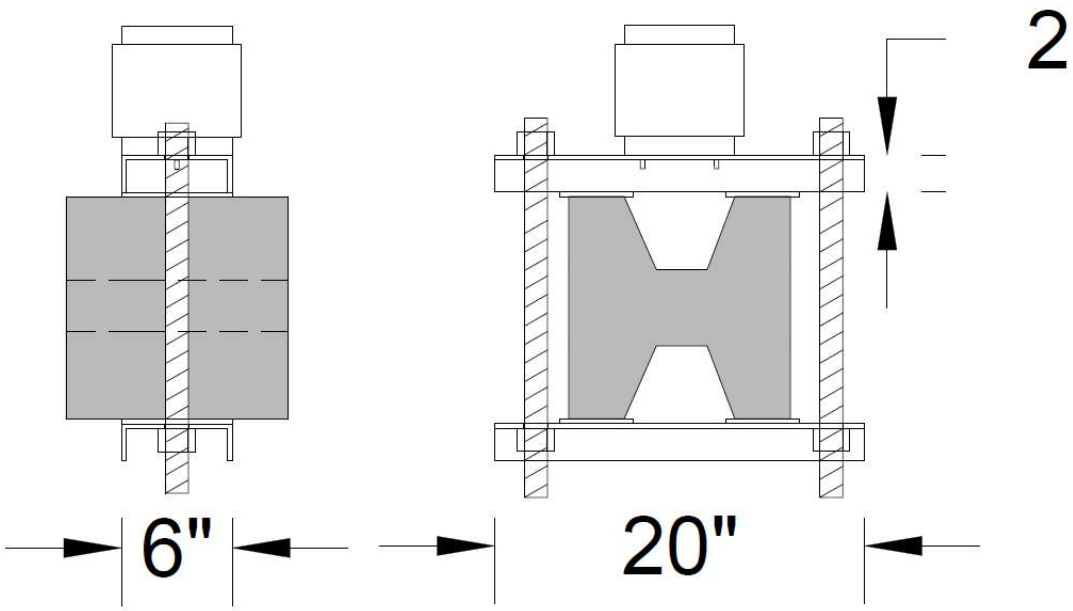

Fig. 3-32 Actuator connection to specimen.

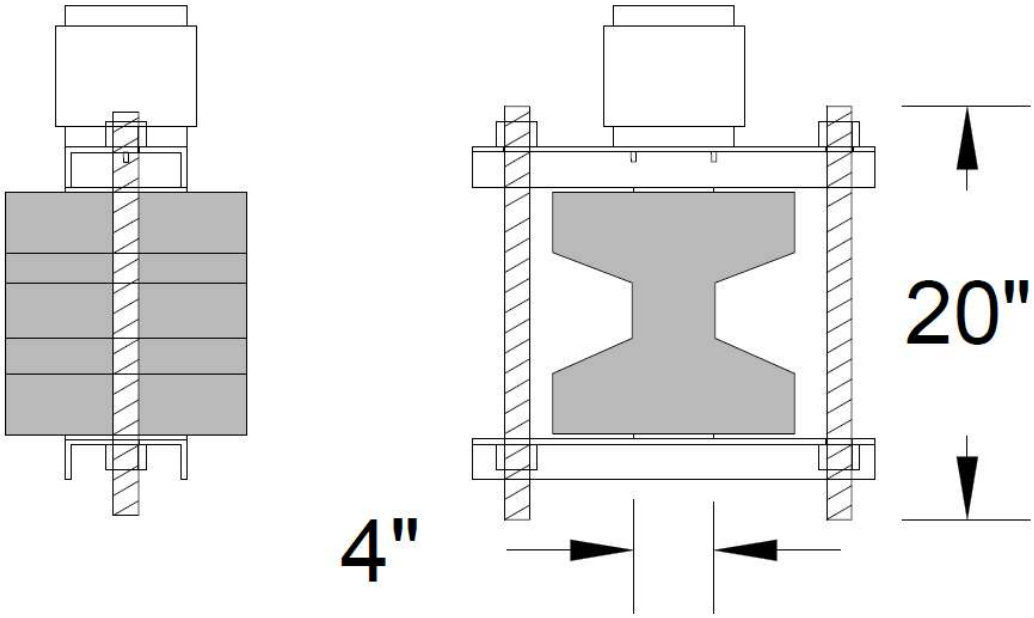

Fig. 3-33 Actuator connection for strong axis orientation.

3.2.3.2.1 Strain Gages

Strain gages were used to monitor the strain in the steel plate springs during tests. Strain gages were placed at the midpoint of the springs located on the top of the apparatus to prevent damage to the sensors during installation of the specimen in the setup. Seven strain gages were placed along the embedment depth as illustrated in Fig. 3-34.

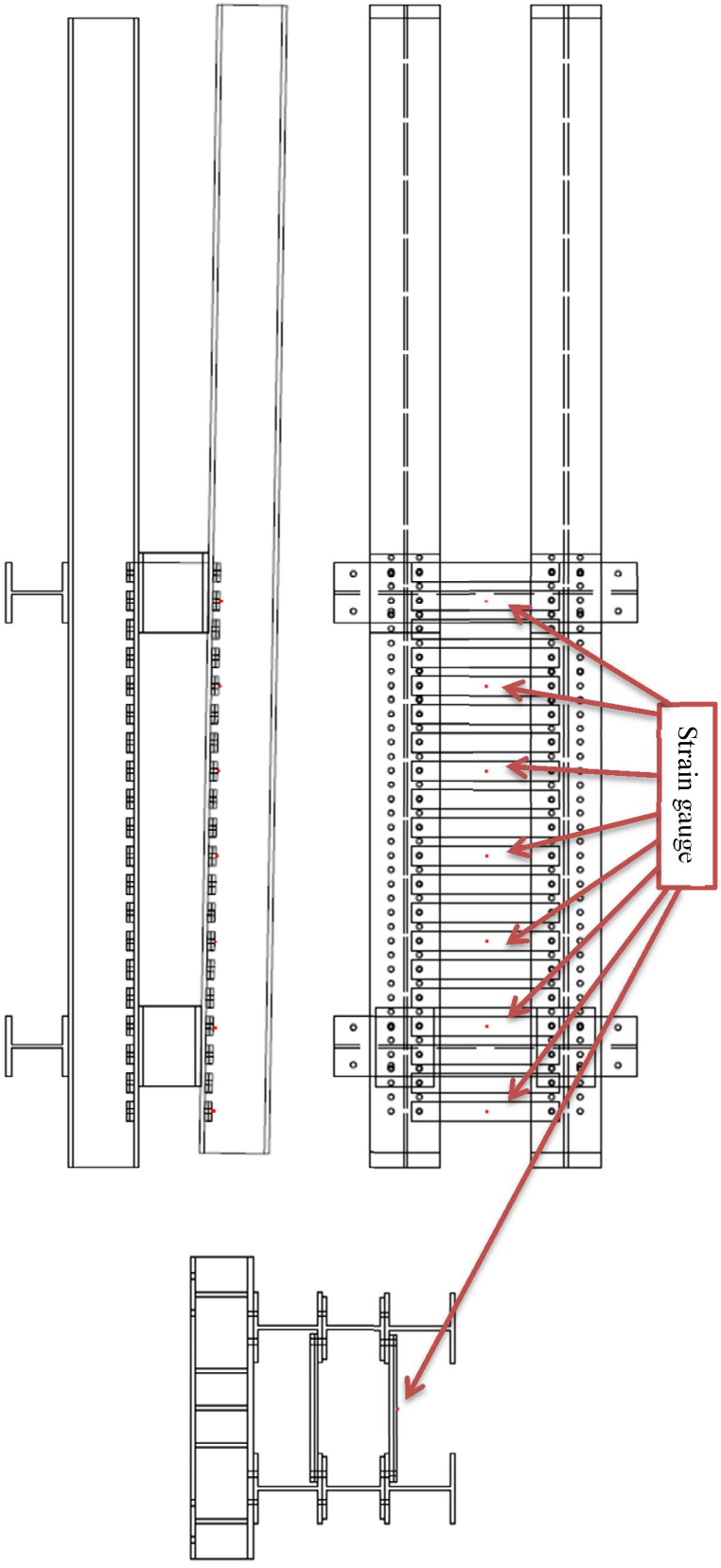

Fig. 3-34 Strain gage locations for tests.

3.2.3.2.2 Displacement Sensors

Displacement sensors were used to capture displacement of the specimens relative to the strong floor and to capture deformations occurring within the specimens. The sensors were string potentiometers and different lengthswere used based on the expected displacement amplitudes. Sizes included 2,4.7, 15, 20, and 30 in. stroke capacities. The string potentiameters placed along the specimen was used to measure curvature, and shear deformations at various sections near the ground line..

Weak axis displacement sensors were placed starting with the groundline location as this was the most crucial section. Locations, 18 in. above the ground line and two locations with 18 in. increments were observed below ground to capture all evident displacements. These locations served as the reference point for all other instrumentation locations. From the ground line, allighning with the 18 in. spacing, vertical displacement sensors were added through the embedment depth to provide displacements within the springs. A displacement sensor was then attached to the specimen at the location of the actuator. The location was at a 5 in. offset toward the groundline to provide clearance from the actuator assembley connected to the specimen. Two vertical displacement sensors were placed equal distant within the exposed specimen between 18 in. above ground line and the actuator to provide curvature information. All locations of displacement sensors for cyclic tests can be seen in Fig. *3-35*, Fig. *3-36*, and Fig. *3-37*.

Horizontal displacement and diagonal displacement were both monitored within the areas of interest around the ground line. One section above and two sections below groundline were monitored with top and bottom horizontal displacements as well as diagonal displacements.

After performing the first test, the locations of the diagonal and horizontal displacmeent sensors were adjected to be 36 in. above and below ground line to fully capture the region in which failure was observed .

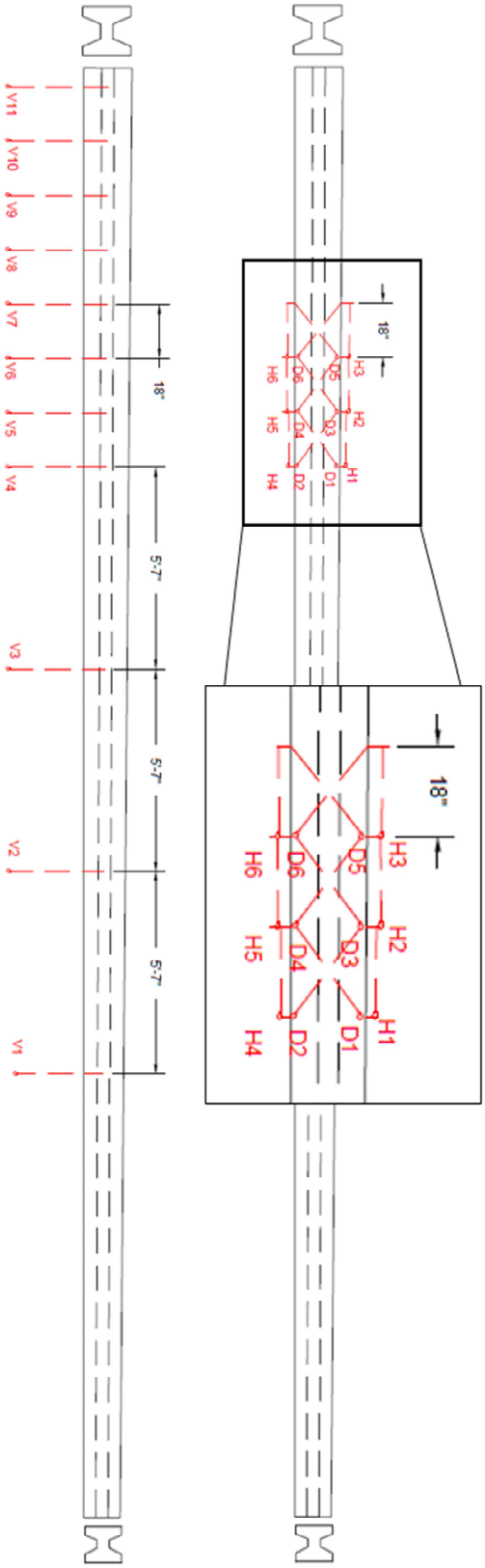

Fig. 3-35 Vertical, diagonal and horizontal displacement sensors for Pole 1 cyclic testing.

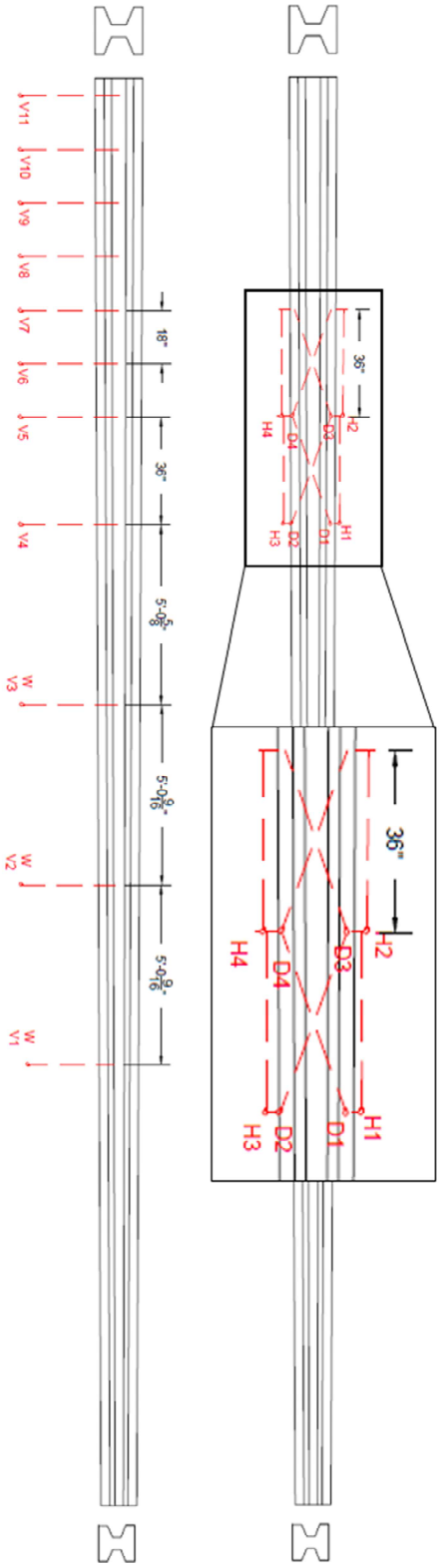

Fig. 3-36 Vertical, diagonal, and horizontal displacement sensors for Pole 2 cyclic testing.

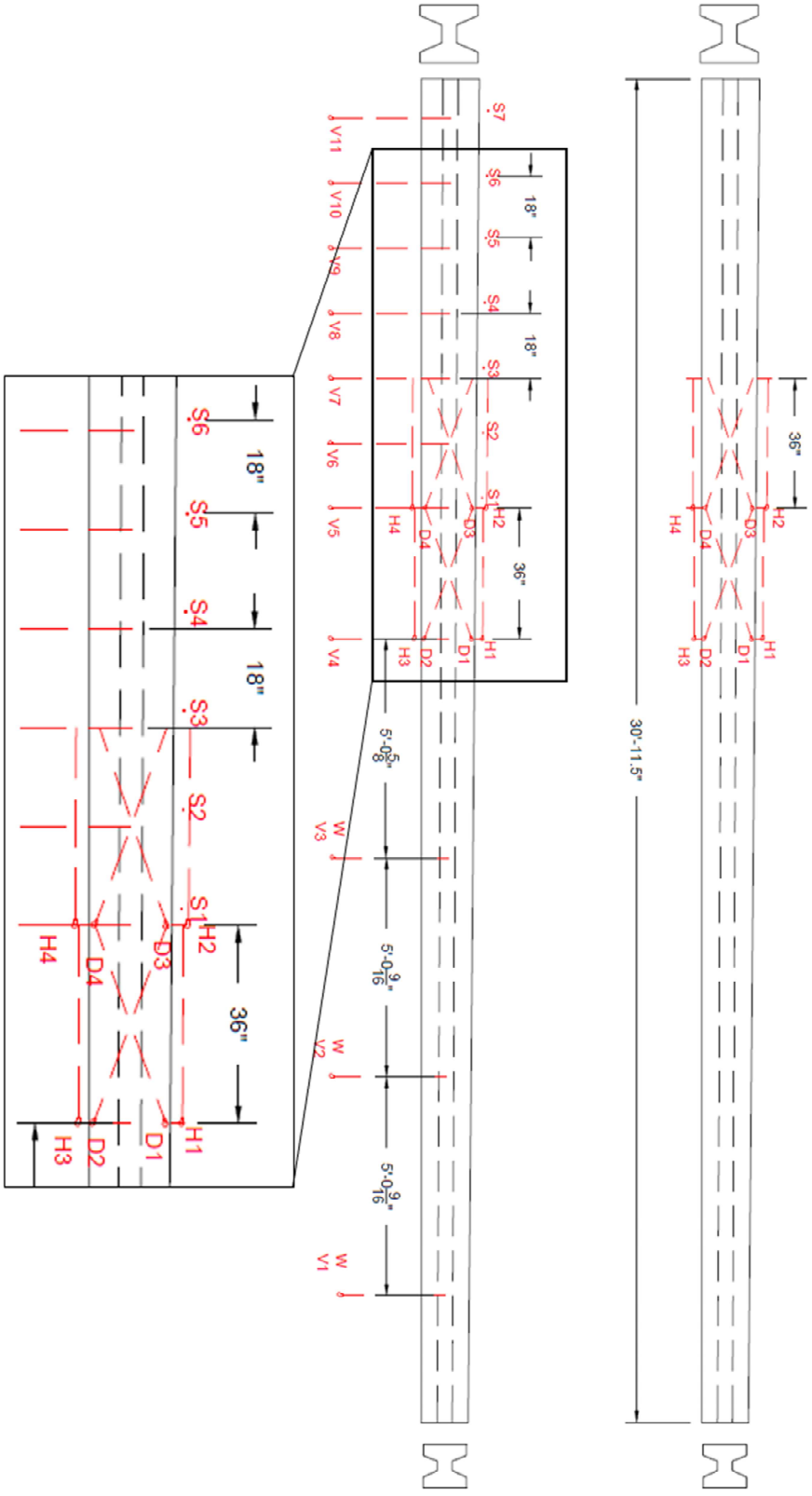

Fig. 3-37 Vertical, diagonal, and horizontal displacement sensors for Pole 3 cyclic testing.

Monotonic tests were conducted on a different cross section of the specimen and therefor the layout of string potentiameters was less extensive in capturing the diagonal displacements throughout the soil. Rotation of the beam was evident in the initial cyclic test and an additional vertical displacement sensor was placed on the opposing ground line side as to capture differential displacement. Montonic instrumentaion locations are protrayed for both Pole 1 and Pole 2 in Fig. *3-38* and Fig. *3-39*, respectively.

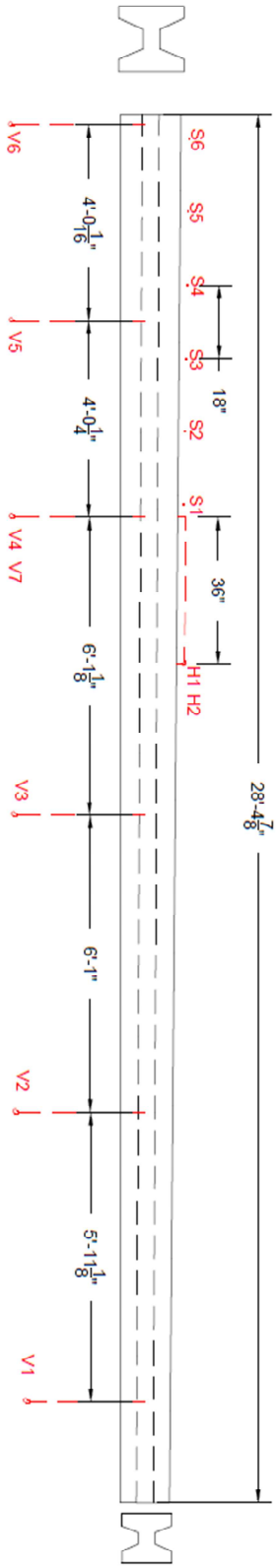

Fig. 3-38 Vertical and horizontal displacement sensors for Pole 1 during monotonic testing.

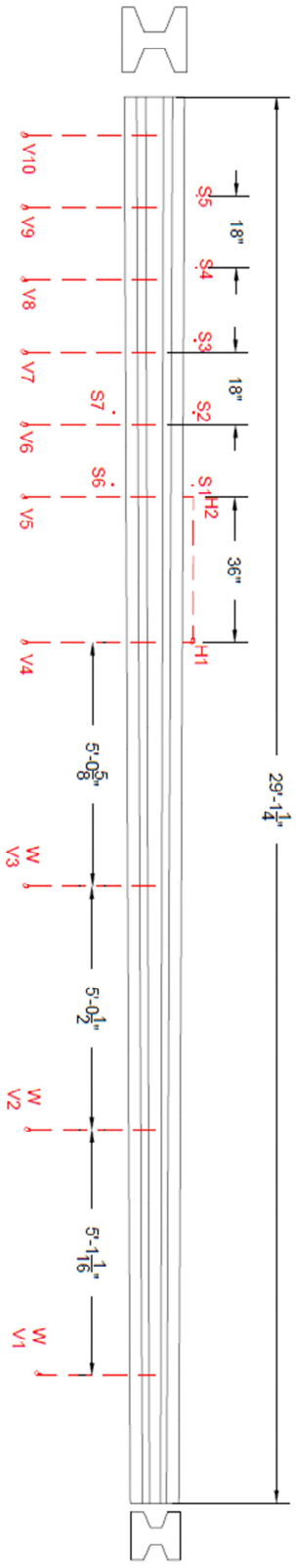

Fig. 3-39 Vertical and horizontal displacement sensors for Pole 2 during monotonic testing.

3.2.3.2.2.1 Linear Variable Differential Transformer (LVDT)

A linear variable differential transformer (lvdt) was used to measure the diplacement of the hydraulic actuator. The instrument was used as the feedback sensor for servo-hydraulic control of the actuator during testing uner displacment control.

3.2.3.3 Cyclic Loading Protocol

To establish the target displacement amplitudes, the yield moment of the cross section at the ground line needed to be determined. Once this is known, the required load and corresponding displacement can be computed based on the geometry used for the setup (the distance from the ground line to actuator was about 18.5 ft). The material properties provided by the plan drawings were chosen to represent the test.

A model of the cross section was developed using the analysis program Response2000 (Bentz 2000) to compute a theoretical yielding moment capacity based on the material properties provided in the construction drawings and the field measured overall section geometry. Based on the moment and moment arm of the experimental setup the deflection at the actuator location was computed assuming the pole acted as a cantilever beam as:

$$\delta = \frac{PL^3}{3EI} \qquad [4]$$

where δ is displacement at the actuator location, P is actuator applied load, L is distance between the ground line and actuator location, E is elastic modulus, and I is moment of inertia of the pole. Target displacement amplitudes were then obtained for the displacement control loading protocol. The displacement protocol for Pole 1, 2, and 3 for cyclic tests are

presented in **Error! Not a valid bookmark self-reference.**. After reaching each prescribed amplitude, the specimens were inspected to identify, mark, and record cracks or other visible distress.

Table 3-7 Pole 1 Cyclic Loading Protocol**.**

Yield	Pole 1	Pole 2	Pole 3
%	(in)	(in)	(in)
25	0.3	0.525	0.525
50	0.6	1.05	1.05
75	0.9	1.575	1.575
100	1.2	2.1	2.1
150	1.8	3.15	3.15
200	2.4	4.2	4.2

3.2.3.3.1 Monotonic Loading Protocol

Monotonic loading was conducted by applying force on the specimen in one direction only. The actuator slowly applied displacement to the specimen to increasing amplitudes until eventual failure. Displacements were suspended at intervals to inspect the specimens and identify and mark cracks. During these intervals the load was reduced to minimize creep effects.

4 Experimental Results

Five different structural tests were conducted for the poles in this research program. Pole 1 was tested in the weak-axis orientation and two tests were conducted; cyclic followed by monotonic. Pole 2 was tested in the strong-axis orientation and two tests were conducted; cyclic followed by monotonic. The final specimen, Pole 3, was tested in weak-axis orientation being tested cyclically. Material samples were taken post mortem from the specimens.

The nature structural testing of a full size specimen in a horizontal orientation permits there to be a self-weight measured at the load cell. T0 account for the load, an average of the strains within the steel plate springs throughout testing was investigated. The load corresponding to the average engagement of the outer-most springs was taken as the load when the pole was a neutral position. The load was then corrected and the corresponding displacement at the load after the first few cycles, to remove initial system inaccuracies, was adjusted.

4.1 Structural Results

The goal of the structural tests was to gain insight into the cyclic performance of the poles in both strong and weak axis orientations to and thereby infer their seismic resistance. All specimens failed due to the concrete in the flanges rupturing in compression with “bird-caging”, or the prestressing strand twisting to form a cage, by the individual strands. Capacities of each pole were taken as the maximum applied load multiplied by the distance from actuator applied load to failure location on the pole. The list of capacities for each test is shown in *Table 4-1*.

Table 4-1 Experimental Pole capacities.

Test	Capacity (k-ft)
Pole 1 Cyclic	106.5
Pole 1 Monotonic	72.3
Pole 2 Cyclic	170.4
Pole 2 Monotonic	146.7
Pole 3 Cyclic	125.7

4.1.1 Pole 1

4.1.1.1 Test 1 Results

The inclusion of the simulated soil through the use of springs required a thorough separation of the different deformations that contribute to the displacement of the pole at the actuator location. The applied load for each step of cycles aligned with the previous cycle and deviated when cracking initiated. In *Fig. 4-1* A) cracking of the specimen can be seen to occur at nearly 4 kips when the pole starts to behave nonlinearly elastic. The slope of the load-displacement response begins to soften followed by failure. The displacement in the negative direction, (push cycles), resulted in failure of the specimen and in completing the cycle lead to the load capacity dropping off in subsequent cycles and steps. The maximum absolute moment that was reached prior to failure in the negative direction and was 106.5 k-ft.

The displacement of the pole was broken into the components produced by bending within the pole, rigid body rotation, and translation due to the simulated soil springs shown in Fig. *4-1*. The translation was very small in comparison as it accounted for the springs settling due to the load of the beam being fully engaged to the springs after removal of supports. Rotation of the pole within the foundation has little effect until higher load cycles when the springs are fully engaged. The displacement due to bending of the pole contributes the most to the total tip displacement and can be seen in Fig. *4-1*. Upon Pole 1 failing, the load drops significantly while allowing further bending displacement as seen in Fig. *4-1* D).

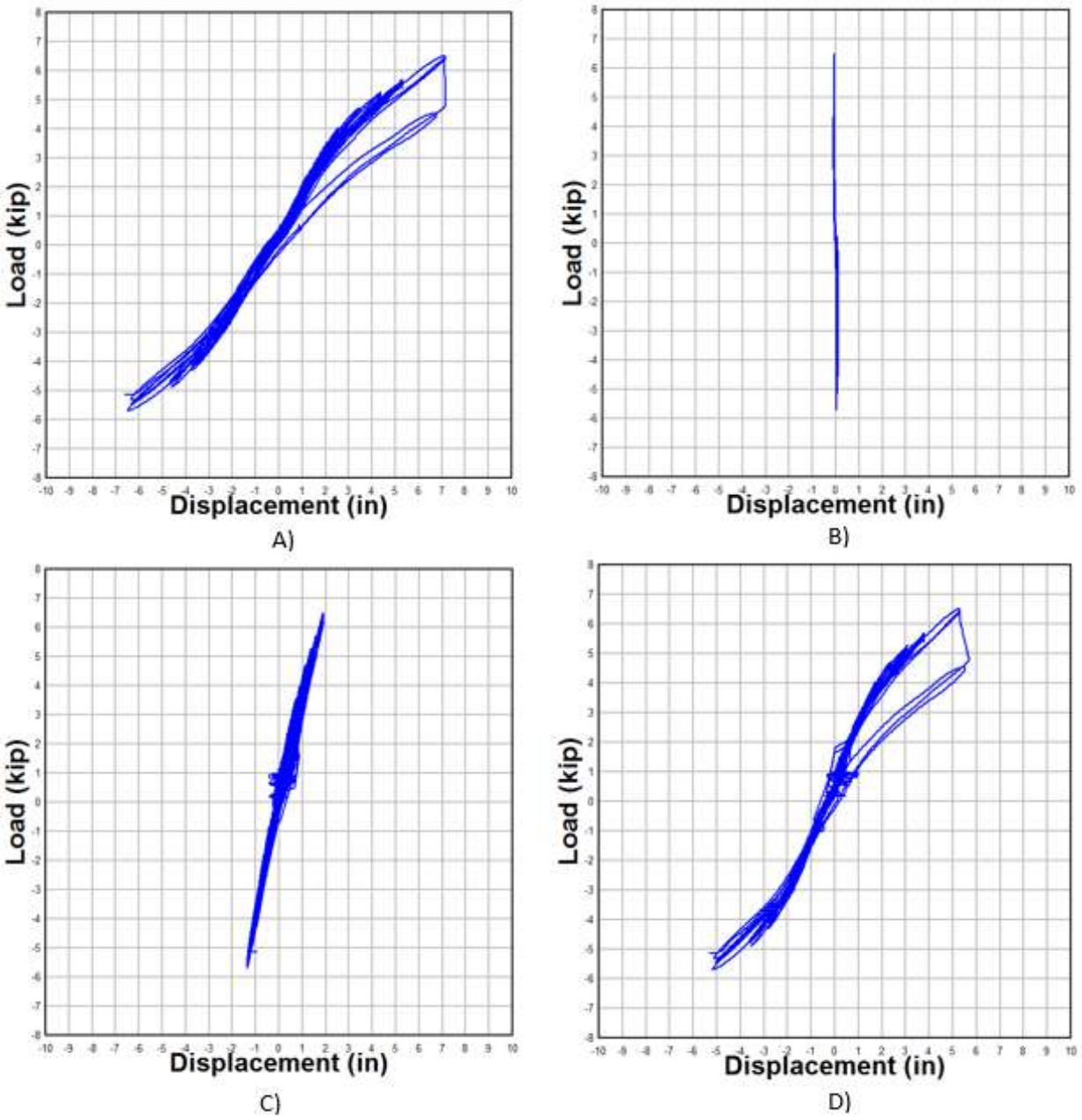

Fig. 4-1 A) Tip displacement, B) translational displacement of the steel plates, C) tip displacement due to rotation within the springs, and D) bending displacement at the tip for Pole 1 during cyclic testing.

Due to continued cycles in both the positive and negative direction as seen in Fig. *4-1*, the failure of both compression faces in the extreme fibers of the flanges spalled exposing the prestressing strand and transverse reinforcement. The remains of the cross section just above the ground line after both failures can be seen in *Fig. 4-2*.

Fig. 4-2 Pole 1 after both positive and negative failure.

Fig. 4-3 presents the steel spring strain during increasing amplitude cycles for Pole 1. The spring stiffness stays relatively consistent from top to bottom with the exception of the ground line spring. The ground line spring, labeled WS1 was engaged the most and saw the larges displacement among the embedment springs. The orientation of the foundation and possible differential tightening of the bolts that fasten the spring to the specimen could lead to an overall stiffer spring.

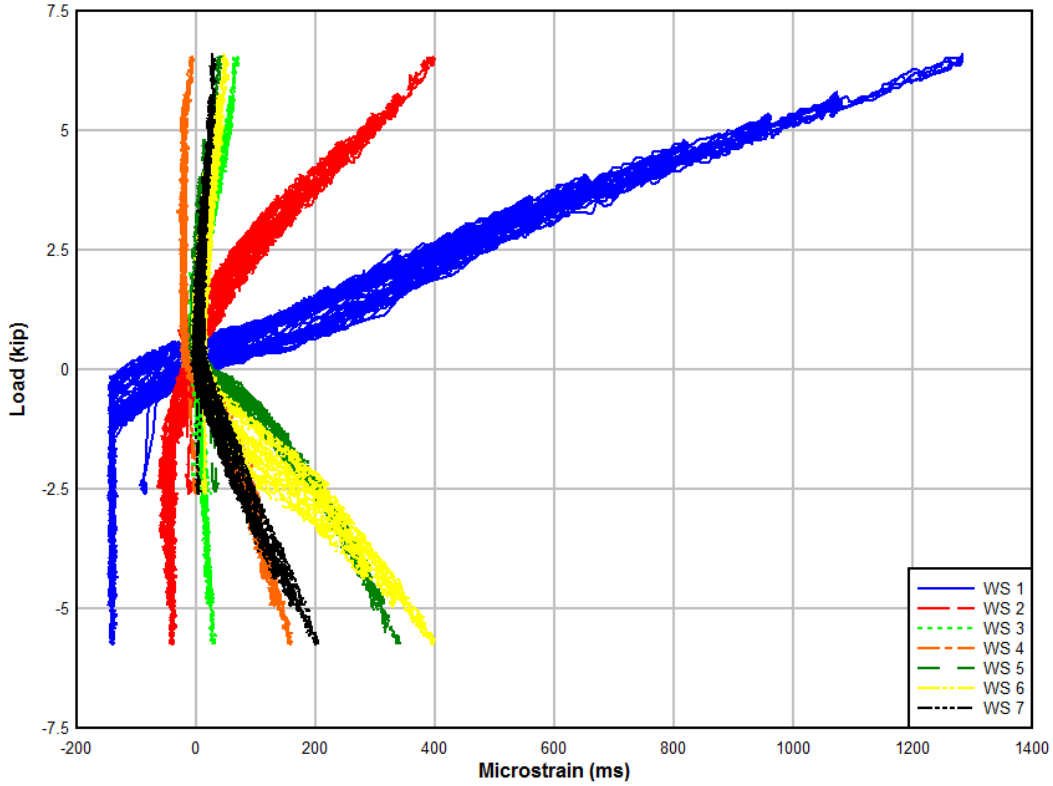

Fig. 4-3 Steel plate spring strain vs load for Pole 1.

The neutral axis for the cross section at ground line for Pole 1 shows a difference when loading positively and negatively. *Fig. 4-4* represents the neutral axis trend for Pole 1 during cyclic testing. The trend for the depth of the neutral axis is shallow when pushing the pole down as opposed pulling up. The neutral axis when pulling up is nearly twice as deep at a depth of about 6 in. The accuracy of the location of neutral axis when approaching small loads leads to impossible neutral axis depth.

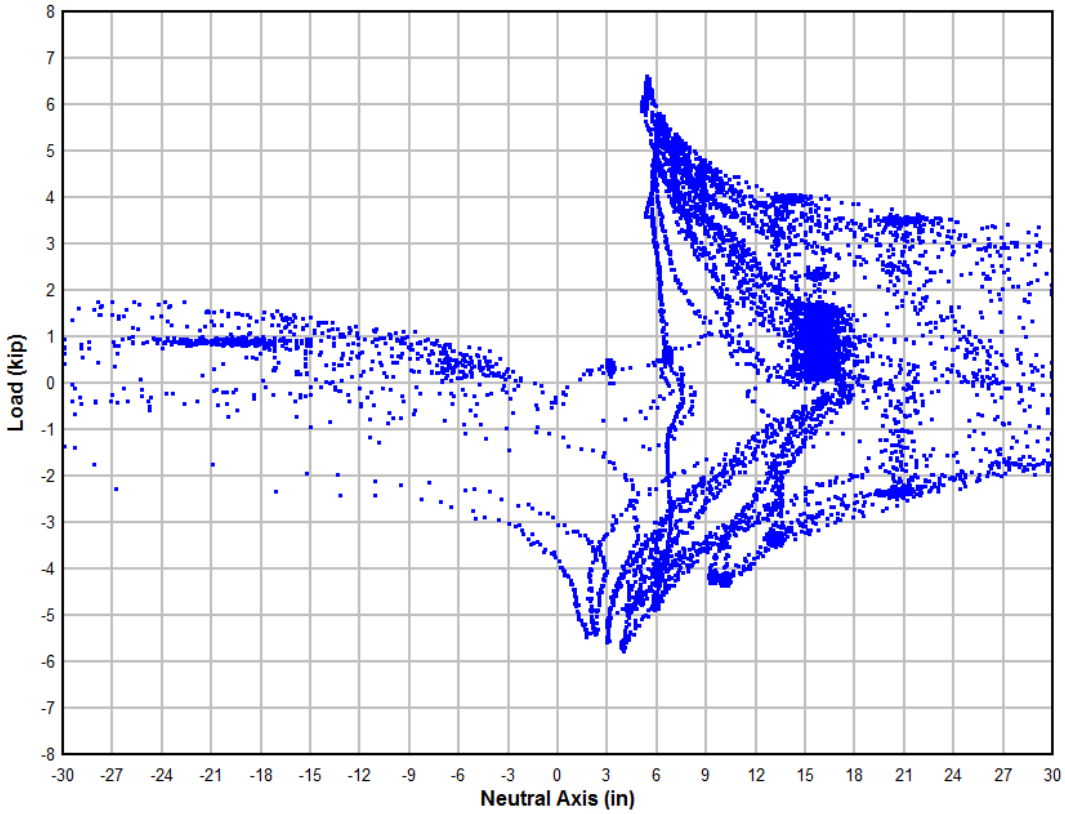

Fig. 4-4 Depth of neutral axis of Pole 1 during cyclic testing.

The curvature of Pole 1 above ground compared to below ground shows the effect of bending outside the simulated soil foundation. *Fig. 4-5* allows a comparison of pole curvature between the section immediately outside the foundation against the section within the foundation. The extent of the curvature outside the foundation after failure leads to large readings of curvature due to a hinge forming within the measured region. The section monitored within the foundation shows the effect of friction within the system between springs, flanges, and bolts. The slight resistance results in load drop-off while the pole remains in the location.

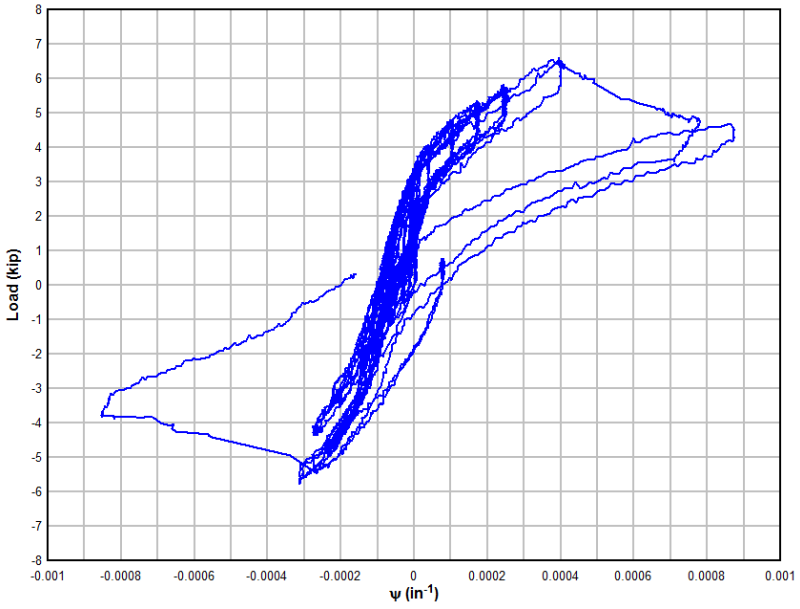

A)

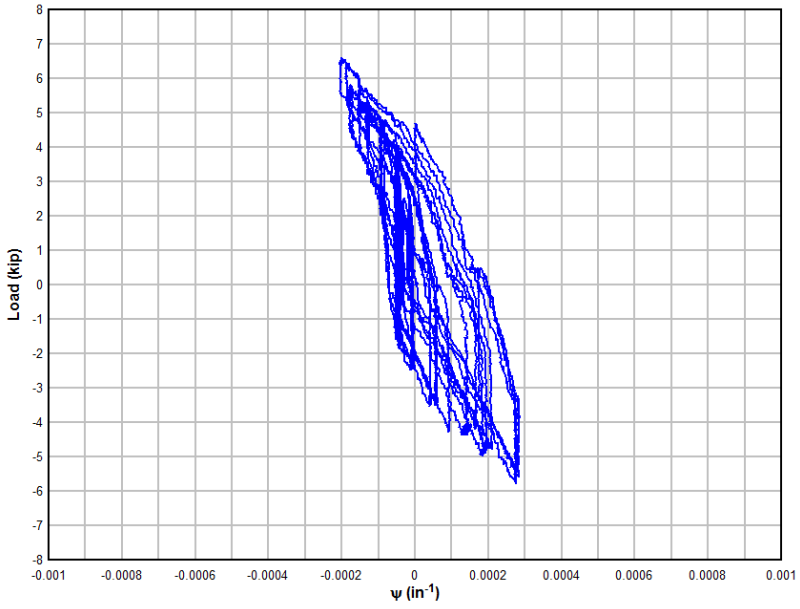

B)

Fig. 4-5 A) Curvature of section above ground, B) curvature of section below ground from cyclic loading of Pole 1.

The diagonal displacement of the three monitored sections is shown in Fig. *4-6*. The first section shown in figure A indicates that vertical cracks formed at small during initial cycles. As the cycles continued, the section experienced cracking parallel to the first displacement sensor which was consistent with cracks observed during testing. The two sections within the ground show parallel cracking with the diagonal sensor running from bottom to top. The two sections below ground line mirror the cracks formed above the ground line, these cracks were caused by shear from the resulting force from the ground line spring. The sensor for the top diagonal displacement in the second section shows a shift into negative displacement which is most likely a results of sensor malfunction.

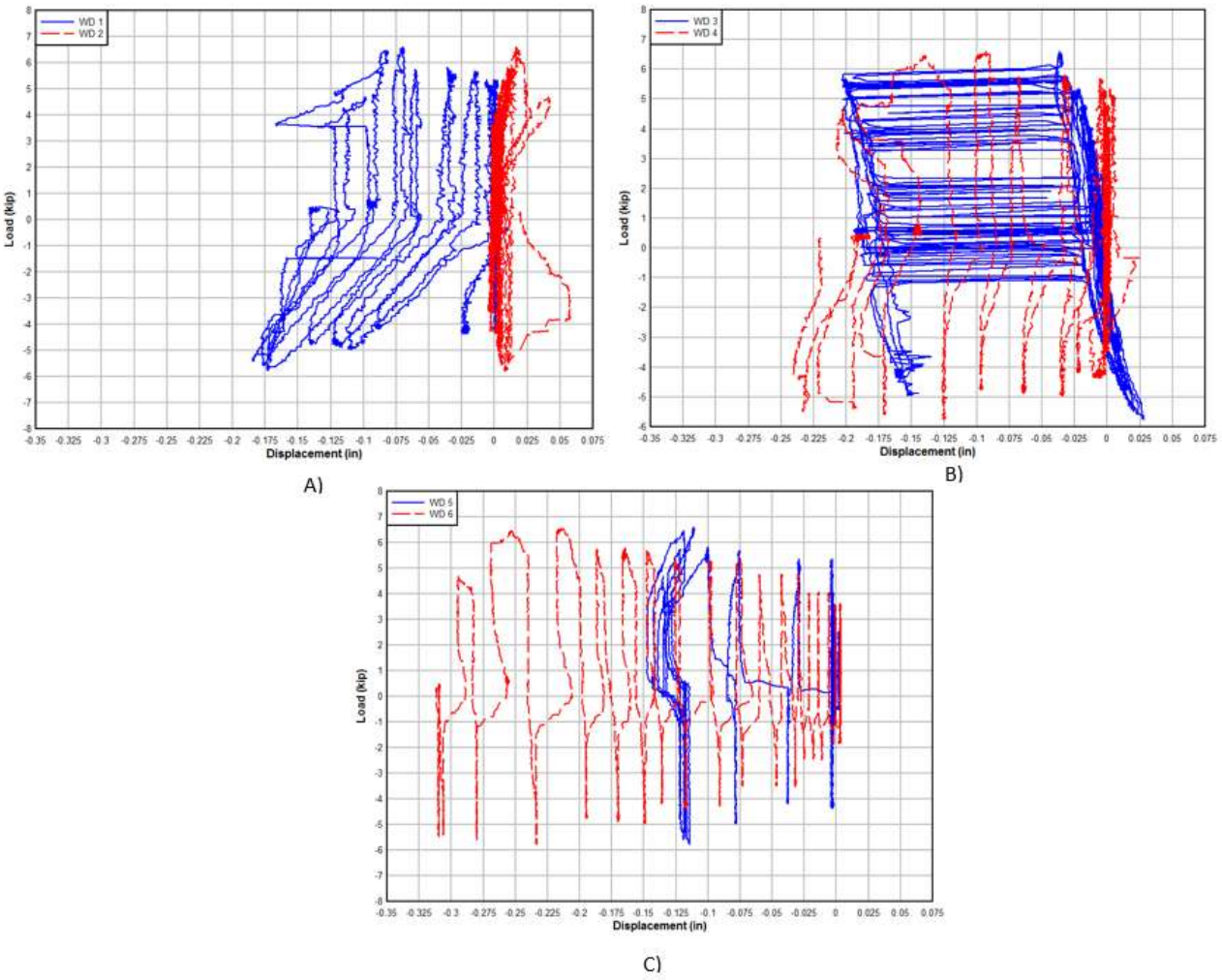

Fig. 4-6 A) Diagonal displacement within section 1 above ground line, B) diagonal displacement immediate below ground line in section 2, C) diagonal displacement in lowest section critically monitored.

4.1.1.1.1 Simulated Soil Response

Soil spring displacements refer to the vertical displacement of the pole specimens located throughout the embedment depth springs at 18 in. intervals. The displacements were taken from the first step of each cycle and are labeled in numerical order of increasing amplitude. The results include both positive and negative displacements at each cycle and indicate the average angle of rotation in radians. The center of rotation is illustrated with a red dot for reference. The distance from the ground line to the location of the sensor or spring labeled on the X-axis with units of in. while vertical displacement are located on the Y-axis and also with units of in.

The angle of rotation and amplitude of displacement grew with each displacement cycle as expected as shown in Fig. *4-7*. The results clearly show soil deformations and rotations displacementup to nearly 0.4 in.. The first negative cycle produced very small results that cannot be distinguished at the scale presented. The small displacements in the first several cycles, except for the furthest sensor reading larger displacements, were expected as all the springs were not yet fully engaged on the specimens due to uneven and nonuniform contact surfacesdisplacement The rotation within the springs and the location of the center of rotation allowed correction of the tip displacement for foundation rotation and translation. The rotation grew to an angle of 0.0072 radains at the larges amplitude cycle in the postive position resulting in a displacement at the tip of 1.89 in. Failure of the pole was just over 6 in. upon comparing to Fig. *4-1* showing rotation displacement was significant

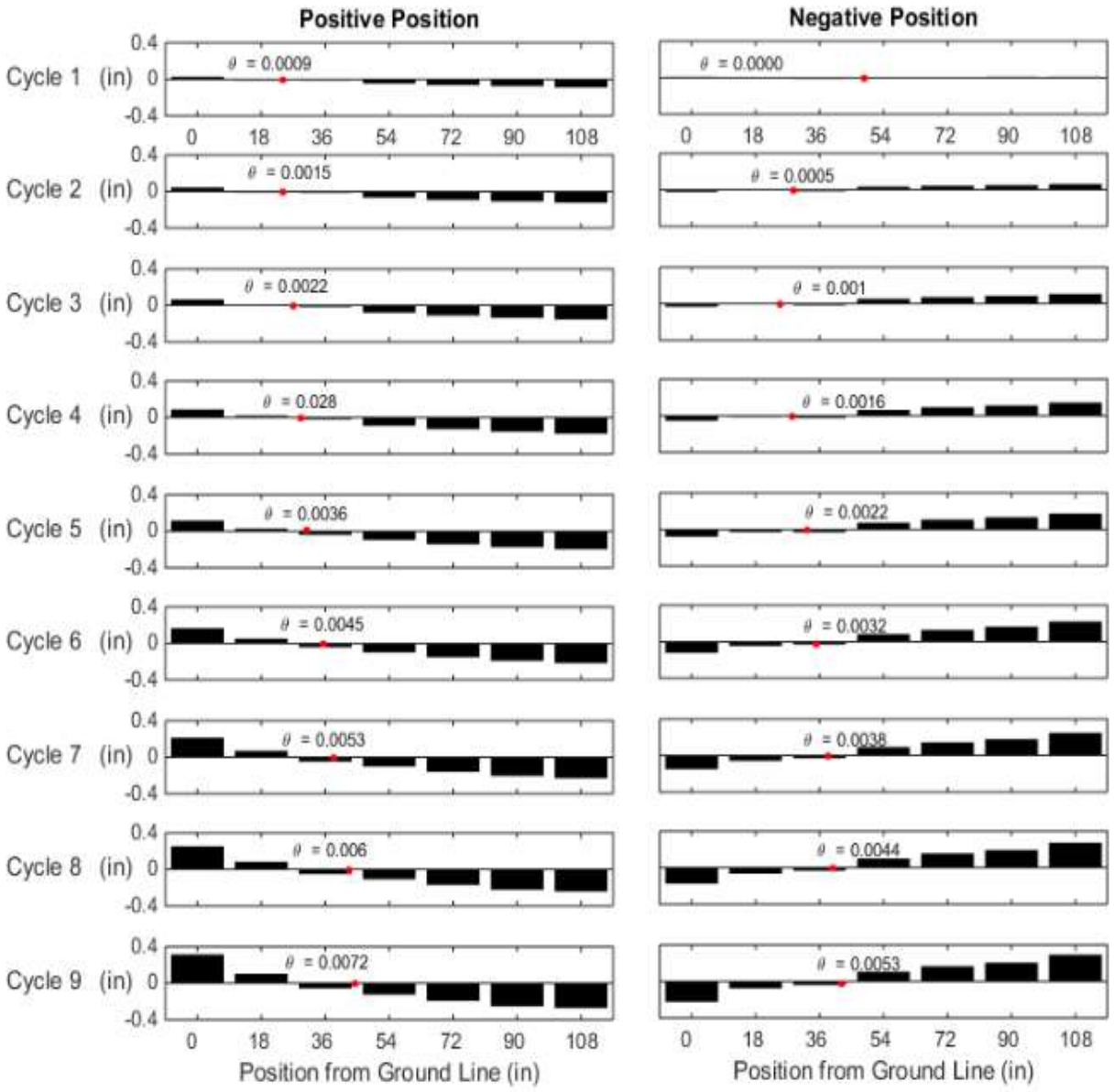

Fig. 4-7 Soil Displacement for each amplitude during the cyclic test on Pole 1.

4.1.1.2 Test 2 Results

Monotonic tests were performed to enable calibration of analytical models for comparative analysis. The overall load-deformation response of Pole 1 during the monotonic loading is shown Fig. *4-8*. The test was conducted with six load steps. The specimen was slightly unloaded after each step to observe cracks. Upon reaching the maximum load the resistance dropped drastically and only further displacement was attained. The experimental moment capacity reached was 72.3 kip-ft at the ground line. This is substantially low compared to expected results from comparative models discussed in later sections. The displacement resulting from rigid body motion within the foundation depicted a linear trend. The displacement from bending depicted an exponential trend.

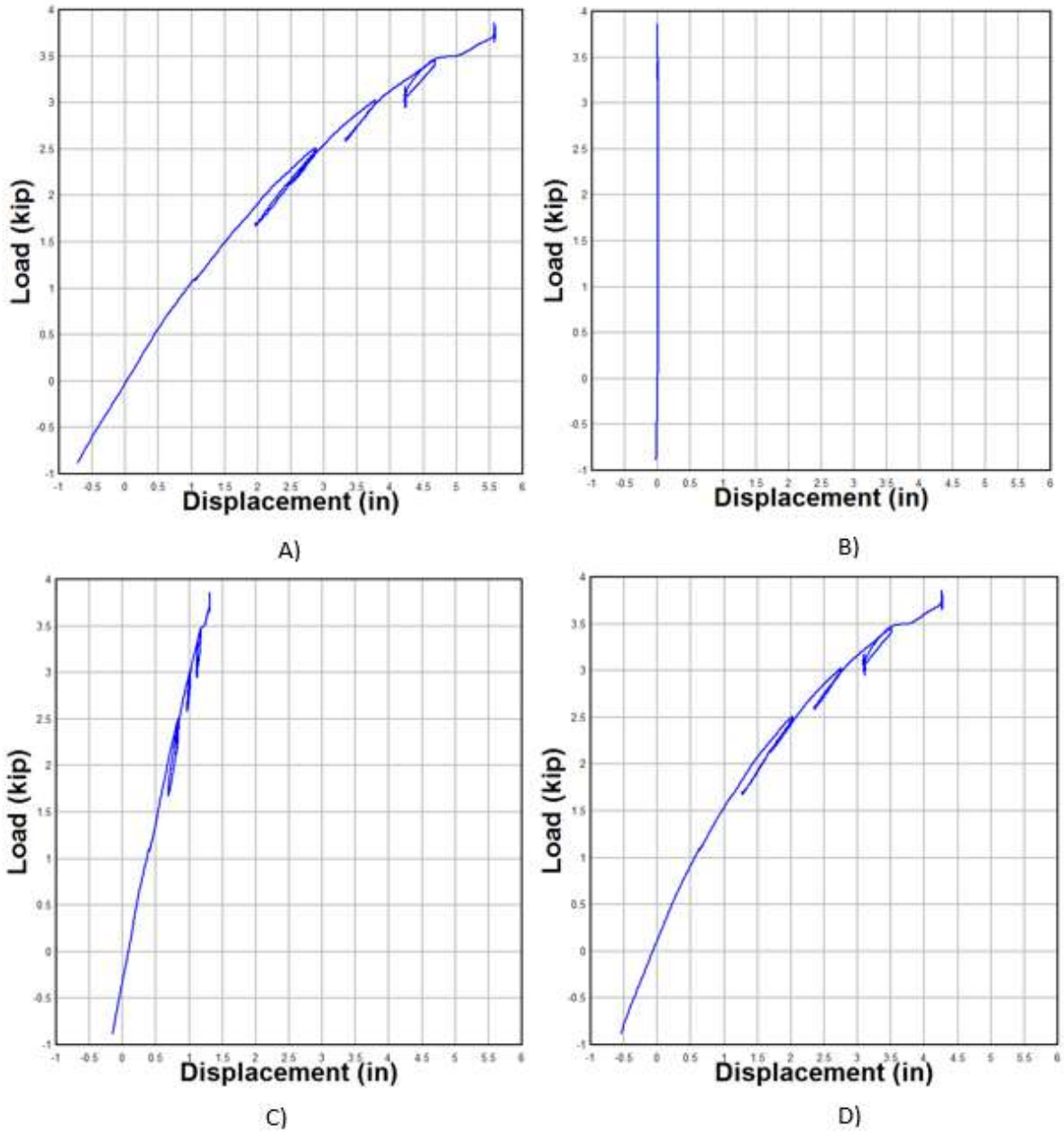

Fig. 4-8 A) Tip displacement, B) translational displacement of the steel plates, C) tip displacement due to rotation within the springs, and D) bending displacement at the tip for Pole 1 during monotonic testing.

4.1.2 Pole 2

4.1.2.1 Test 3 Results

The load-deformation response of Pole 2 is shown in Fig. *4-9*. As expected the strong axis response was stiffer and stronger than that observed for Pole 1. Pole two was able to achieve a capacity of 170 k-ft at the ground line and overall tip displacement of 10 in. before failure. Initially observed cracking of the cross section occurred close to 6 kips (positive displacement) and 3.5 kips (negative displacement).

The effect of rotation displacement is seen to be more prevalent in higher loads than other tests and seems to be linear with loading. The contribution from rotation within a strong axis tests was expected due to the larger moment of inertial of the pole cross section leading to reduced bending. The displacement achieved from bending of the pole is largely effected by cracking of the section which is seen in part D of Fig. *4-9*. A nonlinear elastic behavior is seen by the lack of a hysteresis effect during reverse cycles.

The beam failed again in the compression zone within the flange of the pole. Fig. *4-10* depicted the bottom flanges immediately after failure. The point at which the beam failed and began to reduce in load was deemed the ultimate capacity of the pole for the strong axis at the ground line.

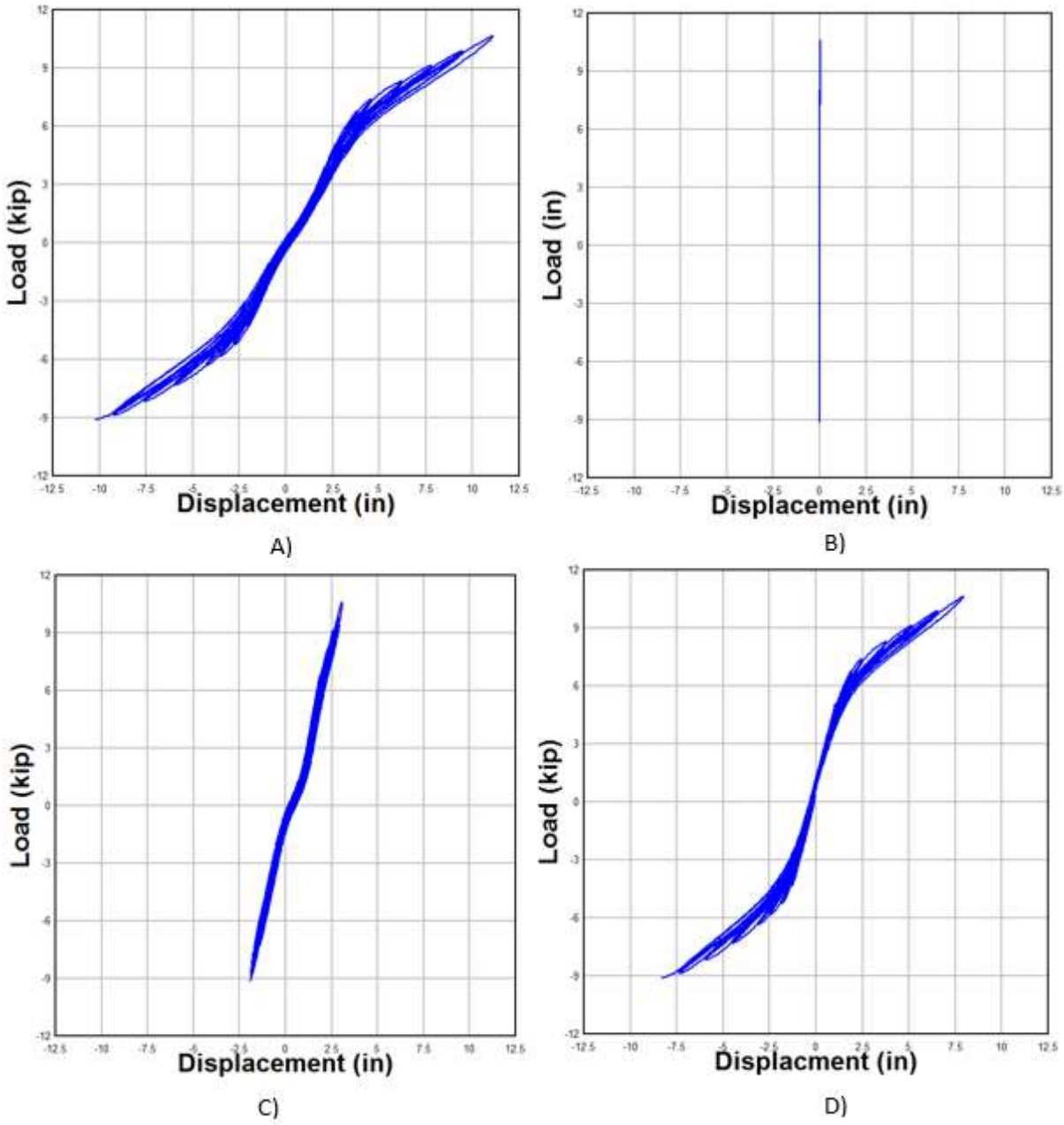

Fig. 4-9 A) Tip displacement, B) translational displacement of the steel plates, C) tip displacement due to rotation within the springs, and D) bending displacement at the tip for Pole 2 during cyclic testing.

Inspection of *Fig. 4-10* shows the outermost prestressing strand in the bottom flange is exposed and brooming. The image was captured during the peak negative displacement before the tip was brought back to neutral which allowed for capture of the strand to remain in a buckled state for examination.

Fig. 4-10 Pole 2 cyclic failure to bottom flange.

Fig. *4-11* presents the steel spring strain during increasing amplitude cycles for Pole 2. The spring stiffness is largest at the outer most locations with subsequent reduction depending on location. The ground line spring, labeled SS1 was saw the largest displacement among the embedment springs resulting in a high stiffness. The orientation of the foundation and possible differential tightening of the bolts that fasten the spring to the specimen could lead

to a stiffer spring. The change in sign of load throughout the spring strain is a good indicator that the center of rotation occurred between spring 3 and 4.

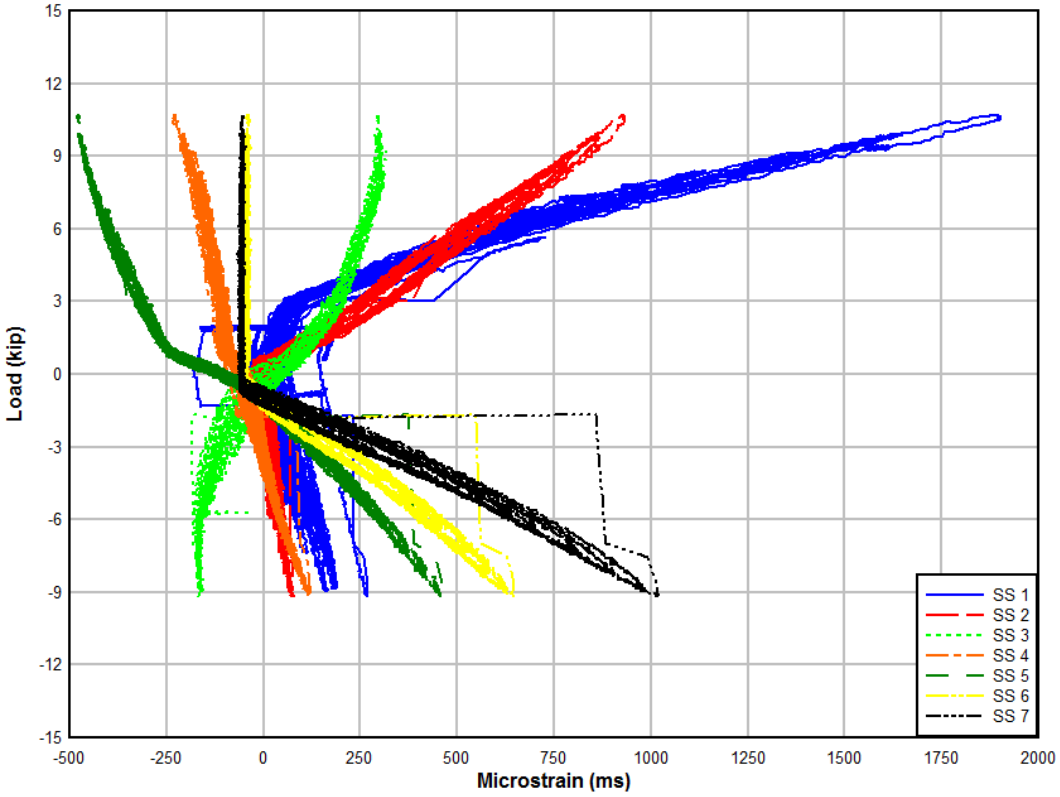

Fig. 4-11 Steel plate spring strain vs load for Pole 2.

The neutral axis of the ground line cross section of Pole 2 was relatively consistent. *Fig. 4-12* shows the trend of the neutral axis during positive and negative cycles. The neutral axis, during positive cycles (pulling up), allowed for a slightly deeper neutral axis. The debonded strand in the section was located on the bottom which would made the composite cross section have a lower neutral axis when bending up. The neutral axis was primarily focused at 3 in. of depth from the extreme fiber resulting in a location at the bottom of the flange.

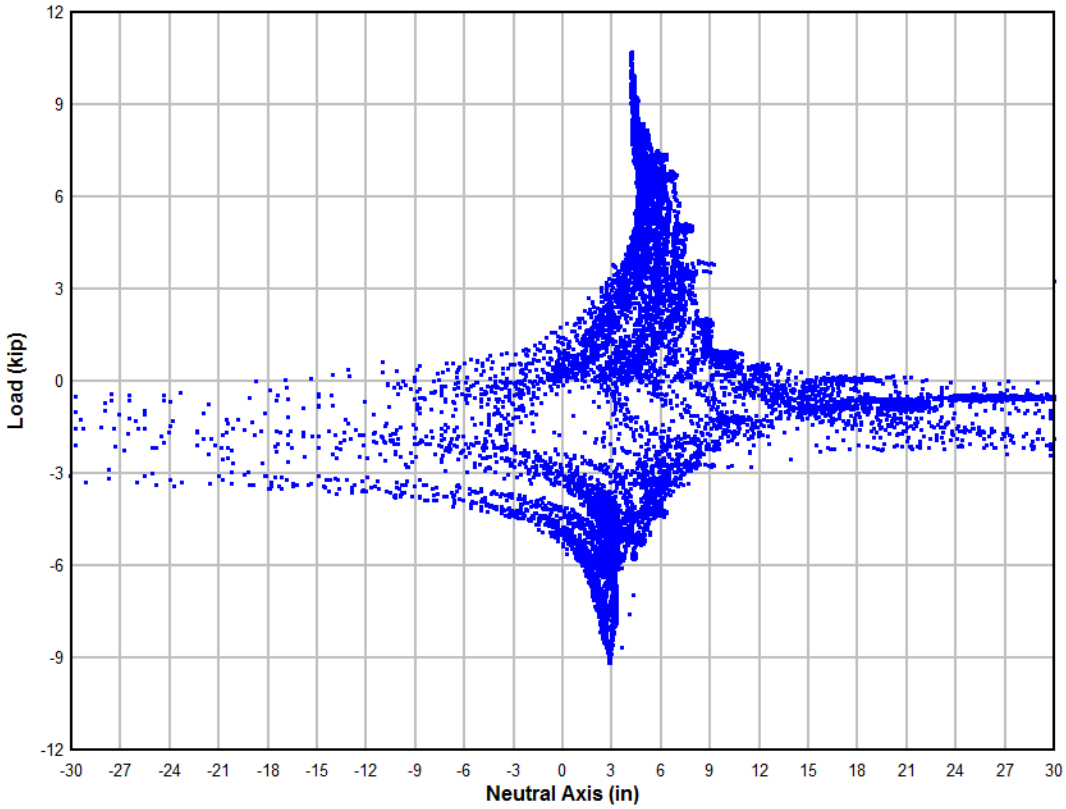

Fig. 4-12 Depth of neutral axis of Pole 2 during cyclic testing.

The curvature of Pole 2 above ground compared to below ground shows the effect of bending outside the simulated soil foundation. Fig. *4-13* allows a comparison of pole curvature between above and below ground line sections. The extent of the curvature for both sections are similar and nearly mirror one another. The nonlinear elastic nature of the pole can be seen in the curvature response above ground line section. The section monitored within the foundation shows the effect of friction within the system between springs, flanges, and bolts. The slight resistance results in load drop-off while the pole remains in the location.

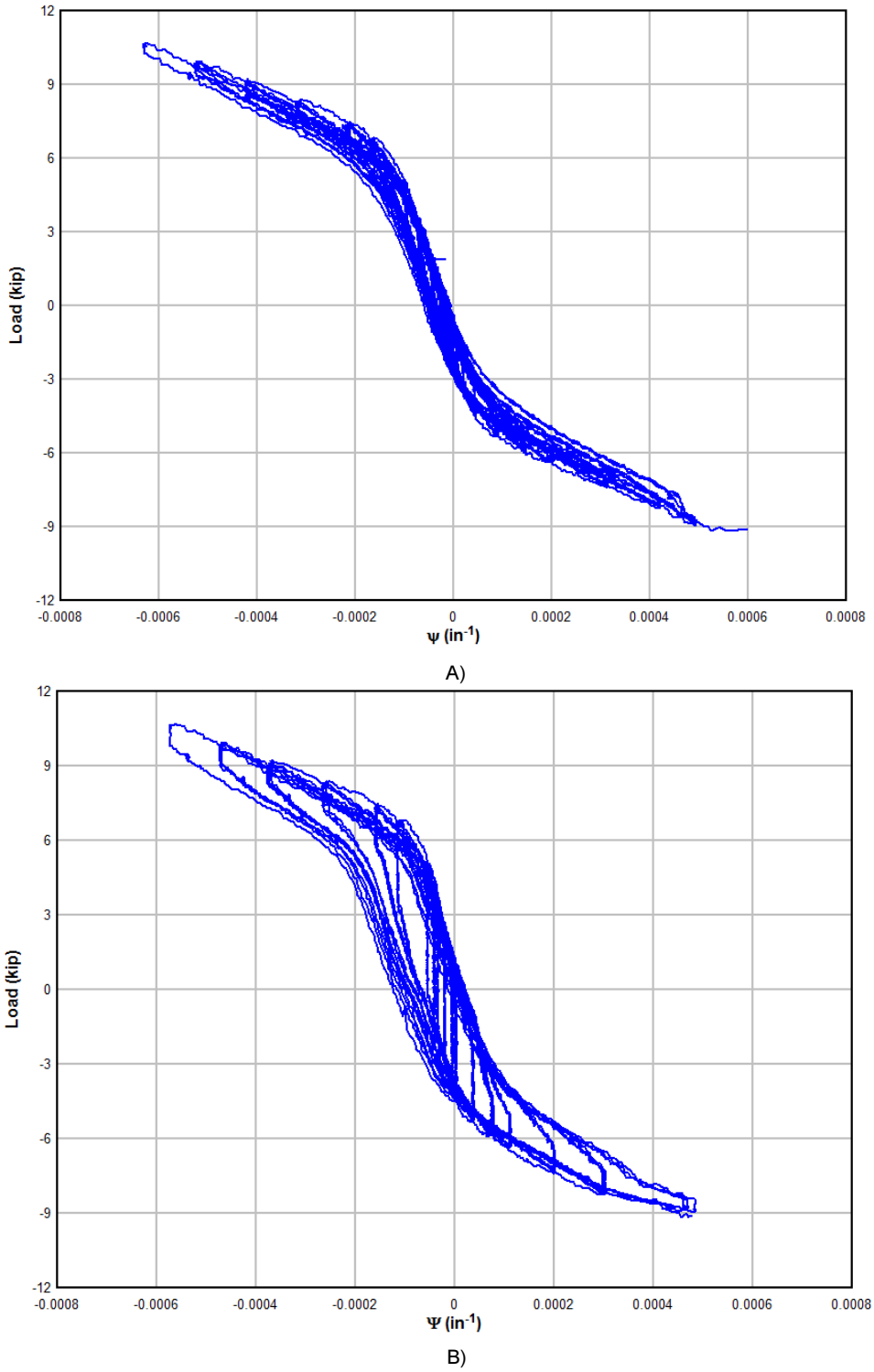

Fig. 4-13 A) Curvature of section above ground, B) curvature of section below ground from cyclic loading of Pole 2.

Fig. *4-14* shows the displacement of the diagonal sensors in the critical sections above and below the foundation ground line. The section above the ground line indicates that only vertical cracks were occurring since both displacement sensors recorded the same readings. The section below ground indicated larger displacement in the top diagonal displacement sensor. The large readings show a crack was forming parallel to the sensor during both positive and negative cycles until rupture. The vertical cracks occurring in the above ground line region indicate flexure was controlling while diagonal cracks in the below ground line region indicate shear was predominantly damaging the section.

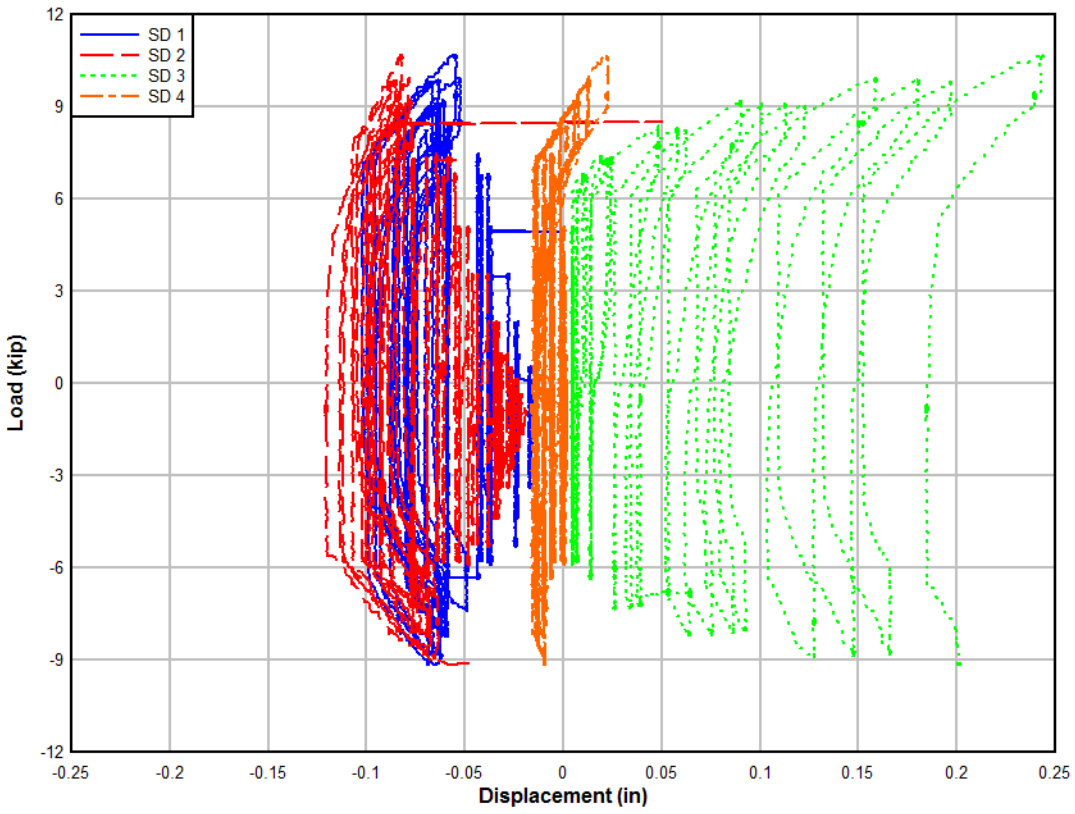

Fig. 4-14 Diagonal displacement of sections above and below the ground line for Pole 2.

4.1.2.1.1 Simulated Soil Response

The first two cycles in in *Fig. 4-15* have low displacements and depict the foundation seeming to settle onto the lower springs with an overall displacement of all springs being negative even while undergoing both positive and negative tip displacement. The soil springs began to engage in the third amplitude cycle and the magnitude of the angle of rotation was large enough to register significant displacements at the tip. The final cycle, when the pole reached capacity, the displacement for the groundline spring was nearly 0.5 in. which resulted in a large displacement due to rotation at the actuator. It can be observed that the location of the center of rotation within the postive postions gradually moves from the front half of the springs to the middle. The center of rotation of the negative postions seems to mirror the postive position and move from the middle to slightly closer to the ground line. The noticable movement of the center of rotation demonstrates the ability for the springs and pole to adapt to the loading and displace accordingly.

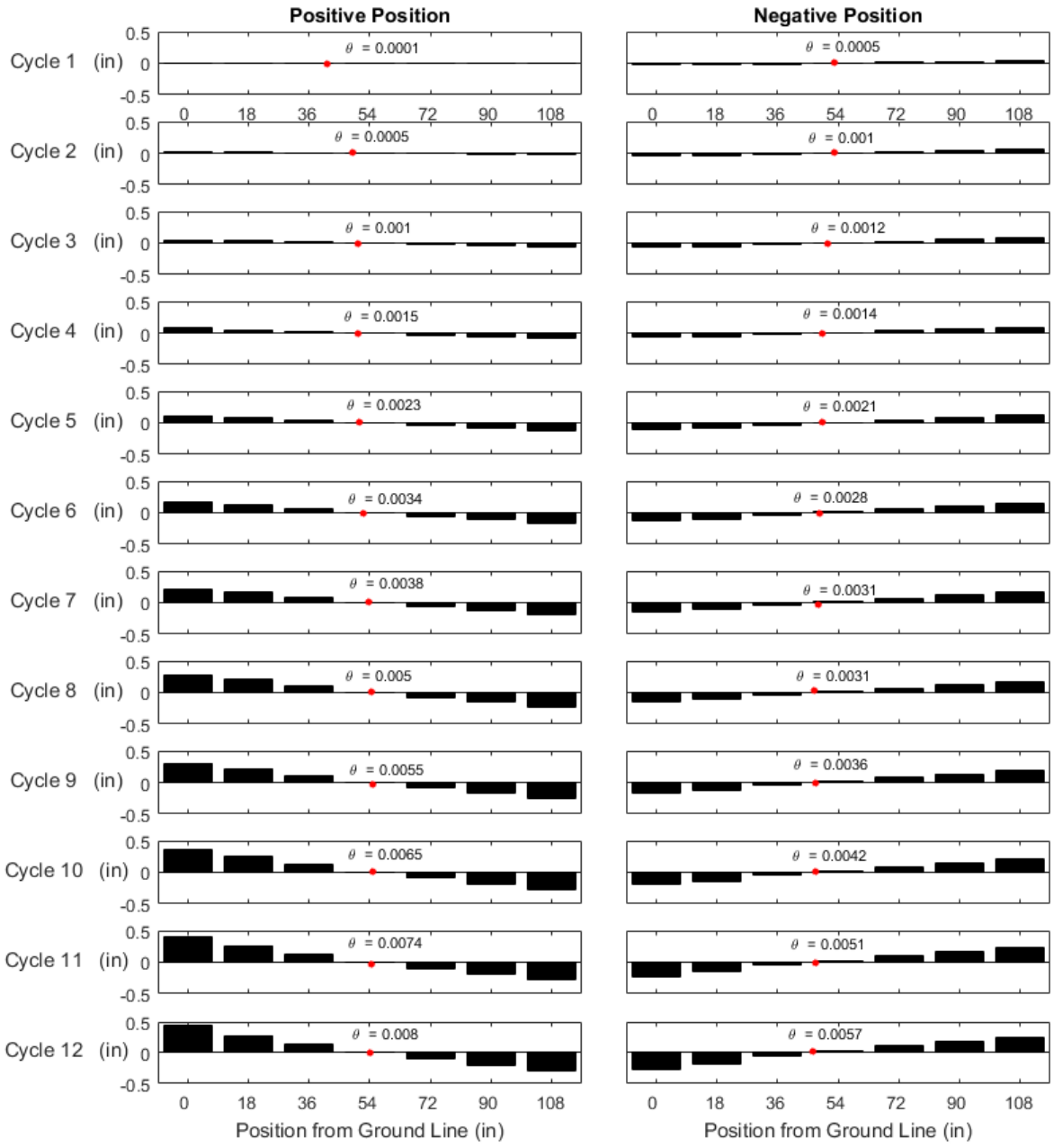

Fig. 4-15 Soil Displacement for each amplitude during the cyclic test on Pole 2.

4.1.2.2 Test 4 Results

Pole 2, oriented in strong axis, was displaced in much smaller increments until failure. The loadings and unloading for Pole 2 can be seen in Fig. *4-16*. According to the loading protocol and from results seen in cyclic testing of the same specimen, the first observed unloading did not take place until three inches of tip displacement. Then the loading and unloading was increased by 0.25 in. subsequently. At three inches, the slope begins to reduce in steepness indicating cracking occurred. The bilinear slope of the load-displacement plot for bending shows the point of a hinge forming. The final load and displacement of the pole was considered the capacity of the specimen which were 7.95 kips and 11.9 in respectively. The moment capacity from the ground line at failure was 146.7k-ft. The pole endured complete failure and lost all capacity without being returned to equilibrium for reinstallation of supports. The lower flange failure can be seen in Fig. *4-17*.

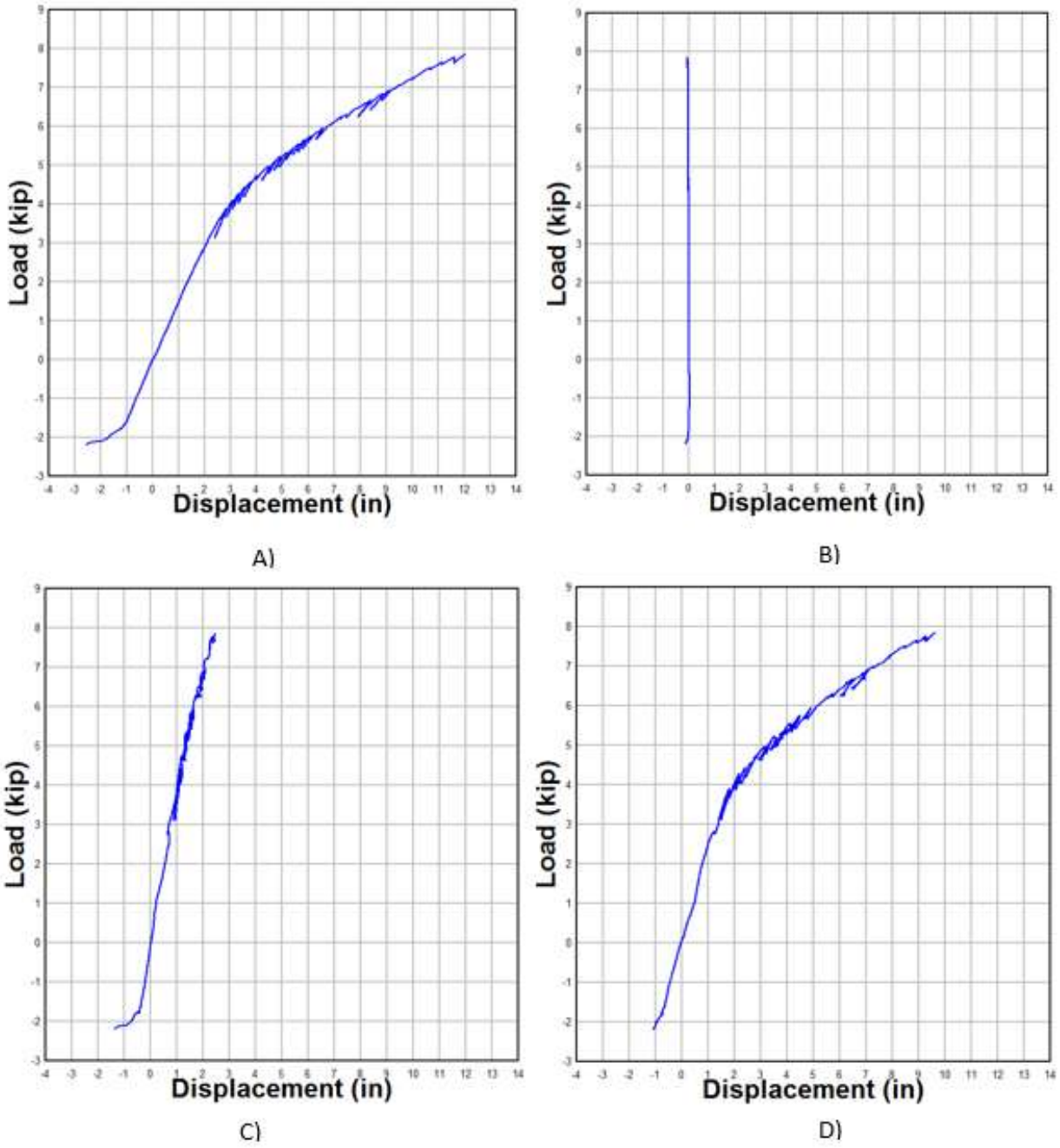

Fig. 4-16 A) Tip displacement, B) translational displacement of the steel plates, C) tip displacement due to rotation within the springs, and D) bending displacement at the tip for Pole 2 during monotonic testing.

Fig. 4-17 Flange failure for Pole 2 in monotonic loading.

4.1.3 Pole 3

4.1.3.1 Test 5 Results

Pole 3 failed at a moment capacity of 125.7 k-ft during a positive displacement position. The moment capacity was larger than Pole 1 but this was expected due to a larger cross section. The failure did not result in large fractures of concrete to break away from the pole requiring further cycles until large abrasions formed within the flanges. Fig. *4-18* demonstrates the load and displacement recorded at the actuator during increasing amplitude cycles with a breakdown of displacements from translation, rotation, and bending. Rotation played a smaller part in cyclic testing of Pole 3 as compared to Pole 2 which was assumed by the cross sectional properties. The first cycles to show signs of yielding were in the negative displacement region and gradual cycles lead to reduced capacity before a step increase to 9.25 in. in the positive displacement lead to failure. The first cycle at the 9.25 in. displacement lead to a significant reduction in load capacity in the positive direction. Each cycle after the ultimate capacity cycle lost load by a significant amount. The second cycle was nearly 1 kip less than the previous until the test was concluded. Cracking and slope change of the load-displacement plot shifted at around 2.5 kips before a nonlinear elastic type response began to form. After crushing of the concrete, the last few cycles showed plastic deformation and did not unload similarly to loading.

The prestressing strands in the specimen were not symmetrical and lead to the assumption that the pole would rotate with larger tip displacements but this was not the case. The beam rotated less than 5 degrees most likely due to the spacing of the prestressing strands being even to the cover on either side of the flange.

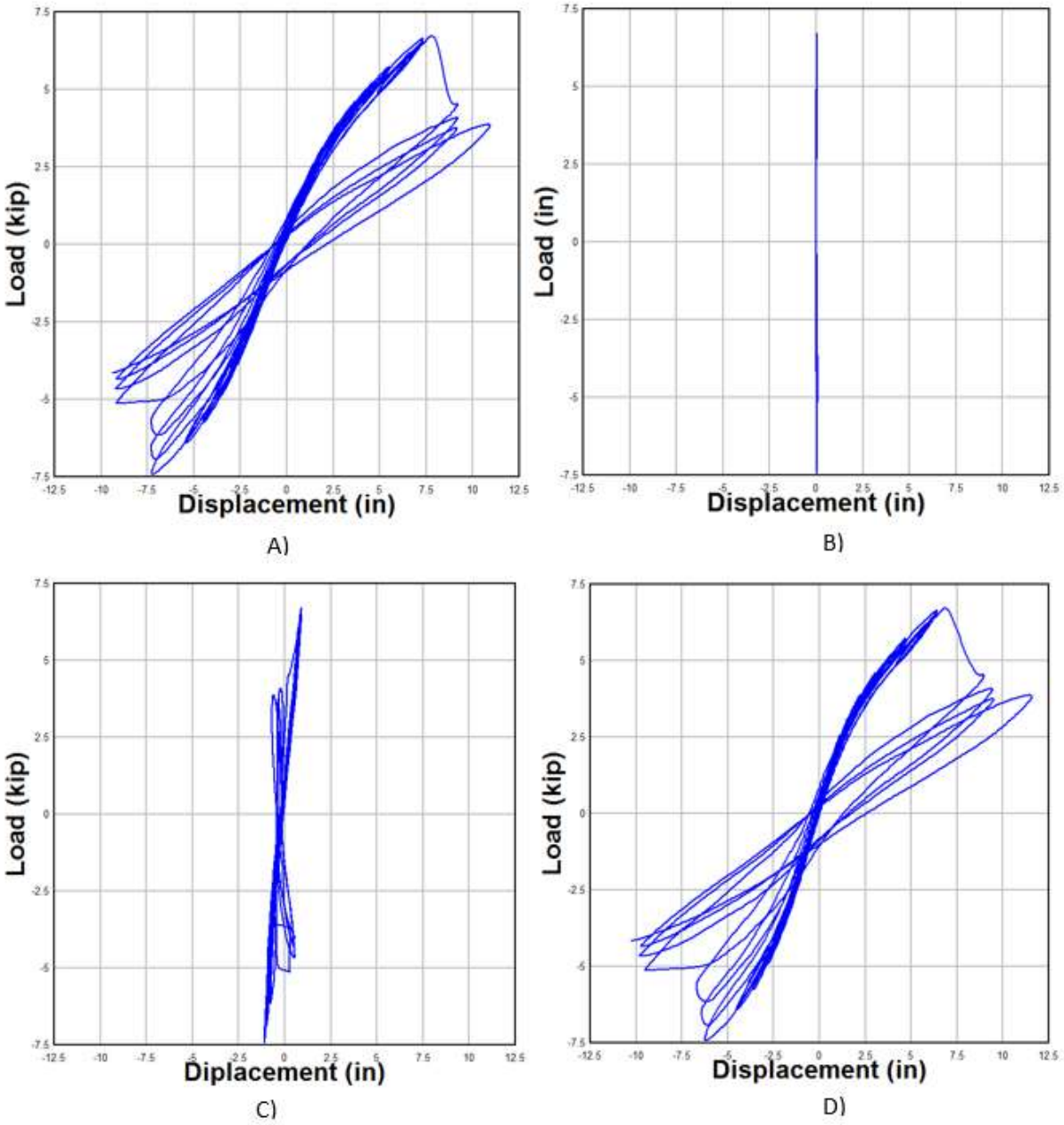

Fig. 4-18 A) Tip displacement, B) translational displacement of the steel plates, C) tip displacement due to rotation within the springs, and D) bending displacement at the tip for Pole 3 during cyclic testing.

The steel plate spring strain throughout the foundation are presented in Fig. *4-19*. The spring stiffness of the extreme springs had larger strains as expected from the testing apparatus. The strain of the interior strings was considerably less. The strain in the third spring labeled WS 3 had a particularly interesting strain loading that was not consistent with other springs. The majority of the springs depicted a linear increasing in strain during cycles but WS 3 plateaued at a microstrain of 50 ms. The center of rotation was located between spring 3 and spring 4 from interpretation of the strain induced at load. The soil spring rotation and location of the center of rotation will be presented later for each cycle.

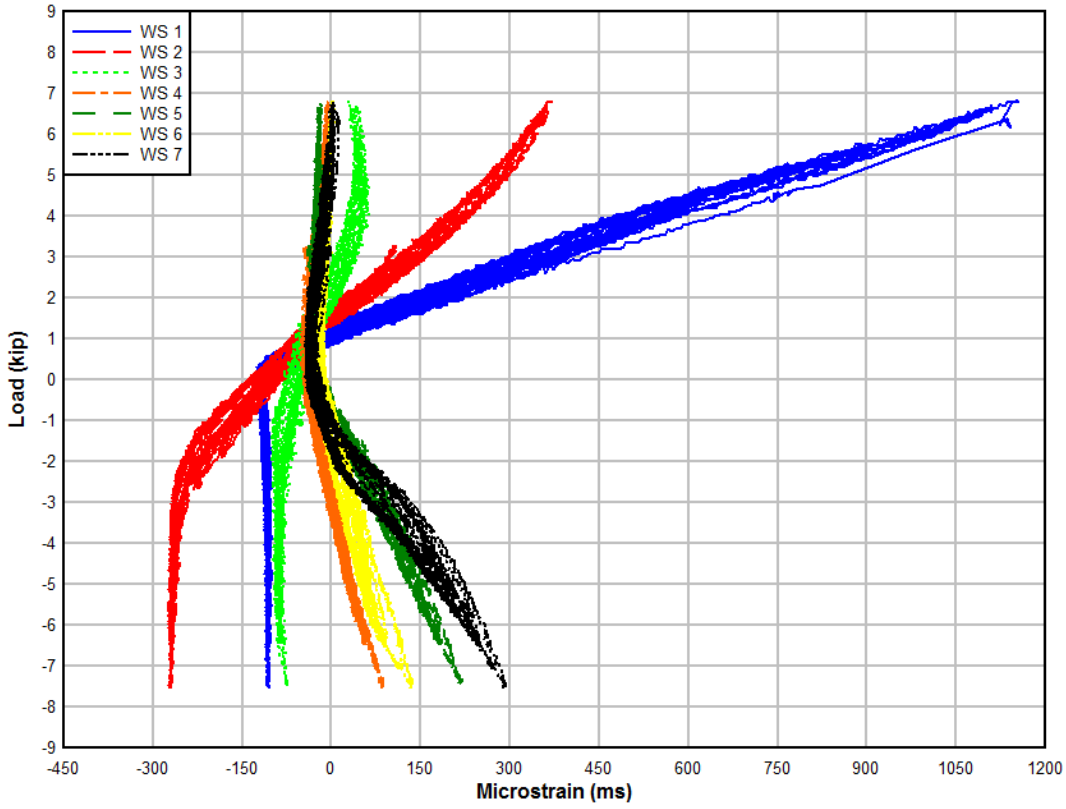

Fig. 4-19 Steel plate spring strain vs load for Pole 3.

The neutral axis of Pole 3 proved to be more difficult to identify in positive displacements as shown in *Fig. 4-20*. The discrepancy in the neutral axis depth at larger loads could be attributed to localized rotation of the specimen. The rotation would provide uneven bearing on the flanges and be unique to each cycle. The concrete pole was placed on the bottom springs and then top springs were fastened to fit, leading to a more consistent bearing for the bottom springs which is seen in the negative cycles and consistent trend of a neutral axis depth of 6 in. The neutral axis depth during positive cycles has a shift at higher load that aligns with 10 in. depth which seems misplaced on a cross section with a depth of 15.8 in at the ground line location. The base of the positive neutral axis trend looks to be consistent of the negative cycles at about 6 in.

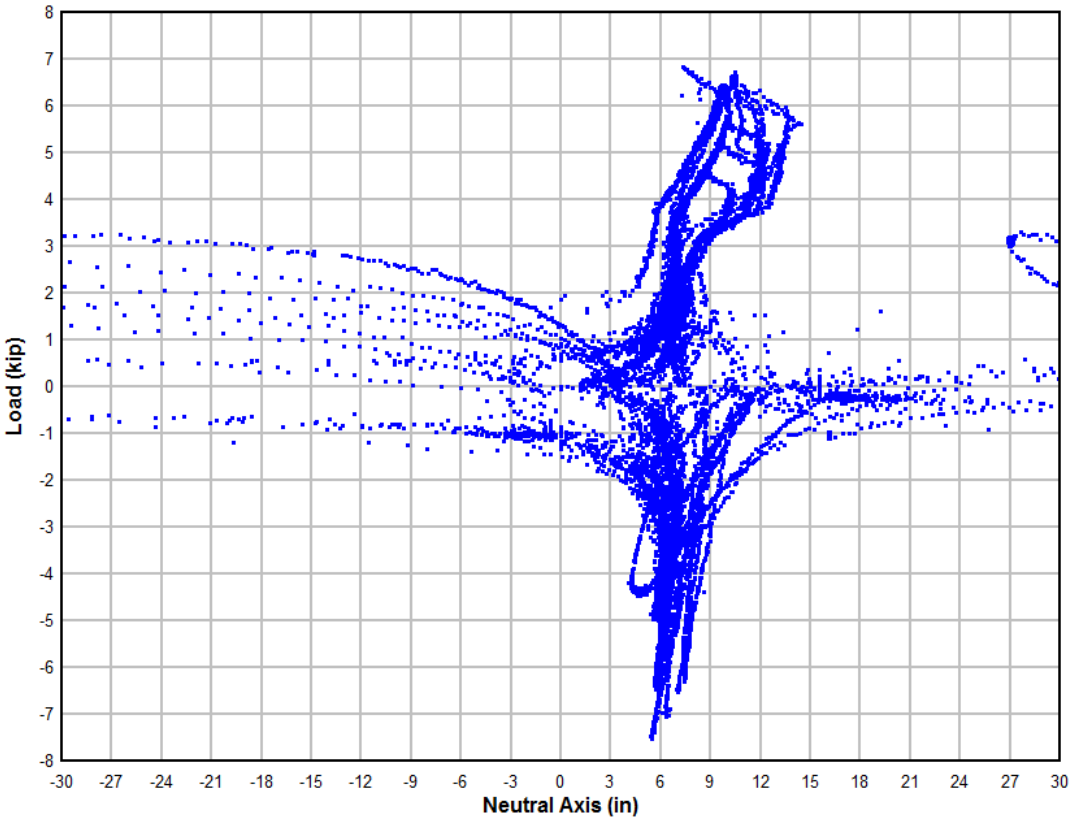

Fig. 4-20 Depth of neutral axis of Pole 3 during cyclic testing.

The curvature of Pole 3 above and below the foundation ground line are depicted in Fig. *4-21*. The linear elastic nature of the section above ground is particularly interesting as it was not observed in previous tests. The below ground section shown in B shows a discrepancy after cycles leading to loads larger than 3 kips. The linear nature was not expected as cracking at larger amplitude cycles would allow more curvature from the section. The negative cycles were consistent with expected trends and showed system friction as load reduction at constant curvature. The friction in the system would lead to connections of the springs retaining the pole at a given location while the actuator was displacing the tip showing a reduction in load and a constant curvature for an increment of time.

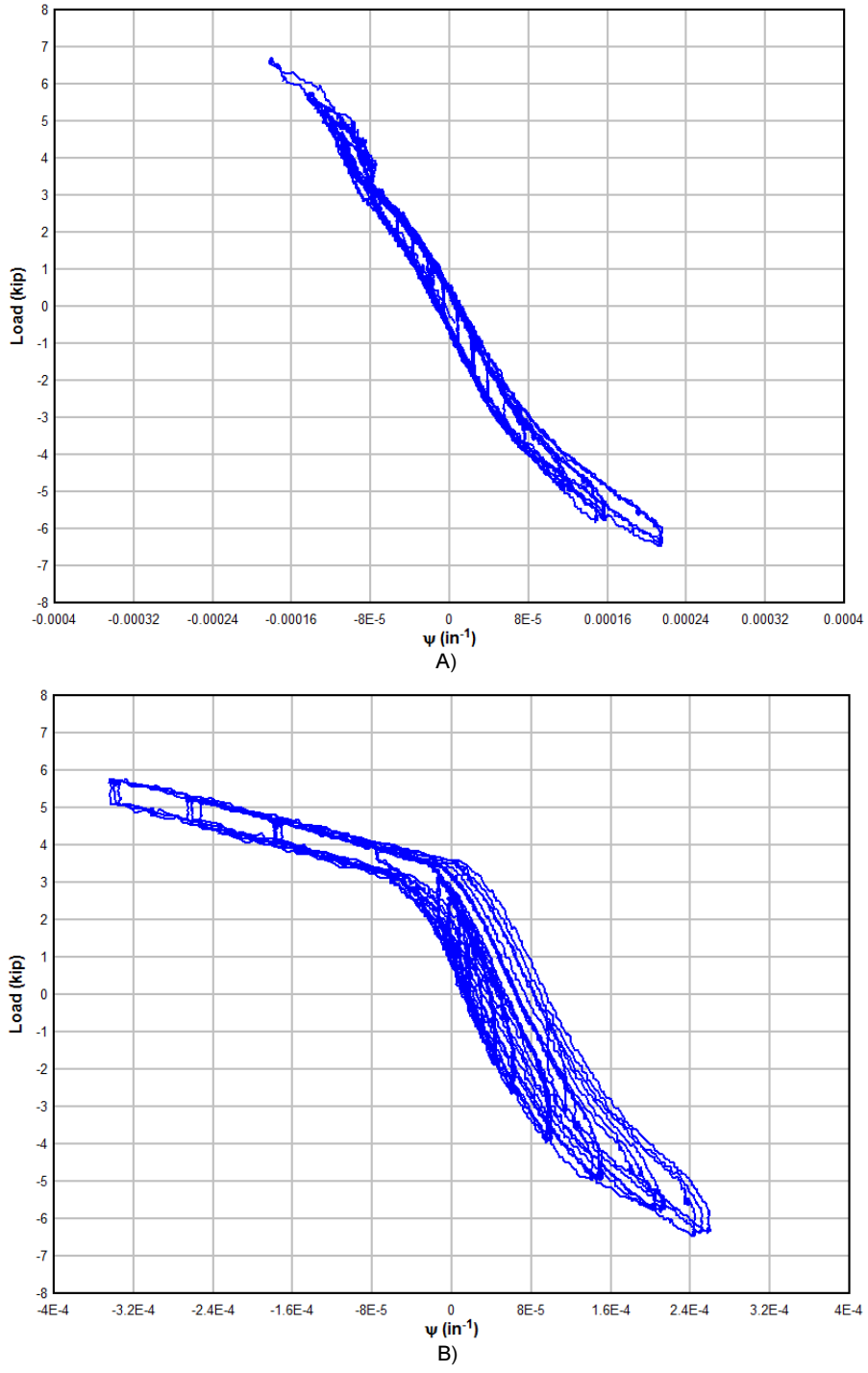

Fig. 4-21 A) Curvature of section above ground, B) curvature of section below ground from cyclic loading of Pole 3.

The diagonal displacement sensors for both above and below the ground line locations are shown in Fig. *4-22*. The similar displacement readings of WD 1 and WD 2 mean flexural cracking was occurring in the section. Flexural cracking will produce vertical cracks. Shear cracking are generally at a 45-degree angle to perpendicular and would resemble readings in a sensor such as WD 3. The lack of displacement for WD 4 means the shear crack was perpendicular to WD 3. All other previous tests resulted in shear cracks forming from the bottom ground line spring, test 5 shows shear cracking forming from the top ground line spring. The inconsistencies from all test data for positive displacement such as the curvature, neutral axis, and diagonals leads to the assumption that loading was not consistent and went unobserved during testing. The failure ultimate failure of the system was in a positive cycle and could have been premature for the cross section. A sufficient contact surface such as the bottom springs would have been the ideal failure location leading to more representative of the cross section capacity.

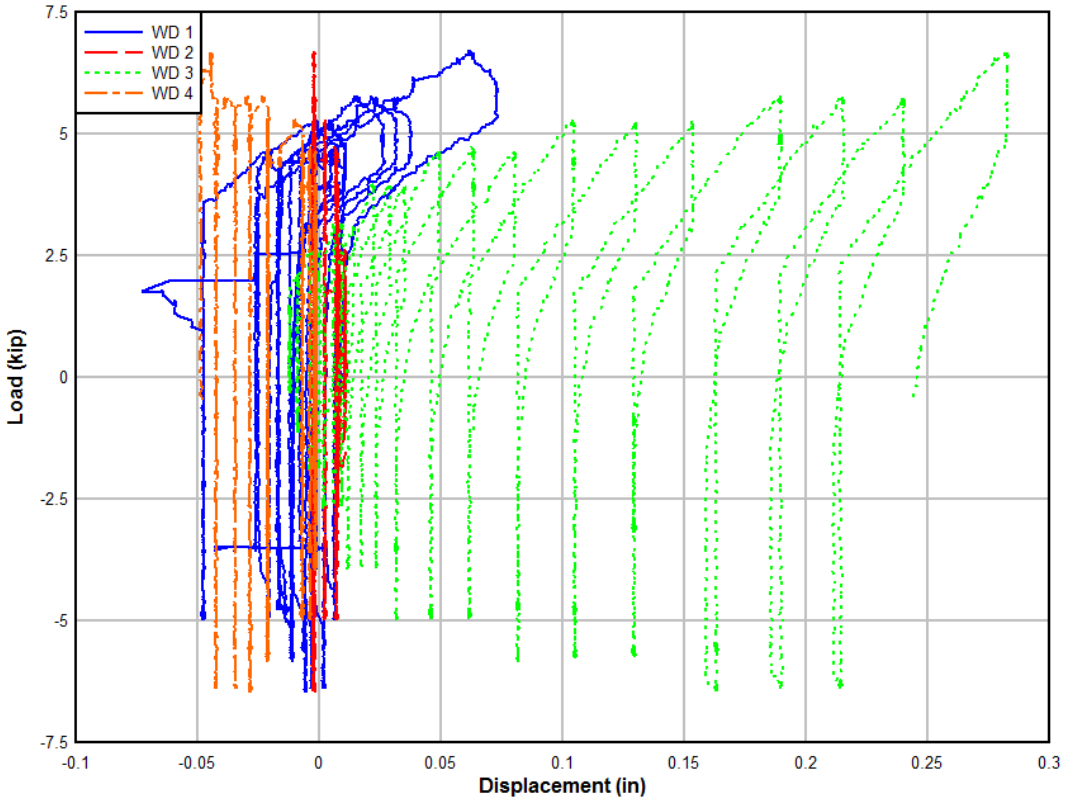

Fig. 4-22 Diagonal displacement of section above and below ground line for Pole 3.

4.1.3.1.1 Simulated Soil Response

Pole 3 allowed for the lowest maximum rotation within the cycles. *Fig. 4-23* illustrates the displacement, center of rotation, and rotation angle for each step in amplitude for displacement. The amplitude scale is the lowest of the three cyclic tests at a maximum amplitude of soil spring displacement of 0.25 inches. The center of rotation is noticably deeper within the embedment depth of the springs from the previous two tests. The average location of the center of rotation for the positive displacement of springs was 62.7 inches.

while the average location for the negative position was 46.7 inches. The difference of the center of rotations was the largest among the three tests and is attributed to the cross section asymmetry. The larger displacement in the springs near the ground line are in agreement with the stress distribution of a laterally loaded pile foundation. The negative position displacements on the later cycles tend to have larger displacements which could be an indication of cracking and less displacement in the groundline and nearby springs.

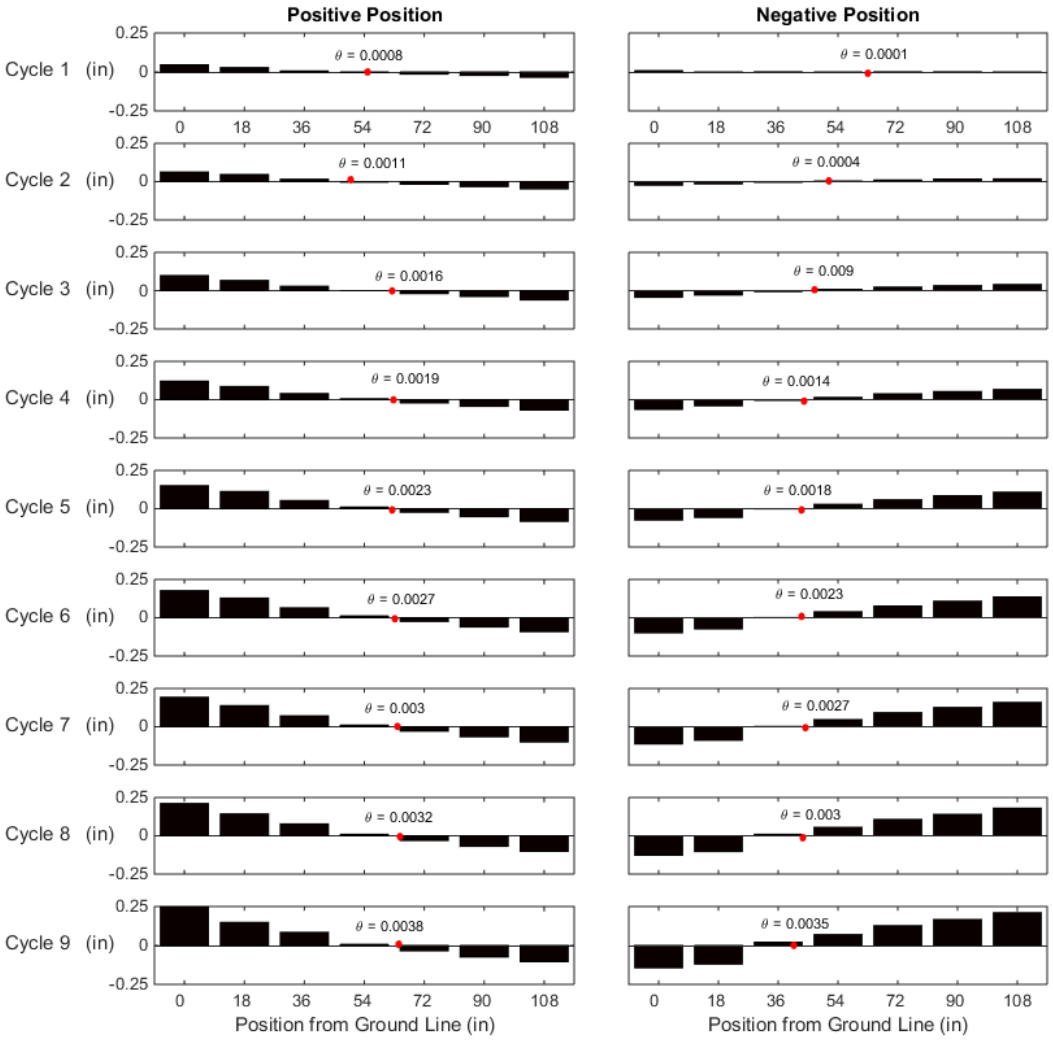

Fig. 4-23 Soil Displacement for each amplitude during the cyclic test on Pole 3.

4.2 Spring Results

4.2.1 Spring calculation

Spring displacement and strain was recorded during cyclic testing to see how springs would behave under loading. The strain in the springs was reduced to a point load to attain a spring constant for the springs at each displacement amplitude. The strain was measured at the extreme fiber and allowed for simple conversion to stress. The cross sections of both springs can be seen in Fig. *4-24*. The assumed configuration was calculated as a simply supported beam with mid-span displacement being monitored as illustrated in Fig. *4-25*.

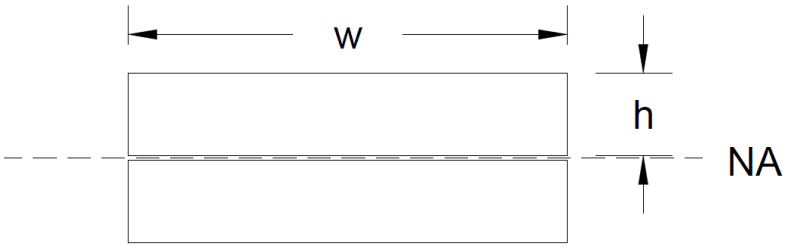

Fig. 4-24 Cross section of springs.

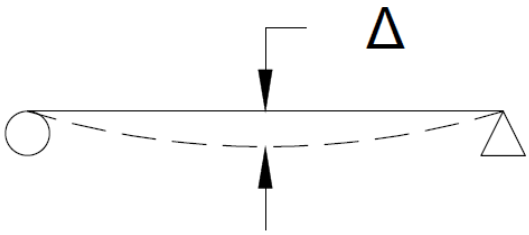

Fig. 4-25 Simply supported beam displacement.

The spring constants were calculated by using the slope of a load-displacement plot for each individual spring. The load sustained by each spring was extracted from the strain endured during loading. The first step to calculating the load was gaining stress from strain through equation [5].

$$\sigma = \epsilon * E \quad [5]$$

Where σ is stress, ε is strain, and E is modulus of elasticity of the steel springs. The next step was to reduce the stress into a moment at the mid-span. Using the extreme fiber stress and getting the internal moment by way of equation [6].

$$M = \frac{\sigma * I}{c} \quad [6]$$

Where M is the internal moment, I is the moment of inertia of the springs, and c is the distance from the neutral axis to the extreme fiber.

The moment is then able to reduce to a point load by the initial assumption that the springs are behaving like a simply support beam as previously illustrated in Fig. *4-25*. The resulting load can be derived from equation [7] which is the maximum moment at mid-span of a simply supported beam.

$$M = \frac{P*L}{4} \quad [7]$$

Where P is the point load at mid-span and L is the length of the beam or spring in these calculations. The values used for each variable are presented in

Table 4-2.

Table 4-2 Spring calculation constants.

Variable	
Distance to Centroid (in)	0.375
Width (in)	4
Height (in)	0.75
Length of Spring (in)	28
Moment of Inertia (in^4)	1.125
Elastic Modulus (ksi)	29000

The resulting load at each amplitude during cyclic tests was plotted against the displacement the spring underwent to produce a P-Δ curve for the springs. Only a few springs from each test displaced enough to give discernable results. The results from springs one and two were captured for all three cyclic tests and spring five was able to be used in testing of pole 2. The load and displacement of these three tests are presented in Fig. *4-26*. The linear spring constants of each spring was calculated by fitting a single polynomial line to the data and recorded in Table *4-3*. The springs all resembled a similar spring constant leading to an average to be taken resulting in about 23 kips/in. This value was larger than the initial assumption of two independent springs that acted in series of one

another but drastically less than theoretical values of one large spring in either fixed or simply supported end supports.

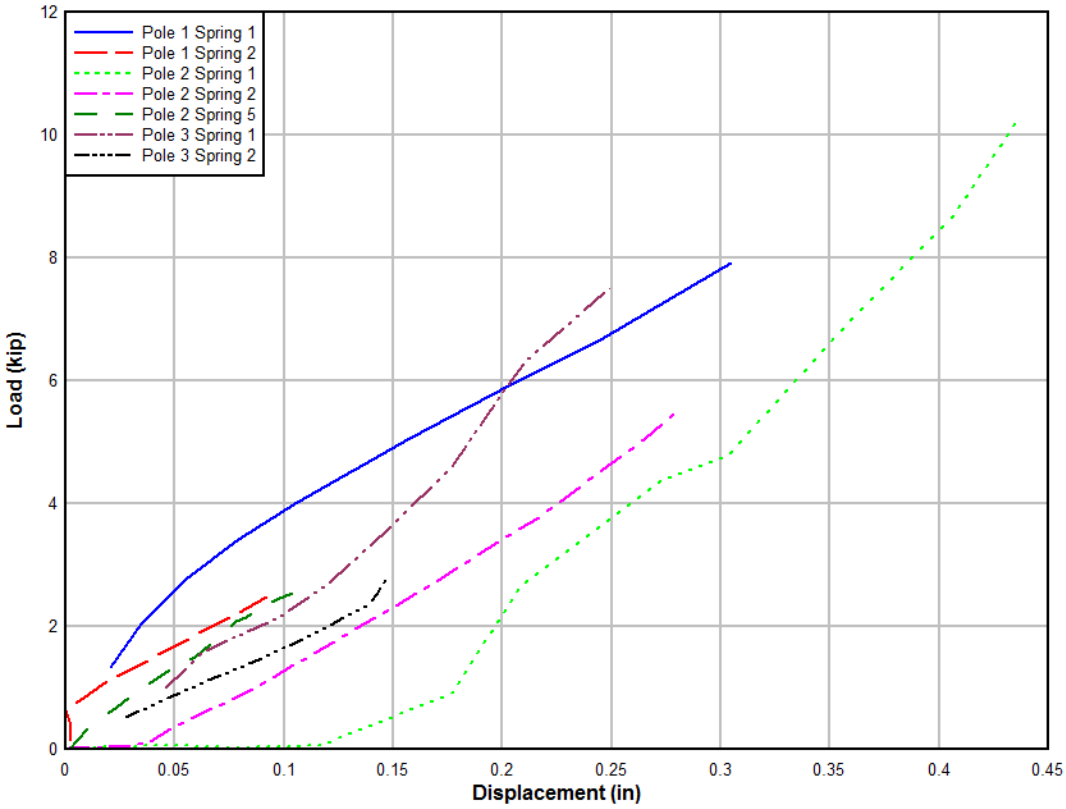

Fig. 4-26 Spring behavior under loading for cyclic tests.

Table 4-3 Foundation Spring Constants.

Location	Pole 1	Pole 2	Pole 3
Spring 1 (kip/in)	22.01	31.78	32.24
Spring 2 (kip/in)	19.67	21.93	17.8
Spring 5 (kip/in)	N/A	24.83	N/A
Average (kip/in)	20.84	23.38	25.02
Total Average (kip/in)	23.08		

The theoretical spring values of both fixed and simply supported end condition beams compared to initial assumptions of the spring system are compared to the experimental average calculated. Table *4-4* lists the spring constants while *Fig. 4-27* allows for a visual representation of the spring constants for comparison.

The friction of the two springs on one another allowed for a stiffer spring to emerge than previously thought but was less than half the spring constant expected from a single thicker spring. The experimental spring constant of 23 kip/in was an order of magnitude larger than what realistic soil values would produce. The ideal spring constant of 2.6 kip/in would be incredibly difficult to produce using a material with such a large modulus of elasticity such as steel.

Table 4-4 Spring Constants.

Scenerio	k (kip/in)
Theoretically Fixed	285.35
Theoretically Simply Supported	71.34
Preliminary Approximation	17.8
Experimental Average	23.08

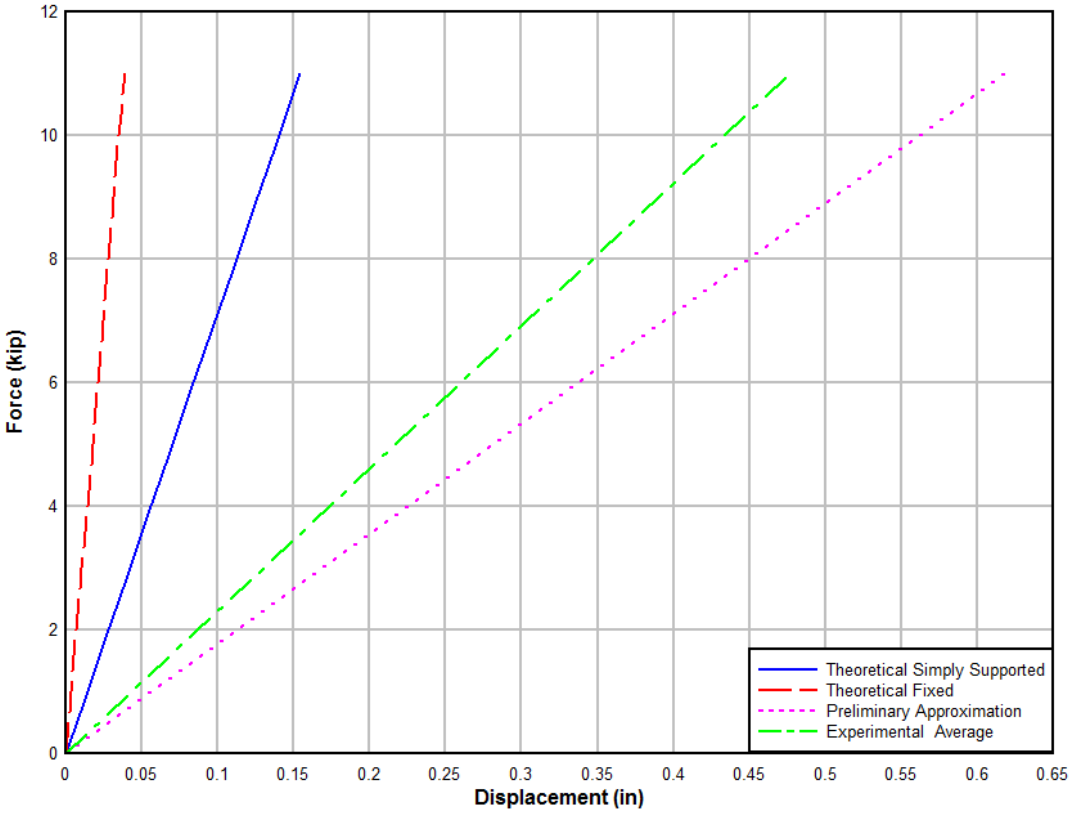

Fig. 4-27 Spring Constants.

5 Comparative Analysis

5.1 Models

Using the provided values from specimen details, models in both OpenSees and Response2000 were created for the structural responses of the poles. After material testing was completed, a more accurate representation of the poles weas input into models to increase the accuracy of the analytical depiction of the structure.

5.1.1 Response2000

Response2000 (R2K) (Bentz 2000) was used for initial design of the loading protocol to estimate the yield-moment for the different pole specimens using nominal and design values for the material properties. After completing the tests of the poles in the structural testing laboratory, the material properties and cross sectional dimensions were established. Response 2000 was again used to estimate the strength of the poles using these updated properties. The model was created using the measured cross sectional properties of the poles. The concrete compressive and prestressing strand and mild steel reinforcing tensile properties were used as the material inputs. Two different analysis cases were considered for each pole: 1) no prestressing losses and using the initial prestressing force shown in the construction drawings and 2) with prestressing losses calculated in section 3.2.2.3.1. The moment to shear ratio for the sectional analysis was taken as 18.5 ft to represent the actuator load location relative to the ground line. The R2K predicted moment capacities of the pole specimens at the ground line are presented in Table *5-1* with the experimentally measured capacities.

As seen in Table *5-1*, the R2K predicted moment strengths at the ground line corresponded closely to the experimentally observed values. The exception was for the monotonic test of Pole 1, which was overestimated by 28 k-ft. The discrepancy is attributed to the sensitivity of the weak axis specimen to non-uniform contact along the soil springs whereby 4 surfaces were required to get uniform contact. This non-uniform contact produces uneven loading of the section. In addition, the two separate compression flanges associated with weak axis loading are more susceptible to damage and lack of confinement than a single compression flange. All other model/experimental comparisons were nearly 1-to-1 as seen in Table *5-1*.

Table 5-1 Response2000 comparison to experimental data.

Test	Model (k-ft)	Experimental (k-ft)	M_{actual}/M_{model}
Pole 1 Cyclic	114.2	106.5	0.93
Pole 1 Monotoni	100.8	72.3	0.72
Pole 2 Cyclic	162.8	170.45	1.05
Pole 2 Monotoni	148.5	146.7	0.99
Pole 3 Cyclic	138.2	125.78	0.91

Fig. 5-1 and *Fig. 5-2* display the models created for the cross section of Pole 1 and 2 during cyclic tests. The program has difficulty creating the weak axis so a shape that joins the flanges was required to represent the weak axis. Because the model is rotating about the X axis, the horizontal spacing of the reinforcement is less sensitive than the provided cover in the flanges.

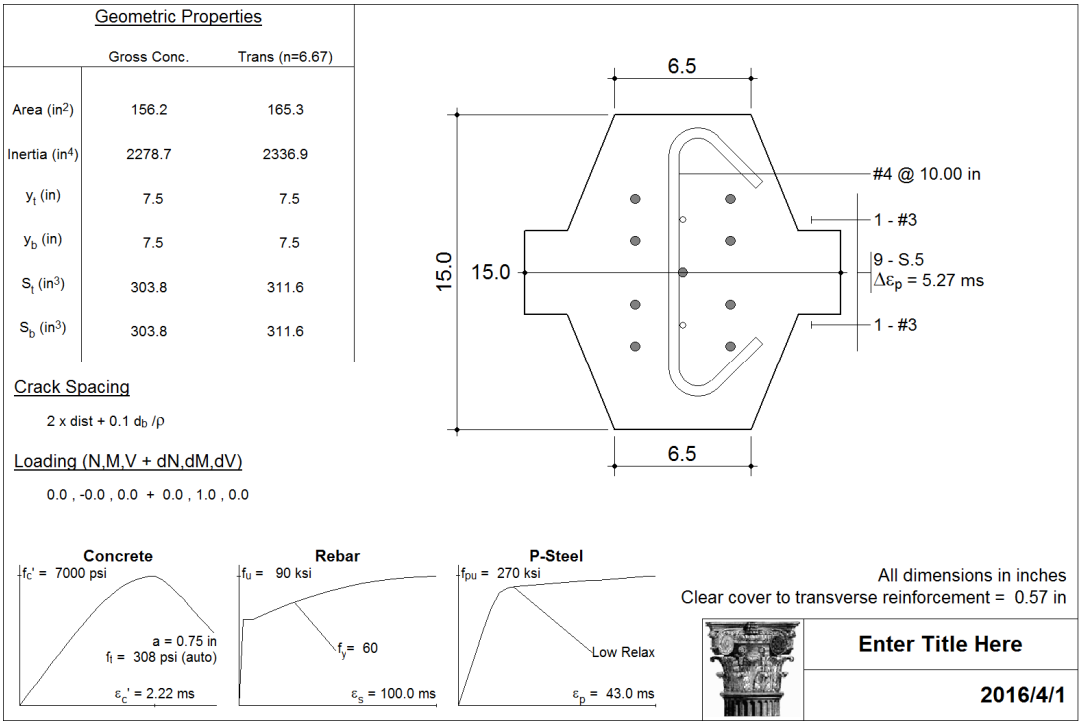

Fig. 5-1 R2K model for Pole 1 during cyclic testing.

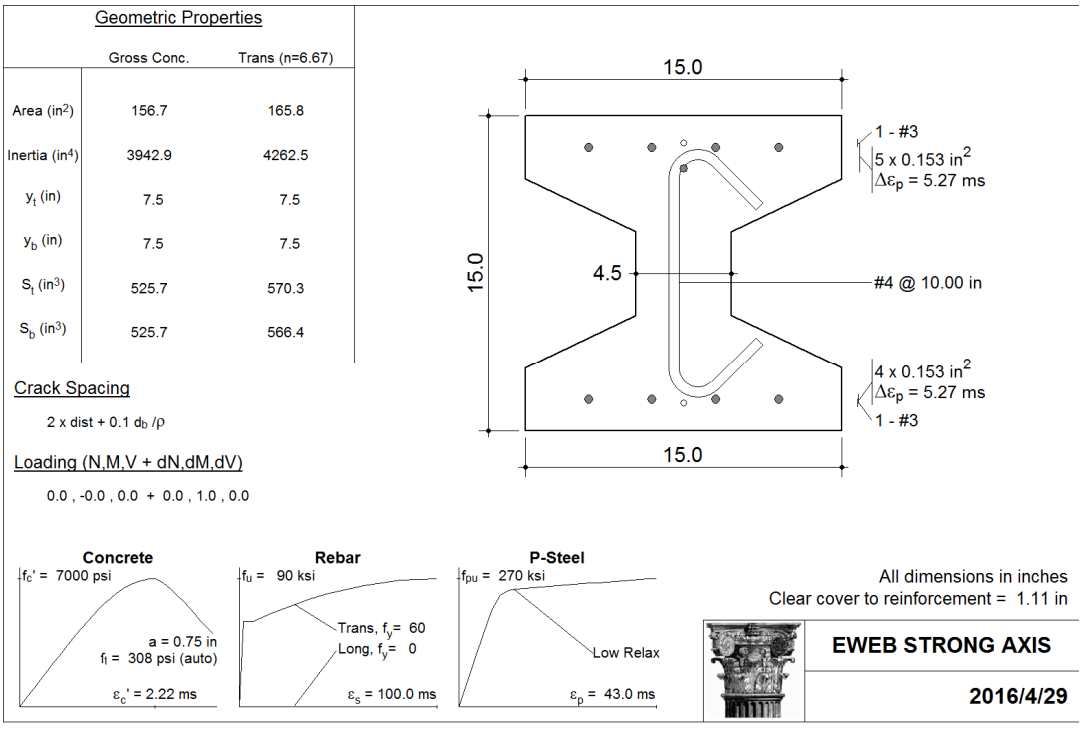

Fig. 5-2 R2K model for Pole 2 during cyclic testing.

5.1.2 OpenSees

A model of a concrete tapering pole with identical area and moment of inertia was created to represent the prestressed concrete poles provided by EWEB. The pole was broken up into 6 in. elements to distribute the tapering into 80 individual prisms. This also allowed for ease in placing springs throughout the embedments depth of the bottom 9.5 ft at 6 in. spacing. The bottom node was modeled as a roller to allow lateral displacement but endur the vertical load produced by the self weight of the pole. Zero length linear springs as described in the Winkler method (Dutta and Roy 2002; PEER 2005) represented soil in a simple manner. The model is visually simplified in *Fig. 5-3*. The poles were oriented upright with a a 10% self weight added at 3 ft. from the top to represent conductor loads.

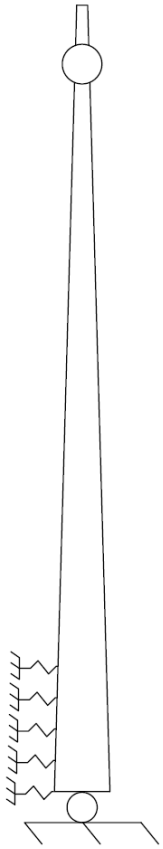

Fig. 5-3 OpenSees model simplification.

Within OpenSees, the ground nodes were excited by ground accelerations to simulate an earthquake response by the structure to known ground motions. The ground motions were chosen to be the 1940 El Centro earthquake, the 1989 Loma Prieta earthquake, and the 2011 Tahoku earthquake, provided by PEER (2016) and NRIESDR (2016), to follow previous experiments performed by Riley *et al.* 2003 becasue they were looking at earthquakes similar to conditions presented in the Pacific Northwest. The Tahoku ground motion was included in modeling due to the similarities of the expected subdution zone realease of a large magnitude earthquake (PNSN 2016).

The material for each element were created by distributing the pole cross section into regions. The regions became fibers of a uniaxial material with characteristics of the concrete used on the poles. The streel prestresseing tendons were fibers introduced into the existing concrete fibers. The tendons were modeled as a prestrained steel uniaxial material. The material used for the springs were chosen to be a elastic uniaxial material with a modulus of elasticity of varying values as the modulus of elasticity equates to the spring constant, k.

The model was created with the intent to show the effective moment demand on the tower by changing the soil stiffness variable and comparing the output to the observed moment capacity from experimental tests. The moment demand of the prestressed concrete pole when loading in the weak axis from the three earthquake ground motions previously mentioned can be seen in Fig. *5-4*. A baseline was input for the observed moment capacity during experimentation for comparison. All values presented are for groundline due to this being the critical element during modeling.

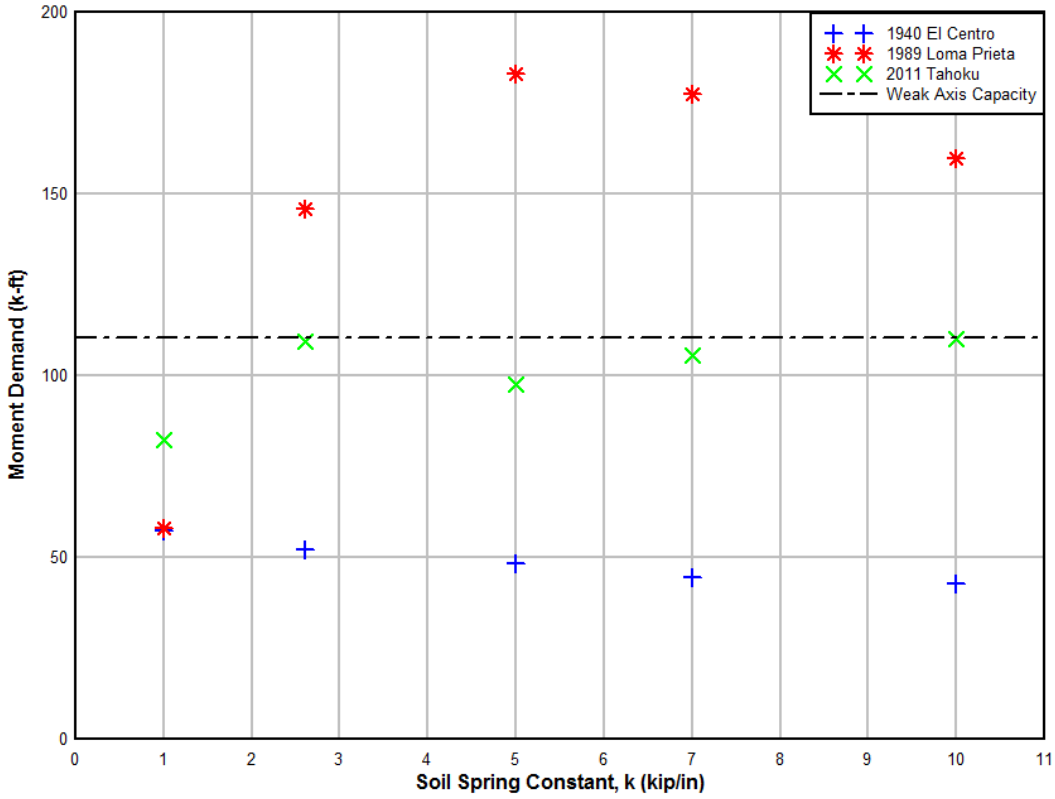

Fig. 5-4 Weak axis moment demand of 40 ft. OpenSees model with varying soil springs from multiple earthquake ground motions.

The weak axis oreintation for the 40 ft. pole sustained the earthquake motions in most cases. The ground motions for both the 1940 El Centro earthquake and the 2011 Tahoku earthquake did not cause structural failure of the pole at any of the presented soil stiffnesses. The noticable structural failures all take place durning the 1989 Loma Prieta earthquake. Out of the five simulations performed with Loma Prieta, only a soil stiffness of 1 kip-per-inch allowed the structure to remain undamaged. The remaining four simulations all demanded a significant amount over the available capacity of the pole and would result in structural failure.

The strong axis orientation of the 40 ft. pole did not fair as well as the weak axis simulations. The results of the simulation to the strong axis pole can be seen in Fig. *5-5*. The demand of all but three tests would cause failure of the pole. The simulations in which the pole would pass consisited of two 1940 El Centro simulations at soil constants of 1 and 5 kip/in and one simulation of 2011 Tahoku at a soil constant of 1 kip/in.

The results from the Loma Prieta earthquake in both orientations of the pole shows the importance of natural friequency of a structure. The El Centro earthquake was expected to be the least demanding for the structure and proved to be correct. The Tahoku earthquake was chosen to be a similar earthquake as expected of the Cascadia Subduction Zone but the large peak ground acceleration did not compensate for the overall low frequency of the earthquake. The structure was clearly most effected by the 1989 Loma Prieta earthquake and is likely due to the similarity in natural frequency for both the structure and the earthquake. A similarity in natural frequency can induce resonance and cause large displacements especially in the first mode which would lead to the largest demand at the critical section.

Soil failure is a large compenent of the simulation that would be beneficial to include in the model. The Wenchuan Earthquake in 2008 showed a rare occurance of tower failure during a seismic event and was attributed to soil failure (Eidinger 2009). If a boundary was included to impose system failure due to soil, the structural demand would be arbitrary for a given soil spring constant.

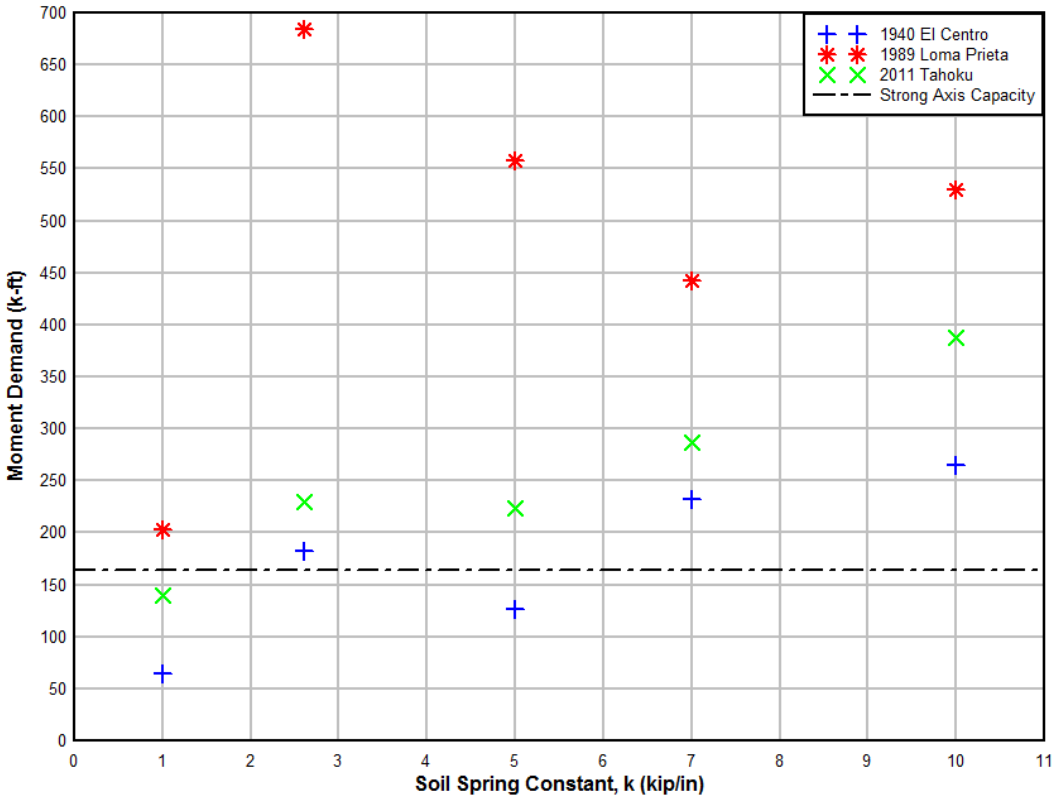

Fig. 5-5 Strong axis moment demand of 40 ft. OpenSees model with varying soil springs.

A response spectrum of the three earthquakes used in modeling was developed with a program labelled khist. The program produced the pseudo acceleration of the three time histories. The response spectrum with the three earthquakes with weak axis natural periods as well as the strong axis periods are shown in Fig. *5-6* and Fig. *5-7*. The Tohoku ground motion file was truncated to properly be analyzed in the program. The natural period of the structures for the weak axis were significantly longer than the natural periods in the strong axis orientation. The period of a structure is reflective of the stiffness which correlates to the longer period for an effectively less rigid structure in the weak axis. The model with Willamette soil spring stiffness of 2.6 kip/in. created a longer period and correlated to a

larger pseudo acceleration from the Loma Prieta earthquake. The lower period structure of the 10 kip/in. springs for soil in the weak axis resulted in a larger Loma Prieta acceleration as compared to the other earthquake response spectra. The strong axis natural period fell in a larger stored energy region of the response spectra. Loma Prieta was the controlling earthquake spectra for both natural periods for strong axis similarly to the weak axis tests.

The PGA of the Tohoku earthquake was roughly five times the size of the other earthquake ground motions and resulted in a khist output of a much larger pseudo acceleration. There is potentially a reduction factor that is required to reduce the extreme levels of acceleration at lower periods. The region of importance to the structures being observed is at a lower frequency resulting in a longer period and thus would not be affected.

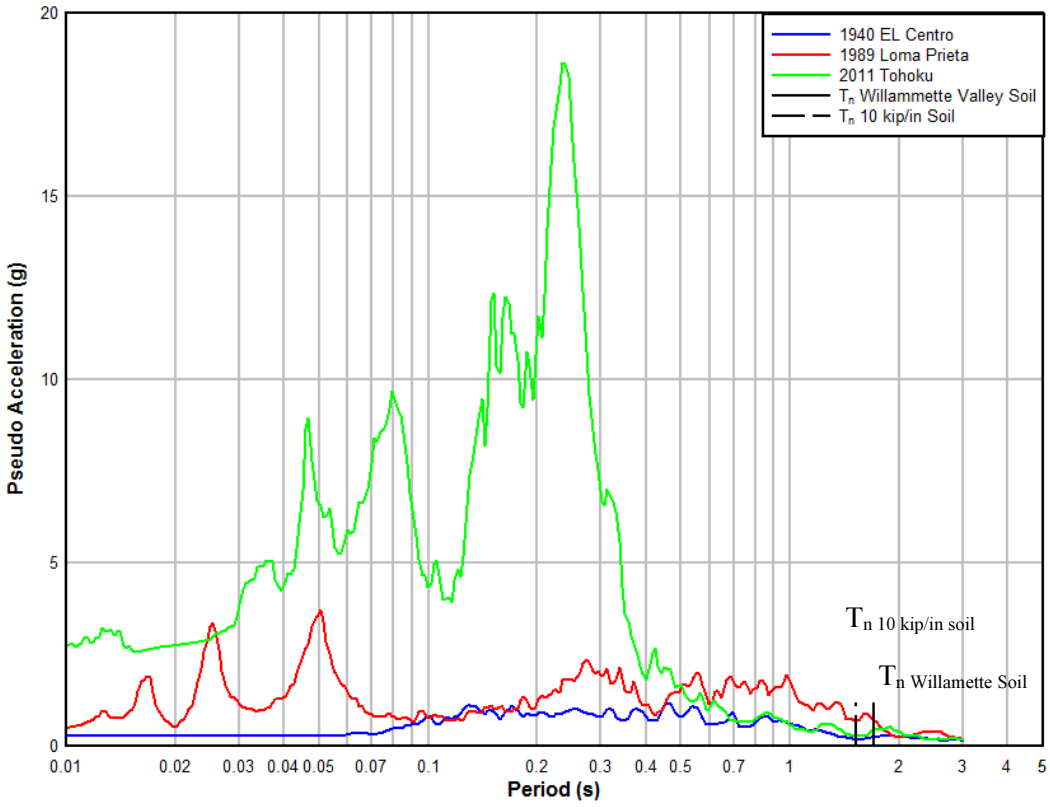

Fig. 5-6 Weak axis pseudo acceleration response spectrum.

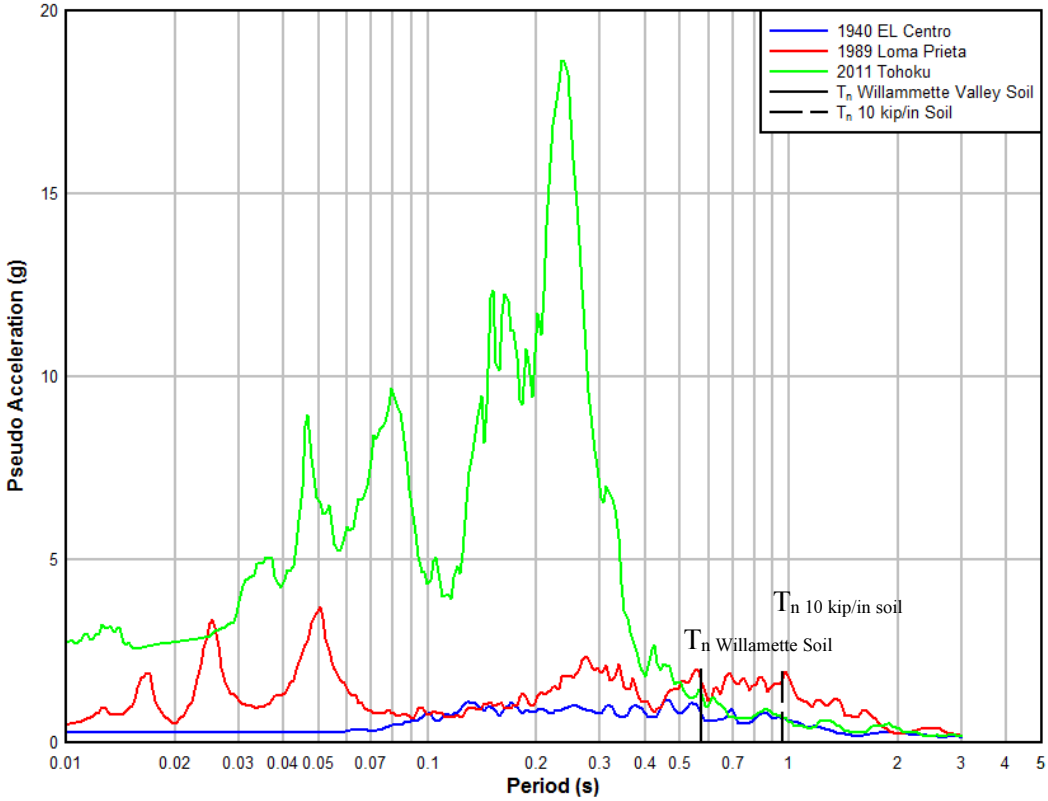

Fig. 5-7 Strong axis pseudo acceleration response spectrum.

6 Conclusion

In this research program, three prestressed concrete transmission poles were tested both cyclically and monotonically until failure. The specimens were extracted from service in the Willamette Valley and were ultimately tested to provide insight into resilience for seismic loading. The moment capacity of the poles at the theoretical ground line was compared to the actual experimentally tested moment capacity through the use of a program called Response2000. An innovative approach to creating a foundation similar to soil through the use of steel springs was tested in place of fully fixing the embedment end. Based on the presented experimental tests, the following conclusions have been prepared:

The concrete used within the poles was lightly degraded and did not significantly reduce the compressive strength. This leads to the assumption that weather has had little effect on the resilience of the poles.

The prestressing strands and mild steel used throughout the pole were not visually nor through instrumental measurements deemed corroded and performed as initially intended. Only standard prestressing losses need to be accounted for.

The moment capacities were accurately modeled with Response2000 and the program can confidently be used to predict other specimens of similar structure. The experimental capacities were validated by the model.

An OpenSees model of the poles can be used to see the internal moment demand from an earthquake response. The model allowed for comparisons of the weak and strong axis to ground motions showing which system is more likely to fail. An inclusion of soil parameters such as failure, would greatly improve the thoroughness of the model.

The soil spring foundation allowed for accurate moment demand of the beam while still allowing for realistic response from tip displacement through the rotation and translation of the beam within the foundation.

6.1 Additional Research

Based on results from the test and observed complications, the following areas of recommendations could be made:

6.1.1 Nonlinear springs

The springs in the foundation were made to be linear elastic but could be improved upon to produce bilinear spring constants or even more realistic nonlinear springs. The Winkler method for discrete linear springs was chosen to inspect the ability to produce semi-realistic results but could be expanded to include the modified Winkler method or even nonlinear springs.

6.1.2 Horizontal Loading

The authors of ASCE No. 123 discuss the testing of tubular transmission towers through the use of placing the structure horizontally similar to the experiment done here but an approach of then loading the structure horizontally as well would reduce the influence of gravity in the cyclic testing and possibly provide a more even response. Gravity was taken into consideration within the analysis presented but would provide one less variable for future researchers if considered.

6.1.3 Biaxial testing

Riley *et al.* 2003 expanded on their research to include biaxial loading of the towers in question. In the current research, only weak or strong axis was explored for the specimens and did not incorporate a possible 45-degree angle loading to each pole. The biaxial orientation of a specimen might be controlling and result in need for further analysis.

7 References

AASHTO Standard TP 95, 2014, "Standard Method of Test for Surface Resistivity Indication of Concrete's Ability to Resist Chloride Ion Penetration," American Association of State Highway and Transportation Officials, Washington, D.C., 2014

Andrade, C., M. Prieto, P. Tanner, F. Tavares, R. d'Andrea. (2013). "Testing and modelling chloride penetration into concrete." Construction and Building Materials 39: 9-18.

ASTM Standard C1723, 2010, "Examination of Hardened Concrete Using Scanning Electron Microscopy," ASTM International, West Conshohocken, PA, 2010

ASTM Standard C39, 2016, "Compressive Strength of Cylindrical Concrete Specimens," ASTM International, West Conshohocken, PA, 1921

ASTM Standard C42, 2013, "Obtaining and Testing Drilled Cores and Sawed Beams of Concrete," ASTM International, West Conshohocken, PA, 1921

ASTM Standard C856, 2014, "Petrographic Examination of Hardened Concrete," ASTM International, West Conshohocken, PA

ASTM Standard C876, 2015, "Standard Test Method for Corrosion Potentials of Uncoated Reinforcing Steel in Concrete," ASTM International, West Conshohocken, PA, 2015

ASTM Standard C856, "Standard Practice for petrographic examination of hardened Concrete," ASTM International, West Conshohocken, PA, 2015

ASTM Standard E8, 2015, “Tension Testing of Metallic Materials,” ASTM International, West Conshohocken, PA, 1924

Bai, F.-L., Hao, H., Bi, K.-M., and Li, H.-N. (2011). “Seismic Response Analysis of Transmission Tower-Line System on a Heterogeneous Site to Multi-Component Spatial Ground Motions.” *Advances in Structural Engineering*, 14(3), 457–474.

Bentz, E. C. (2000). Response-2000: Reinforced Concrete Sectional Analysis using Modified Compression Field Theory (Version 1.05) [Computer Software]. University of Toronto.

Billington, D. (2004). “Historical Perspective on Prestressed Concrete.” *PCI Journal*, (January- February), 14–30.

Bungey, J. H., and Soutsos, M. N. (2001). “Reliability of partially-destructive tests to assess the strength of concrete on site.” *Construction and Building Materials*, (15), 81–92.

Cascadia Region Earthquake Workgroup. (2013). *Cascadia Subduction Zone Earthquake: A magnitude 9.0 Earthquake Scenario*. Oregon Department of Geology and Mineral Industries.

“Cascadia Subduction Zone.” (2016). *Pacific Northwest Seismic Network*, <https://www.pnsn.org/outreach/earthquakesources/csz>.

Choi, W.-C., Picornell, M., and Hamoush, S. (2016). “Performance of 90-year-old concrete in a historical structure.” *Construction and Building Materials*, 105, 595–602.

Dejke, V. (2001). “Durability and service life prediction of GFRP for concrete reinforcement.” *Chalmers University of Technology*.

Dinges, T. (2009). “The History of Prestressed Concrete: 1888 to 1963.” Kansas State University, Manhattan, Kansas.

Dutta, S. C., and Roy, R. (2002). “A critical review on the idealization and modeling for interaction among soil-foundation-structure system.” *Computers and Structures*, (80), 1579–1594.

Eidinger, J. (2009). “Wenchuan Earthquake Impact to Power Systems.” American Society of Civil Engineers.

Garzon, A.J., et al., Modification of four point method to measure the concrete electrical resistivity in presence of reinforcing bars. Cement and Concrete Composites, 2014. 53: p. 249-257.

Goldfinger, C., Nelson, C. H., Morey, A. E., Johnson, J. E., Patton, J. R., Karabanov, E., Gutierrez-Pastor, J., Eriksson, A. T., Garcia, E., Dunhill, G., Enkin, R. J., Dallimore, A., and Vallier, T. (2012). “Turbidite Event History- Methods and Implications for Holocene Paleoseismicity of the Cascadia Subduction Zone.” *U.S. Geological Survey Professional Paper 1661-F*, 170.

Gowers, K. R., S. G. Millard. (1999). "Measurement of concrete resistivity for assessment of corrosion severity of steel using Wenner technique." ACI Materials Journal 96(5): 536-541.

Guidelines for Electrical Transmission Line Structural Loading. (2010). ASCE Manuals and Reports on Engineering Practice, American Society of Civil Engineers, Reston Virginia.

Guo, A., Yuan, W., Lan, C., Guan, X., and Li, H. (2015). “Time-dependent seismic demand and fragility of deteriorating bridges for their residual service life.” *Bull Earthquake Engineering*, 13, 2389–2409.

Harden, C., Hutchinson, T., Martin, G. R., and Kutter, B. L. (2005). *Numerical Modeling of the Nonlinear Cyclic Response of Shallow Foundations*. PEER Report, Pacific Earthquake Engineering Research Center, University of California, Berkeley.

“History.” (2016). *Precast/Prestressed Concrete Institute*, <https://www.pci.org/About_PCI/History/>.

Hosseinzadeh, N. A., and Nateghi-a, F. (2004). “Shake table study of soil structure interaction effects on seismic response of single and adjacent buildings.” Vancouver, B.C., Canada.

Kosmatka, S. H., and Wilson, M. (2011). *Design and Control of Concrete Mixtures: The guide to applications, methods, and materials*. Portland Cement Association.

Li, H.-N., Bai, F.-L., Tian, L., and Hao, H. (2011). “Response of a transmission tower-line system to a canyon site to spatially varying ground motions.” *Journal of Zhejiang University-Science A (Applied Physics & Engineering)*, 12(2), 103–120.

Li, H.-N., Shi, W.-L., Wang, G.-X., and Jia, L.-G. (2005). “Simplified models and experimental verification for coupled transmission tower-line system to seismic excitations.” *Journal of Sound and Vibration*, (286), 569–585.

Liang, J. Z., and Hao, H. (2008). “Performance of Power Transmission Tower in PMA under Simulated Earthquake Ground Motion.” Beijing, China.

López, W., J. A. González. (1993). "Influence of the degree of pore saturation on the resistivity of concrete and the corrosion rate of steel reinforcement." Cement and Concrete Research 23(2): 368-376.

McClure, G., and Lapointe, M. (2003). “Modeling the structural dynamic response of overhead transmission lines.” *Computers and Structures*, 81, 825–834.

Mehta, P.K. and P.J.M. Monteiro, *Concrete: Microstructure, Properties, and Materials*. 3rd ed. 2006, New York: McGraw-Hill.

Millard, S. Reinforced Concrete Resistivity Measurement Techniques. in ICE Proceedings. 1991. Thomas Telford.

Morris, W., A. Vico, M. Vázquez. (2004). "Chloride induced corrosion of reinforcing steel evaluated by concrete resistivity measurements." Electrochimica Acta 49(25): 4447-4453.

National Research Institute for Earth Science and Disaster Resilience. (2016). “Strong-motion seismograph Networks.” <http://www.kyoshin.bosai.go.jp/>.

Negro, P., Paolucci, R., Pedretti, S., and Faccioli, E. (2000). “Large scale soil-structure interaction experiments on sand under cyclic loading.”

Pacific Earthquake Engineering Research Center. (2016). “Peer Ground Motion Database.” <http://ngawest2.berkeley.edu/>.

Pengyun, L., Jiedong, L., Ming, N., Wanli, Z., and Anguo, W. (2012). “Dynamic Response of Power Transmission Towers under Wind Load.” *Energy Procedia*, 17, 1124–1131.

Pitilakis, K. D., Karapetrou, S. T., and Fotopoulou, S. D. (2014). “Consideration of aging and SSI effects on seismic vulnerability assessment of RC buildings.” *Bull Earthquake Engineering*, 12, 1755–1776.

Polder, R., Andrade, C., BElsener, B., Vennesland, O., Gulikers, J., Weidert, R. and Raupach, M. (2000). “Test methods for on site measurement of resistivity of concrete.” *Materials and Structures*, 33, 603-611.

Precast Concrete Institute. (2004). *PCI Design Handbook*.

Prestressed Concrete Transmission Pole Structures. (2012). ASCE Manuals and Reports on Engineering Practice, American Society of Civil Engineers, Reston Virginia.

Riley, M. J., Kempner Jr., L., and Mueller III, W. H. (2003). “A Comparison of Seismic (Dynamic) and Static Load Cases for Electric Transportation Structures.” *Earthquake Engineering*, 687–696.

Rodgers Jr., T. E. (1984). “Prestressed Concrete Poles: State-of-the-Art.” *PCI Journal*, (September- October), 53–103.

Saha, M. K., and Tan, K. H. (2005). “GFRP- Bonded RC beams under sustained loading and tropical weathering.” *American Concrete Institute*, 230, 1379–1396.

Sanabra Loewe, M., and Capellà Llovera, J. (2014). “The four ages of early prestressed concrete structures.” *PCI Journal*, 59(4), 93–121.

Song, H. W., V. Saraswathy. (2007). "Corrosion monitoring of reinforced concrete structures - A review." International Journal of Electrochemical Scienc. 2(1): 1-28.

Stauth, D. (2016). “Cascadia Lifelines Program begun to aid earthquake preparation.” *News and Research Communications*, <http://oregonstate.edu/ua/ncs/archives/2013/oct/cascadia-lifelines-program-begun-aid-earthquake-preparation>.

Struedlein, Dr. A., and Higgins, Dr. C. (2015). “Willamette Valley Soil Spring Constant.”

Taniwaki, K., and Ohkubo, S. (2004). “Optimal synthesis method for transmission tower truss structures subjected to static and seismic loads.” *Struct Multidisc Optim*, 26, 441–454.

Tian, L., Li, H.-N., and Liu, G. (2010). “Seismic Response of Power Transmission Tower-Line System Subjected to Spatially Varying Ground Motions.” *Mathematical Problems in Engineering*, 2010, 20.

Tipson, F. S. (2013). *Natural Disasters as Threats to Peace*. Special Report, United States Institute of Peace, Washington DC.

Todorovska, M. I. (2002). “Full-scale experimental studies of soil-structure interaction.” *ISET Journal of Earthquake Technology*, 39(3), 139–165.

Ueli M. Angst, B.E., ACI-13-024, On the Applicability of the Wenner Method for Resistivity Measurements of Concrete. ACI Materials Journal, 2013.

Xie, Q. (2013). “Shaking table test on UHV transmission tower 8-bundle conductor coupling system.” Shanghai, China.

Yokel, F. Y. (1990). *Earthquake Resistant Construction of Electric Transmission and Telecommunication Facilities Serving the Federal Government Report*. Earthquake Hazard Reduction, Federal Emergency Management Agency, Washington DC.

8 Appendix

8.1 Additional Material testing Reports

8.1.1 Petrographic Analysis

Report created by: Tyler Deboodt

Two concrete cores were extracted for petrographic analysis from a region of the poles that experienced no stress during structural testing. One section above ground and one section below ground were investigated and analyzed through an independent company, GHD. ASTM C856 was followed to determine composition, signs of deterioration, and estimated water-to-cement ratio for each sample (ASTM C856). Composition of the concrete is seen in Table *8-1*.

Table 8-1 Concrete composition determined from petrographic analysis.

	Above ground	Below ground	Average
Coarse aggregate	55.0%	50.0%	52.5%
Fine aggregate	25.0%	30.0%	27.5%
Cement paste	18.5%	18.0%	18.3%
Porosity	1.5%	2.0%	1.8%
w/c	0.35	0.35	0.35

The coarse and fine aggregates in both samples were primarily basalt with some granite. These aggregates were well rounded gravels with low sphericity in shape. The basalt

consisted of plagioclase feldspar (55-65%), volcanic glass (15-20%), olivine (10-15%), orthopyroxene (5-10%), and traces of magnetite and ilmenite. The feldspar and volcanic glass had a fine-grained matrix, whereas the olivine, orthopyroxene were present as phenocrysts. The granite consisted of quartz (40%), orthoclase (30%), plagioclase feldspar (25%), biotite (5%), and traces of epidote and magnetite.

Minor microcracking was observed in the cement paste as well as in the ITZ. Most of the cracks had no secondary products, and it was determined these were likely caused by drying shrinkage or stresses since there was no reaction products or typical damage features caused by deterioration of the paste or aggregates. However, a few of the microcracks were partially filled with ettringite, as seen in **Error! Reference source not found.**. Furthermore, fewer voids and cracks filled with ettringite were observed in the above ground sample when compared to the below ground sample.

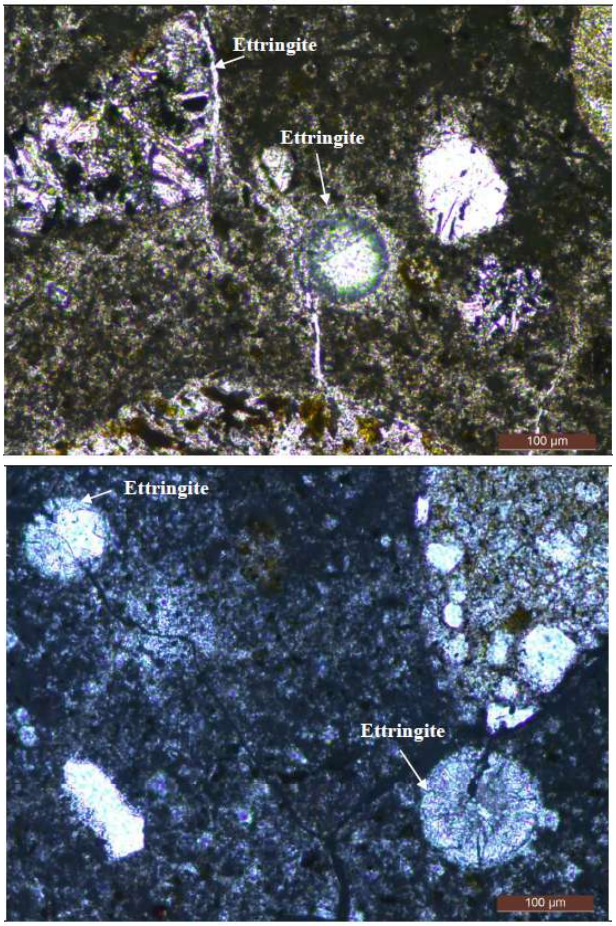

Fig. 8-1 Ettringite deposites observed with natural light in the above ground sample (Top) and below ground sample (Bottom).

8.1.2 Scanning Electron Microscopy

Report created by: Tyler Deboodt

Scanning electron microscopy (SEM) was used to investigate the quality of microstructure and potential deterioration within the microstructure. An acceleration energy of 15 kV was used for all analysis. A spot size of 5.0 was typically used for magnifications up to 100 µm, but needed to be reduced at higher magnifications to minimize charging of the sample. Two regions of concrete were investigated that were exposed to different environmental

conditions. These conditions were concrete that was exposed above ground, and concrete that was below ground. Furthermore, concrete samples for thin sectioning were taken from areas of the concrete poles that experienced no stress during structural testing. SEM results for the above ground concrete is seen in Fig. 8-2.

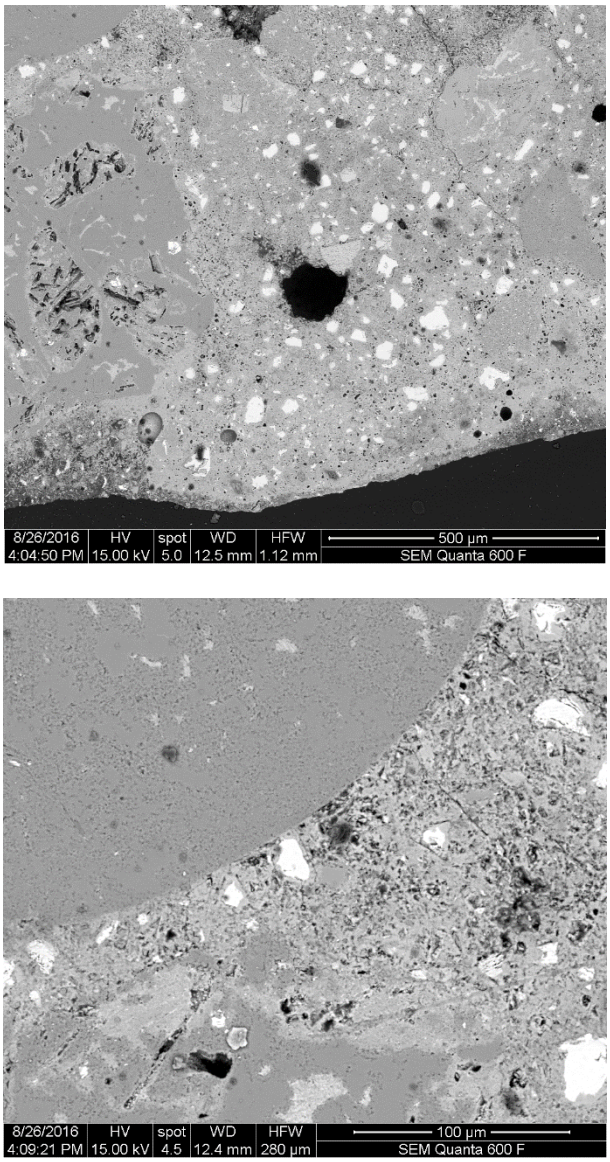

Fig. 8-2 - SEM analysis of above ground concrete

It can be seen in Fig. 8-2 that the microstructure exhibits low porosity, particularly near the edge of the concrete. The paste matrix near the exterior edge of the sample was similar to the bulk, interior paste matrix, indicating minimal to no deterioration of the concrete. This was corroborated with the carbonation testing done immediately after structural testing and a visual inspection prior to structural testing. Furthermore, the interfacial transition zone (ITZ) was shown to be intact and the paste in the ITZ was comparable to that of the bulk paste matrix. Some minor microcracking was observed, but this could have been caused by sample preparation of the specimen for SEM.

Two thin sections were obtained the below ground concrete. A second section was taken to observe a reaction rim occurring around one of the aggregates. SEM images for the below ground sections are seen in Fig. *8-3*.

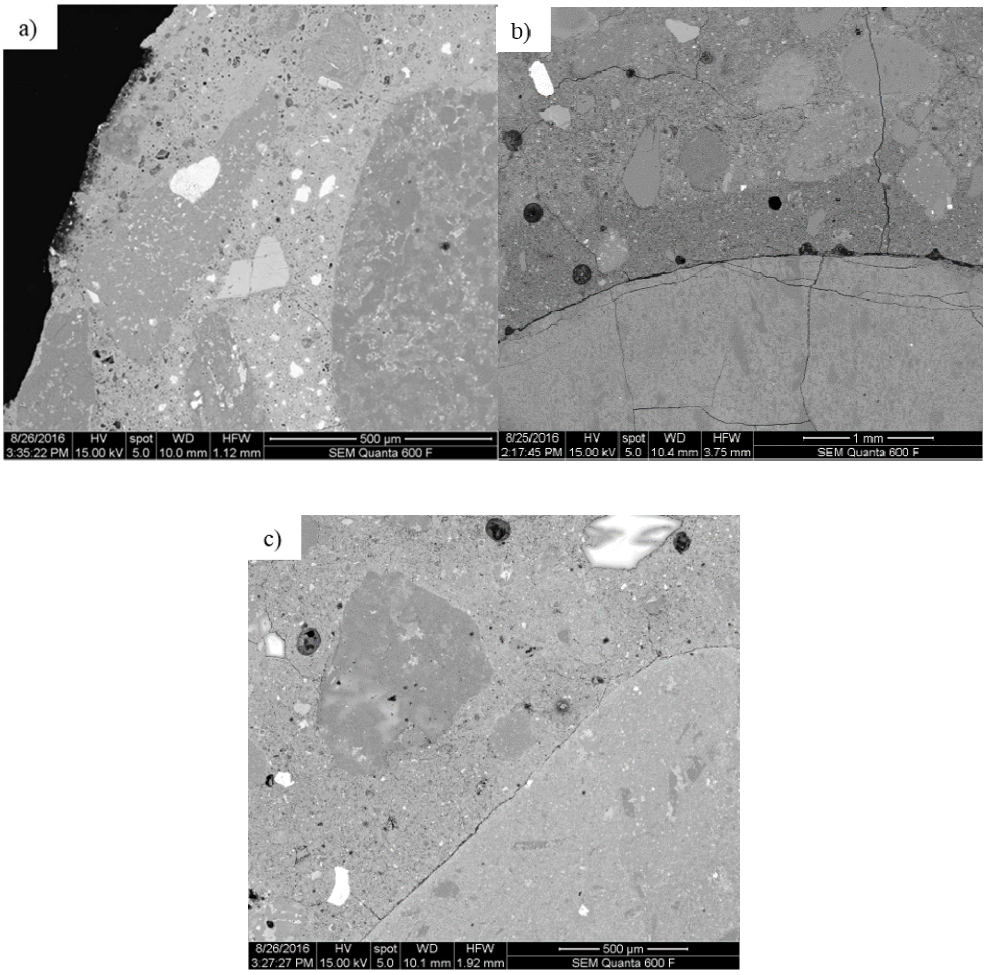

Fig. 8-3 SEM analysis of below ground concrete. Image a) indicates no damage near the exterior surface of the concrete pole. Minor microcracking was observed, but an intact ITZ. Image b) shows microcracking throughout the bulk paste and cracking round the ITZ

Comparing the above ground and below ground concrete, it was observed the below ground concrete had a higher degree of hydration. This indicates a prolonged presence of moisture below ground. In Fig. *8-3*-a), little change throughout the paste matrix was observed from the exterior surface to the overall bulk paste. Additionally, it was found that there was very little microcracking and an intact ITZ in this section. However, it was seen in Fig. *8-3*-b) and Fig. *8-3*-c) there was a larger amount of microcracking throughout the paste matrix, as

well as void space between the aggregate and the bulk paste matrix. In Fig. *8-3* -b) cracking was observed in both the paste and the aggregate. A reaction rim around the aggregate (720-880 µm in thickness) was observed. Furthermore, in Fig. *8-3* -b) and Fig. *8-3*-c), mineral deposits were found in several of the air voids. A closer investigation of the deposits are seen in Fig. 8-4.

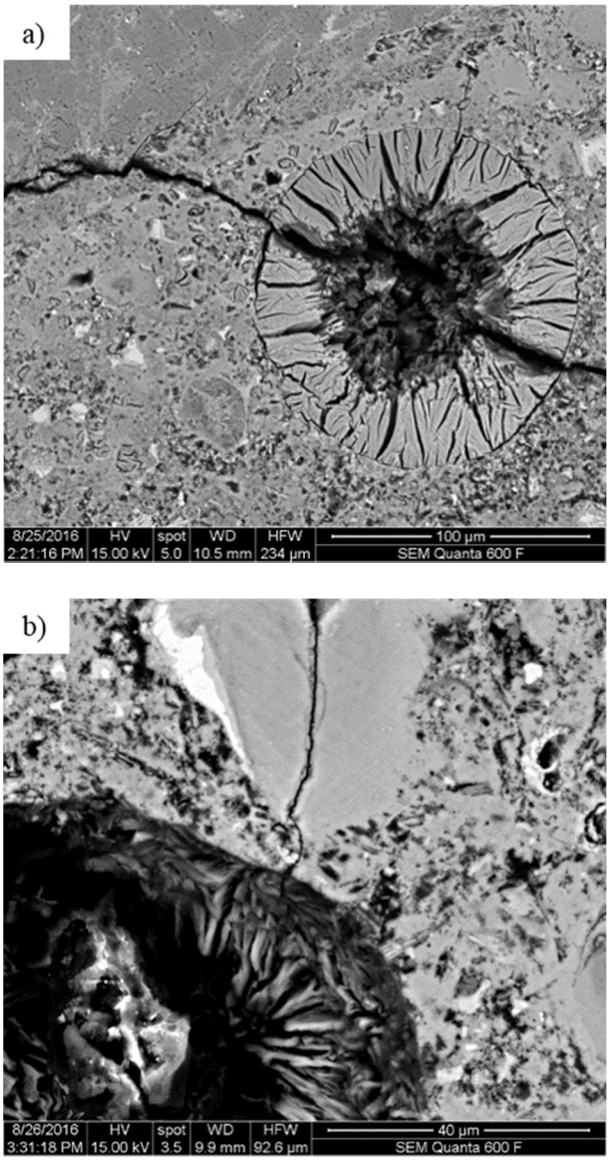

Fig. 8-4 - Ettringite deposition in air voids

The presence of water and the siliceous composition of the aggregates indicate the likelihood of alakali-silica reaction (ASR) contributing to the deposition of these minerals. Additionally, steam curing may be used in many prestressed concrete structures to expedite the strength gain of structural elements. The maximum temperature used for steam curing can range from 60-82 ˚C, depending on the design code used for design [1]. Delayed ettringite formation (DEF) may occur if the temperature of the concrete exceeds 65 ˚C since ettringite is unstable above this temperature [2]. Since the curing regiment of these particular elements is unknown, DEF may be a concern. Upon further investigation, significant ASR damage is unlikely since there are no mineral deposits in or around the aggregates, only in the air voids. Furthermore, DEF is unlikely to be contributing to the mineral deposition since these minerals were only found in air voids and not throughout all of the cracks. The formation of these minerals is likely a secondary ettringite formation known as Ostwald ripening. This process is caused by the continuous dissolution of ettringite formed in small cracks and voids and reprecipitating in larger voids [3]. This type of ettringite forms larger crystals in bigger empty spaces (i.e. entrapped air) [4], and there is no evidence this leads to damage [3].

SEM Report References

[1] Hwang S-D, Khatib R, Lee HK, Khayat KH. Optimization of steam-curing regime for high-strength, self-consolidating concrete for precast, prestressed concrete applications. PCI Journal. 2012;57(3):48-62.

[2] Mehta PK, Monteiro PJM. Concrete: Microstructure, properties, and materials. 3 ed. New York: McGraw-Hill; 2006.

[3] Thomas M, Folliard K, Drimalas T, Ramlochan T. Diagnosing delayed ettringite formation in concrete structures. Cement and Concrete Research. 2008;38(6):841-7.

[4] Johansen V, Thaulow N, Skalny J. Simultaneous presence of alkali-silica gel and ettringite in concrete. Advances in Cement Research. 1993;5(17):23-9.

8.2 EWEB Construction Drawings

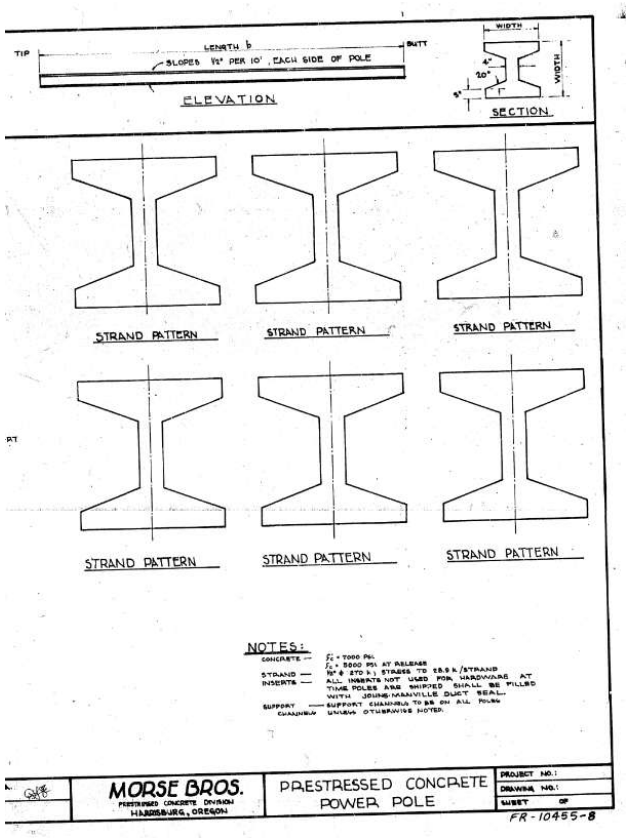

Fig. 8-5 Construction drawing #1

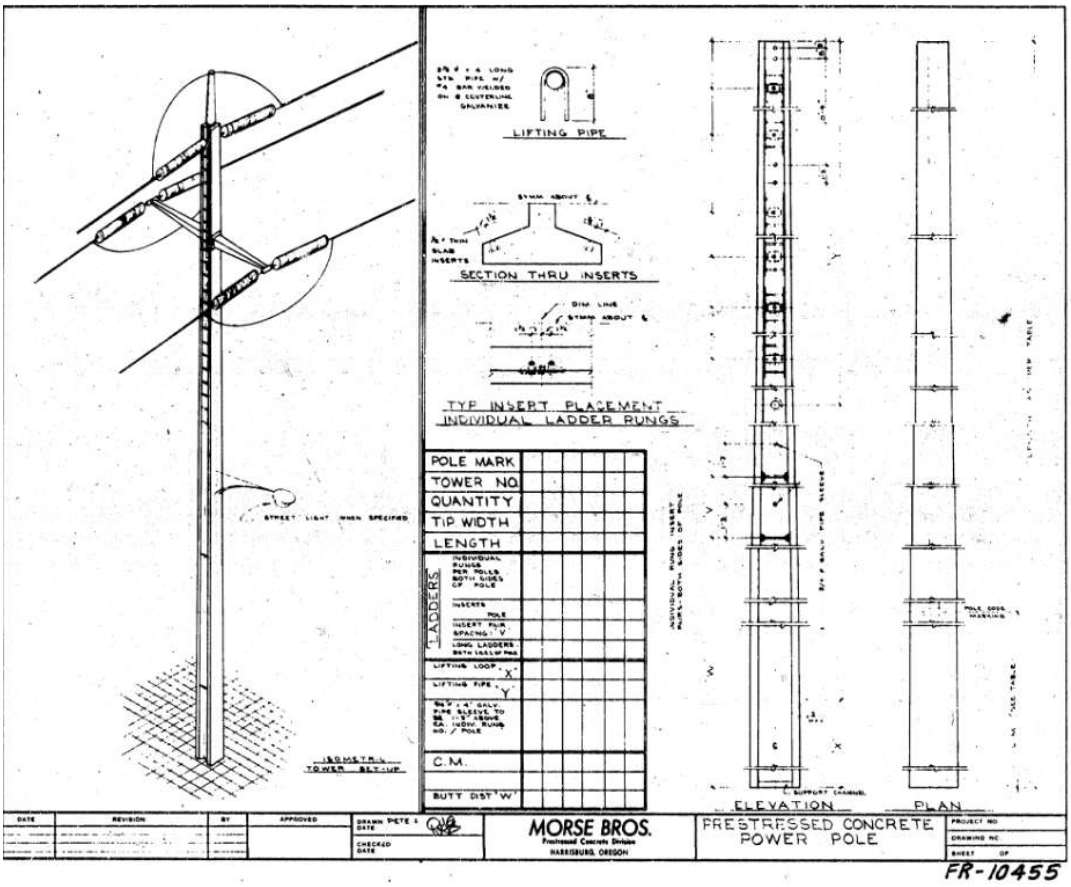

Fig. 8-6 Construction drawing #2

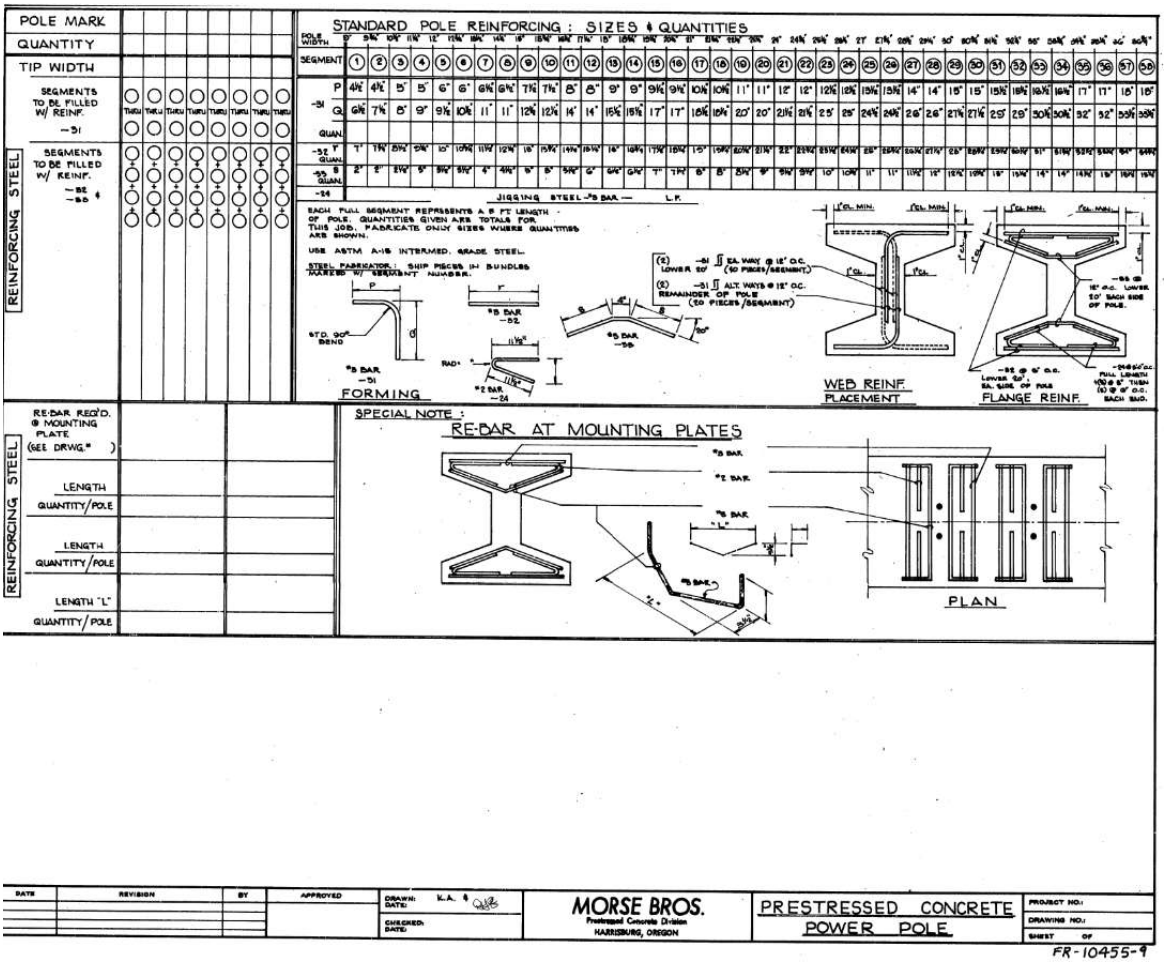

Fig. 8-7 Construction drawing #3.

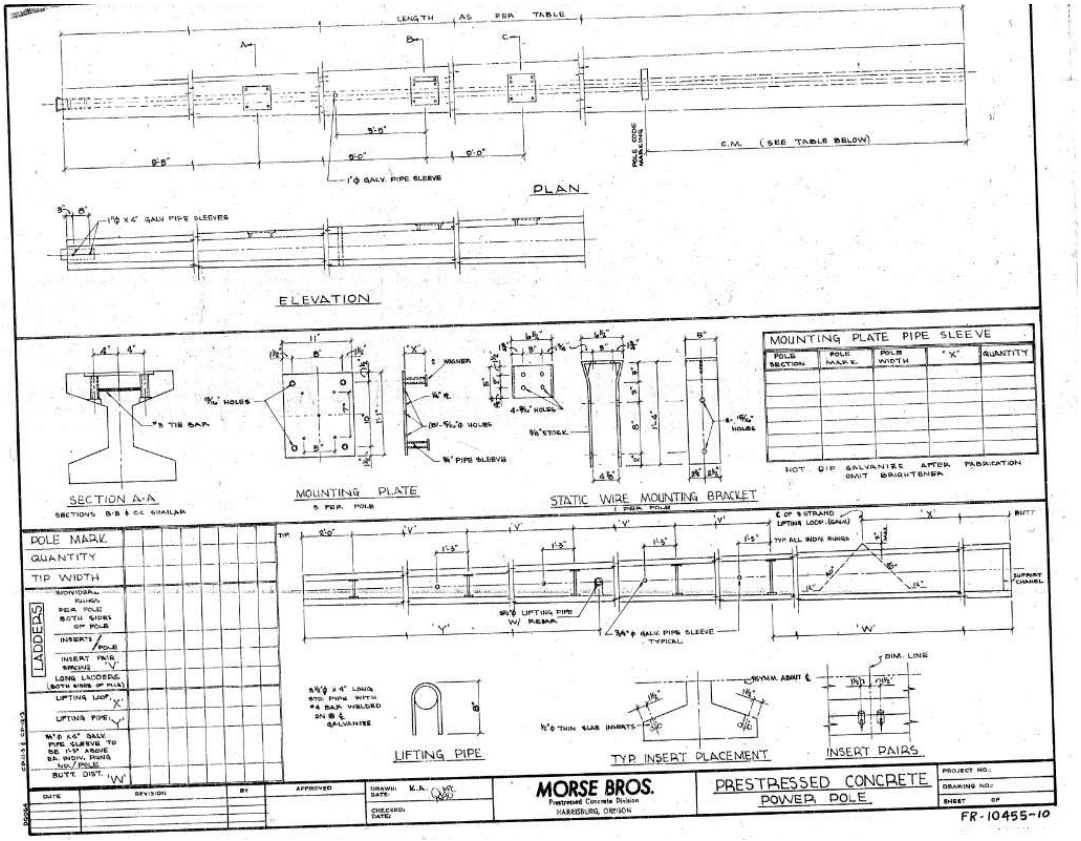

Fig. 8-8 Construction drawing #4

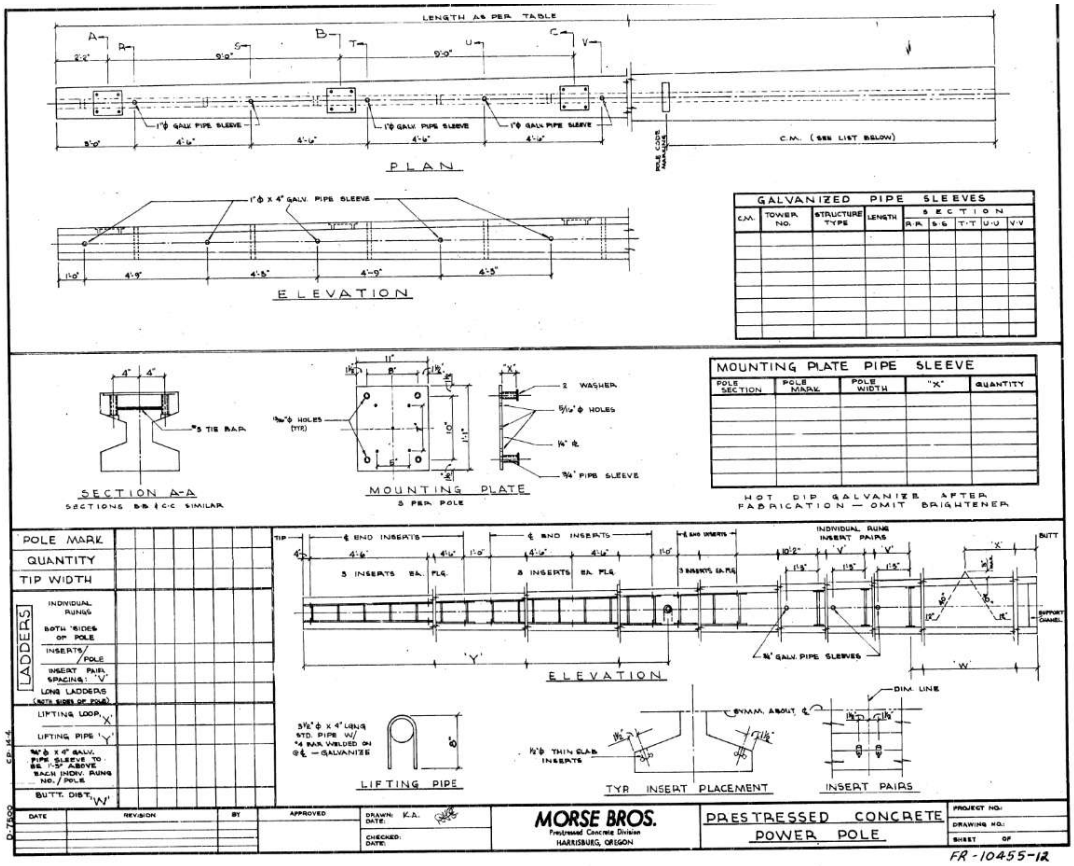

Fig. 8-9 Construction drawing #5

8.3 Earthquake Ground Motions

The following three ground motions were plotted for reference. The motions were used for the OpenSees input files to perform uniform excitation to the foundation. See section Comparative Analysis for further information.

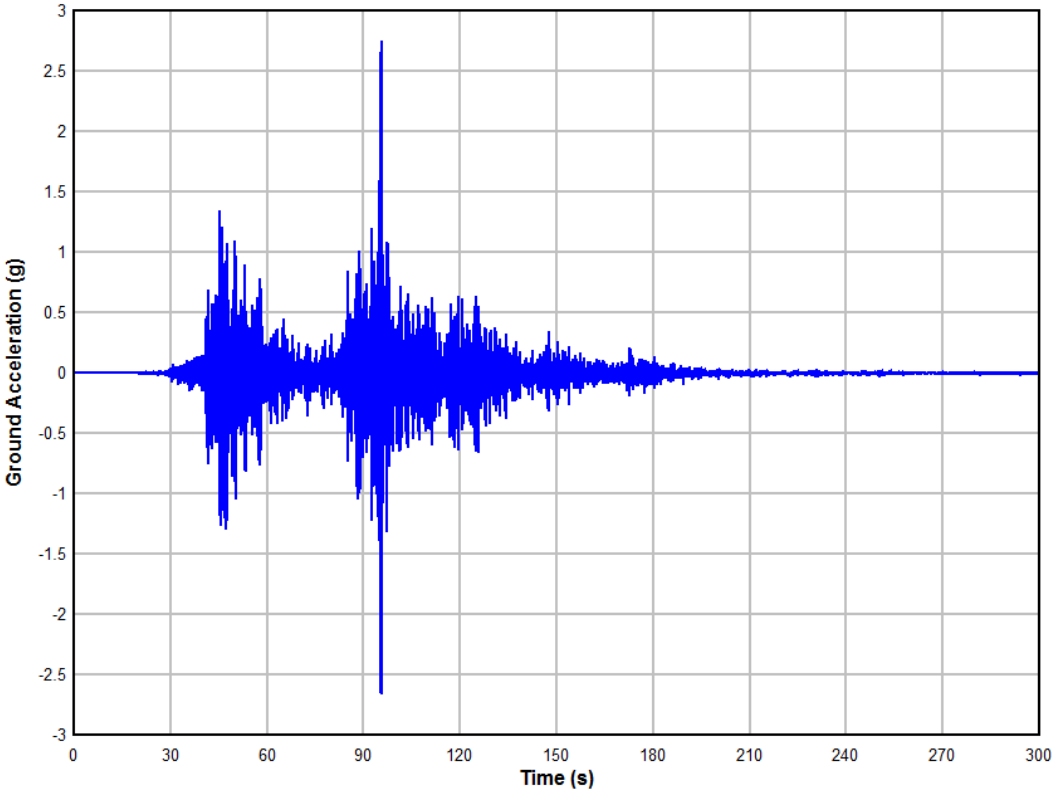

Fig. 8-10 2011 Tahoku Earthquake Ground Motion.

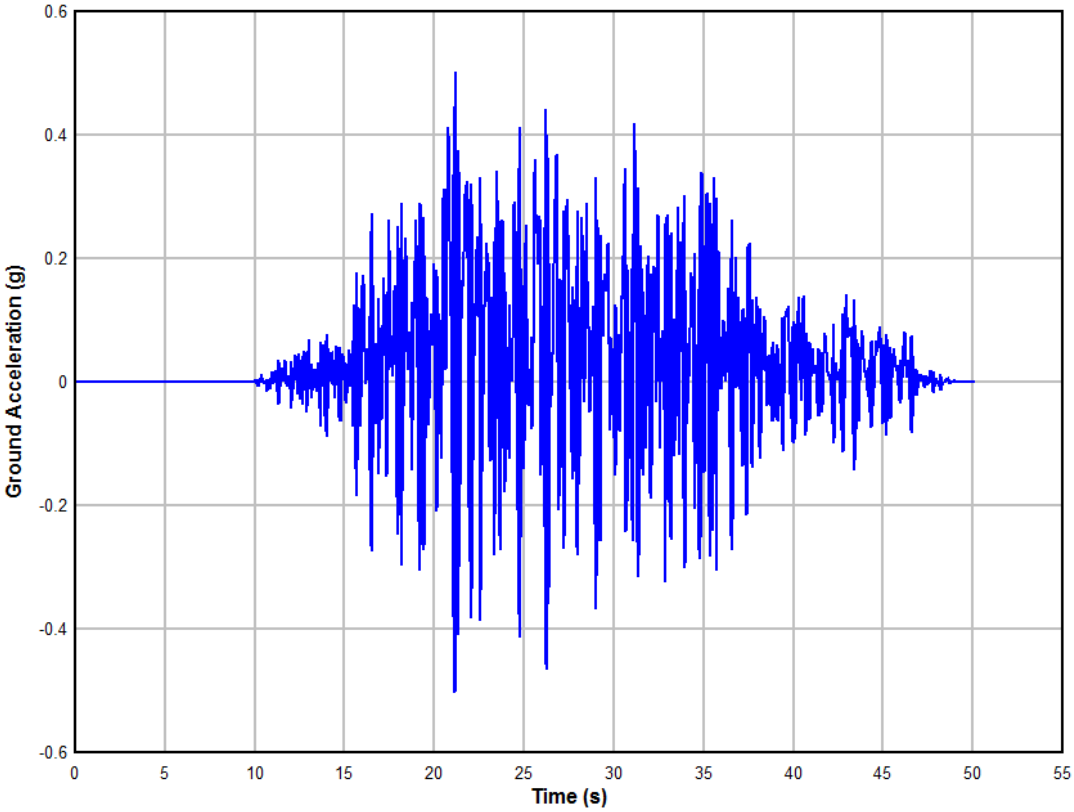

Fig. 8-11 1989 Loma Prieta ground motion.

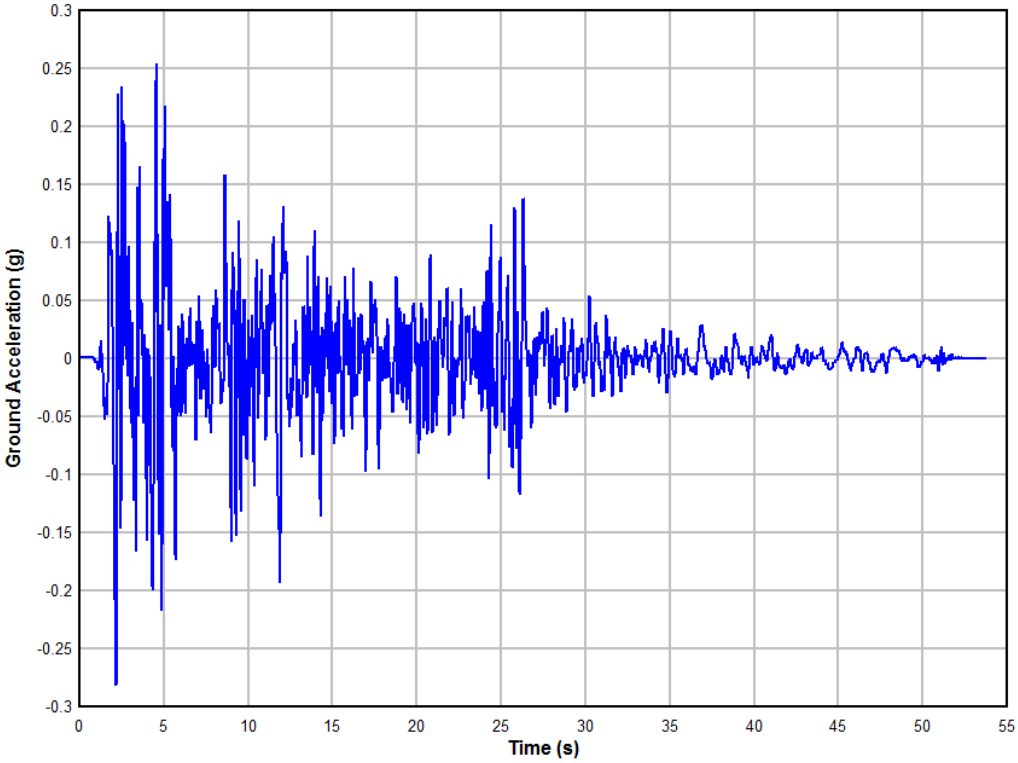

Fig. 8-12 1940 El Centro ground motion.